Dynamique de la phase dans des jonctions Josephson ferromagnétiques

Ivana Petkovic

École Doctorale de Physique de la Région Parisienne - ED 107

THÈSE DE DOCTORAT

présentée par

Ivana Petković

pour obtenir le grade de

Docteur en Sciences de l'Université Paris-Sud 11
Spécialité Physique

Dynamique de la phase dans des jonctions Josephson ferromagnétiques

Thèse préparée sous la direction de Marco APRILI
soutenue le 23 janvier 2009
devant la commission d'examen :

Dominique MAILLY	Président
Marco APRILI	Directeur
Claire BARADUC	Rapporteur
Rudolf GROSS	Rapporteur
Zoran RADOVIĆ	
Sadamichi MAEKAWA	

Laboratoire de Physique des Solides UMR 8502

2009.

PHASE DYNAMICS OF THE FERROMAGNETIC JOSEPHSON JUNCTIONS

Science is magic that works.

Kurt Vonnegut
Cat's Cradle

Abstract

Superconductivity and ferromagnetism are antagonistic orders, that do not co-exist in bulk materials. However, artificially we can realize nanometric heterostructures where the two orders can coexist locally, and then we might expect coupled modes of the two order parameters. We have realized this possibility experimentally, with an s-wave superconductor, using a ferromagnetic Josephson junction. Then, in addition to the decrease of the Josephson current due to the exchange field, the magnetization dynamics couples to the Josephson phase. As a consequence of energy dissipation through spin motion, a magnetic resonance of frequency ω_s appears as a depression in the current-voltage curve of the Josephson junction when $\hbar\omega_s = 2eV$. As we have shown theoretically, this coupling occurs through an interference effect involving the Aharonov-Bohm phase. We describe this by analogy with Fraunhofer diffraction with a time dependent phase plate. By exciting the magnetic system via the singlet Josephson supercurrent which also detects its characteristic modes, we have been able to perform a resonance experiment on a mere 5 femto cm^3 of material or 10^7 Ni atoms.

We have also investigated the classical phase dynamics of large area strongly underdamped ferromagnetic Josephson junctions by measuring the probability of switching into the dissipative state. We have found that in the stationary regime the switching is governed by the thermal noise, indicating negligible spin noise induced broadening. In the non stationary regime, achieved for the ramp frequency comparable to the inverse RC time, we have performed a pump-probe experiment that shows a kinetic phase transition due to the phase

bifurcation. Bifurcation manifests itself as a bimodal switching distribution. Through the frequency dependence of the population of each mode we directly measured the phase relaxation time τ_φ. Numerical simulations account for the experimental values of τ_φ, set by the quasiparticle resistance.

We have also investigated the electromagnetic field propagation inside the ferromagnetic Josephson junctions by measuring the characteristic Fiske resonances, that take place between the Josephson current and electromagnetic standing waves inside the junction. We have shown that the dispersion relation $\omega(k)$ of these resonances presents a constant shift towards higher frequencies for ferromagnetic junctions, compared to the non-ferromagnetic ones.

Acknowledgments

I would like to thank my thesis advisor Marco Aprili for his constant and tireless support. I have benefited greatly both from his scientific insight and competence, as well as dedication and work ethic, and I consider it a great privilege to have been able to work with him.

I would like to thank Bertrand Reulet and Julian Gabelli, always in the mood to discuss physics and answer my questions, as well as scout for the gateau of the day. My thanks also goes to Francesca Chiodi, a good friend and interlocutor I enjoyed very much sharing the office with.

I would like to thank Francois Beuneu who performed the ferromagnetic resonance measurements that helped us gain further insight into our results.

I would like to thank Sadamichi Maekawa and Stewart Barnes for providing the theory of coupling between the ferromagnetic and superconducting order parameters and contributing to a more complete understanding of the experiment, as well as for committed work and discussion during the redaction of the paper.

I would like to thank Hervé Hurdequint and André Thiaville for interesting and useful discussions.

I would also like to thank Jean-Yves Prieur, who worked to help us put in place the dilution fridge and kindly provided many tutorials on cryogenics.

My thanks also extends to Laurence Ferlazzo for her amiability and efficiency in performing with me the RIE on our samples.

I would like to thank Gilles Guillier who I could count on to make the right piece of equipment.

I would also like to thank Hélène Bouchiat, Sophie Guéron and Meydi Ferrier for many useful discussions and their kind interest in my work.

I would like to thank Zoran Radović, who has taught me a lot, but who has also inspired me, supported me and whose elegance in physics makes it look easy.

As for the financial support, I acknowledge Allocation de Recherche No. 18870-205 for the duration of my PhD thesis. I also acknowledge the support of the French Cultural Center in Belgrade for providing me a scholarship during the DEA, thus enabling me to continue my studies in France, and in particular to Ms. Lila Prstojević, whose help and support were crucial in that respect.

I would like to thank Rudolf Gross and Claire Baraduc for accepting to be the examiners of my PhD thesis, to Dominique Mailly for accepting to be the president of the committee, and to Sadamichi Maekawa and Zoran Radović for accepting to be part of the committee.

And thanks to my mother and brother in Serbian: Hvala za podršku i ljubav.

This thesis is dedicated to the memory of my father.

Table of Contents

Introduction

Superconductivity is a rich and interesting playground for testing quantum mechanics. Notably are interesting the macroscopic structures that display phase coherence, such as Josephson junctions. A Josephson junction consists of a superconductor interrupted by a weak link, and the current passing through depends periodically on the phase difference between the two sides, reflecting its quantum-mechanical nature. When embedding the Josephson junctions into superconducting loops, we create SQUIDs (Superconducting QUantum Interference Devices) - artificial macroscopic objects that keep the phase coherence, and can be used as building bricks for quantum computing.

The basic unit of a superconductor, a coherent pair of electrons, so-called Cooper pair, is a spin singlet, while ferromagnetism tends to align all the spins. This is the antagonism between a superconductor and a ferromagnet, which prevents their coexistence. So far, they have been found to co-exist in bulk in the case where the magnetic order is inhomogeneous, or the superconducting pairing is most probably triplet. However, in the singlet case, they can coexist locally, at the interface, and they can be combined at lengths of the order of the coherence length to give new ground states. The presence of a ferromagnetic exchange field can induce a center-of-mass momentum of the Cooper pair, translating into a phase modulation of the superconducting order parameter in real space. Therefore, making a Josephson junction with a ferromagnetic barrier at thicknesses for which the order parameter is negative, we find that its ground state is for the phase difference of π, rather than zero. When embedding such a junction into a superconducting loop, it acts as a phase battery, adding

a phase difference of π. This gives new opportunities for SQUID operation, making the alternative way to manipulate the phase with external magnetic field redundant. However, before we can successfully create SQUIDs with π junctions, we need to find out just how noisy they are. A possible source of noise are the magnetic modes of the ferromagnetic layer that couple with the Josephson phase through the Aharonov-Bohm term.

Another unique property of the Josephson effect is its nonlinearity - the current is dependent on the sine of the phase difference. This enables the rectification of resonant effects taking place at higher frequencies, so they are visible in dc. This is inherent to every Josephson junction, making it possible to probe the external rf radiation coupling resonantly to the characteristic Josephson phase oscillation. In the ferromagnetic junctions it is the internal ferromagnetic modes that couple resonantly to the Josephson phase, so we can measure directly the spin-wave spectrum or the domain-wall-related resonances, with great sensitivity.

The Josephson phase has an Aharonov-Bohm contribution of the form $\int \mathbf{A} \cdot d\mathbf{l}$, where $\mathbf{A}$ is the vector potential and $\mathbf{l}$ the phase trajectory. As the phase can take different paths across the junction, it interferes with itself, and the critical current as function of field shows the same dependence as the light intensity as function of distance from the center of the screen in the diffraction experiment - the Fraunhofer pattern. In this work we have shown that for ferromagnetic Josephson junctions the ferromagnet acts as a wedge-shaped optical plate, its refractive index analogous to magnetization, shifting the maximum of the Fraunhofer curve. We can generalize the Fraunhofer concept to include the magnetization dynamics, reflected in $\mathbf{A}(t)$.

In this work, we have demonstrated for the first time the coupling between the spin-wave modes and the Josephson current in ferromagnetic Josephson junctions. A magnetic resonance of frequency ω_s appears as a depression in the current-voltage curve when $\hbar\omega_s = 2eV$. We have shown that this depression is proportional to the imaginary part of the ferromagnetic susceptibility χ''. We have demonstrated the excitation of the magnetic system via

singlet supercurrent on a thin layer of weak ferromagnet, and performed a ferromagnetic resonance measurement (FMR) on a ferromagnetic quantity so small that it is outside the range of conventional methods.

In the second part of the thesis we have investigated the proper phase dynamics of ferromagnetic Josephson junctions with very low damping, showing that in the adiabatic regime, the large surface junctions are no noisier than their non-ferromagnetic counterparts. We have also performed a pump-probe measurement: with a fast sawtooth current ramp we put the Josephson phase out of equilibrium, and then probed the phase dynamics, detecting it as voltage generated across the junction. In this way we accessed directly the phase relaxation time τ_φ, showing that the phase relaxation is set by the quasiparticle resistance. We have shown that when the ramp frequency is comparable to the inverse RC time, the Josephson junction displays bifurcation - with minute changes in the initial conditions, provided by the thermal noise, the phase can either relax completely into the equilibrium corresponding to non-dissipation, or stay on the dissipative branch.

Finally, we have investigated the resonant coupling between the Josephson current and the standing electromagnetic modes in the ferromagnetic barrier - the Fiske resonances. The barrier acts as a transmission line, and the spectrum of Fiske resonances is shifted for ferromagnetic compared to the non-ferromagnetic junctions due to the changed high frequency impedance.

Future applications of the Josephson effect for probing ferromagnetic modes would include the investigation of the domain wall movement. Another promising line is the investigation of distant correlations of a Cooper pair when separated (following conversion into a so-called Andreev pair) and forced to traverse different magnetic domains. It would also be possible to envisage refining the FMR experiment down to accessing much lower quantities of spin, perhaps even attaining the dynamics of a single spin.

Chapter 1

Interplay between the Josephson phase and the magnetic modes

1.1 Superconducting ferromagnetic heterostructures

Ferromagnetism is known since ancient times, and it is the property of certain materials, such as iron or nickel, to exhibit permanent magnetization. The origin of ferromagnetism is quantum-mechanical, it is the spin of elementary particles, which acts like a tiny magnetic moment. The nature of correlations between spins, Coulomb interactions and the Pauli principle, makes it possible for them to get into parallel alignment, yielding net magnetization in the energetically more favorable thermodynamical phase. There is a transition temperature, the Curie temperature T_{Curie}, below which the order sets in.

Superconductivity was discovered by Kamerlingh Onnes in 1911[1]. Its signature properties are zero resistance and expelling of the magnetic field (Meissner effect). In 1956 Bardeen, Cooper and Schrieffer (BCS) [2] showed that the Fermi sea of electrons with an arbitrarily small attractive interaction, such as the one provided by the electron-phonon coupling, responds by forming pairs of opposed spin and momentum, co called Cooper pairs. These pairs undergo Bose-like condensation, creating a superfluid with a single quantum mechanical wave function Ψ, also called the order parameter (often denoted by Δ). This is the explanation of the new thermodynamical phase which is characterized by the perfect conductivity and perfect diamagnetism. The critical temperature T_C is the temperature at which the superconductivity sets in.

1.1.1 Antagonism between the superconducting and the ferromagnetic order

Both magnetism and superconductivity are broken symmetry states of matter characterized by an order parameter. For a ferromagnet, the order parameter is the magnetization **M**, the sum of individual spin magnetic moments aligned in the same direction due to an exchange mechanism. The broken symmetry is time-reversal. For a superconductor, the order parameter within the Ginzburg-Landau theory[3] is a complex number $\Delta = |\Delta|e^{i\phi}$ with a magnitude $|\Delta|$ and a phase ϕ, spatially constant in the absence of a magnetic field. The broken symmetry is a gauge symmetry, which is reflected in the choice of the phase ϕ. The superconducting condensate consists of the Cooper pairs, electron singlets of opposite momentum and spin[4]. The superconducting singlet state can be destroyed by an exchange mechanism, tending to align both spins in the same direction. This so-called paramagnetic effect is the main effect preventing the coexistence of the two states[5].

Another way for the external magnetic field, or magnetic moment of a ferromagnet, to influence superconductivity is via the so-called orbital effect. Ginzburg showed that the coupling of the superconducting order parameter with a vector potential of the magnetic field **A** suppresses superconductivity[6]. This is the underlying physics of the Meissner effect, where the superconductor expels the magnetic field up to a surface layer of thickness λ, the penetration depth[7].

However, there is a possibility to tailor the superconducting order parameter on a short length-scale to accommodate for a coexistence between superconductivity and ferromagnetism. Fulde and Ferrel, and independently Larkin and Ovchinnikov, demonstrated that the superconductivity can be non-uniform in a pure ferromagnetic superconductor at low temperature [8, 9]. In the so-called FFLO state, the superconducting order parameter is sinusoidally modulated on the length-scale of the superconducting coherence length ξ_S, the

size of a Cooper pair. The Cooper pairs in this state have a finite momentum, compared with zero momentum in conventional superconductors.

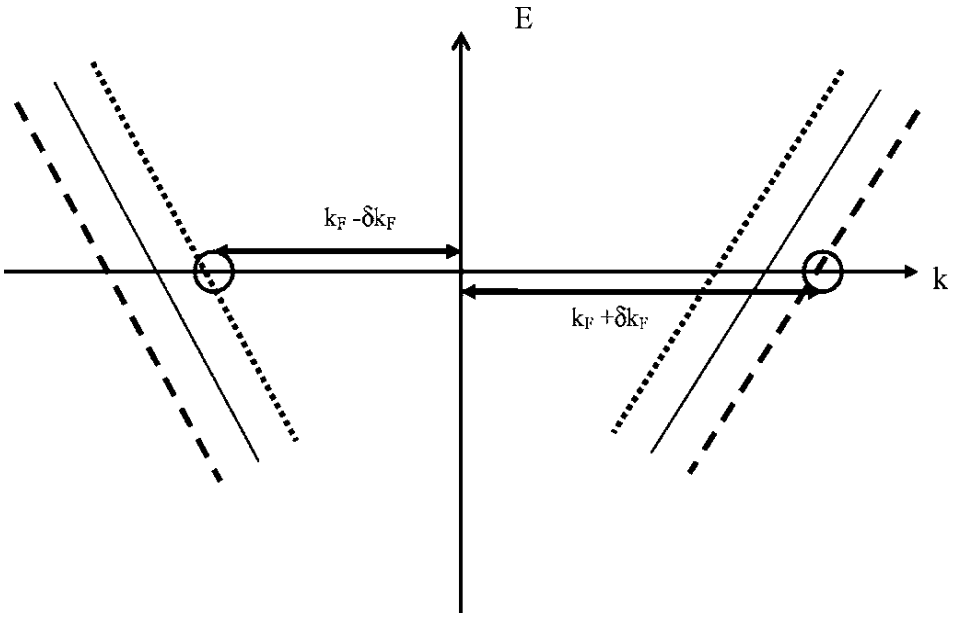

Figure 1.1: One-dimensional example of the energy band of the superconductor near the Fermi surface [10]. The two electrons forming the Cooper pair (represented with circles) in the absence of an external field have the momenta represented with full lines, at the Fermi surface their values are k_F and $-k_F$. In the external field H, there is a Zeeman-splitting induced shift by $\delta k_F = \mu_B H/\hbar v_F$. The shift $+\delta k_F$ is denoted in dashed, and $-\delta k_F$ in dotted lines. The Cooper pair gains a center-of-mass contribution of $2\delta k_F$.

We shall illustrate this by considering a one-dimensional example, see Fig. 1.1 [10]. In the absence of an external field the two electrons with opposite spin forming the Cooper pair have the opposite momenta k_F and $-k_F$ and their center of mass has momentum zero. In the field H, due to the Zeeman splitting, each electron will gain a momentum $\delta k_F = \mu_B H/\hbar v_F$, where v_F is the Fermi velocity and μ_B is the Bohr magneton. The center of mass gains momentum $2\,\delta k_F$, so the order parameter obtains spatial modulation $\exp(2\,i\,\delta k_F x)$.

However, the way to create an analog of the FFLO state artificially is to consider superconducting – ferromagnetic heterostructures, such as submicronic S/F superlattices[11, 12, 13]. When a Cooper pair passes through the ferromagnet, its spin up electron decreases energy by the exchange energy E_{ex}, while the spin down electron gains the same energy. To com-

pensate this, the spin up increases its kinetic energy by this amount, while the spin down decreases it, and the center of mass acquires momentum $2\,\delta k_F = 2E_{ex}/\hbar v_F$, which implies the modulation of the order parameter with period $\pi\hbar v_F/E_{ex}$. Here, the magnetization is parallel to the layers and the orbital effect [14] is neglected.

The first truly ferromagnetic superconductors, UGe_2 and URhGe, have been discovered recently[15, 16]. The assumption is that the superconductivity is triplet, with both spins of the Cooper pair parallel, so there is no paramagnetic effect.

1.1.2 Proximity effect

Order parameter

At the interface between a superconductor (S) and a normal metal (N), they influence one another passing some of their attributes to their neighbor. The Cooper pairs leak from the superconductor into the normal metal, creating locally a condensate. This is the so-called proximity effect[17]. The Ginzburg-Landau superconducting order parameter Δ decays in the normal metal exponentially, over the length ξ_N. In the dirty limit $\xi_N = \sqrt{\hbar D_n/2\pi k_B T}$, where D_n is the diffusion coefficient and T the temperature, while in the ballistic limit $\xi_N = \hbar v_F^n/2\pi k_B T$, where v_F^n is the Fermi velocity in the normal metal. On the other hand, the leaking of the Cooper pairs into the normal metal diminishes the order parameter in the superconductor and that is the so-called inverse proximity effect[18]. The schematic behavior of the real part of the order parameter at the interface is given in Fig. 1.2.

At the interface between a superconductor and a ferromagnet (F), the order parameter shows the exponential decay over a much shorter length than in the normal metal, $\xi_{f1} = \sqrt{\hbar D_f/E_{ex}}$ in the dirty limit or $\xi_{f1} = \hbar v_F^f/2\pi k_B T$ in the clean limit, where D_f and v_F^f are the diffusion coefficient and the Fermi velocity in the ferromagnet. In addition to this, the order parameter in the ferromagnet oscillates due to the paramagnetic effect. In the dirty limit

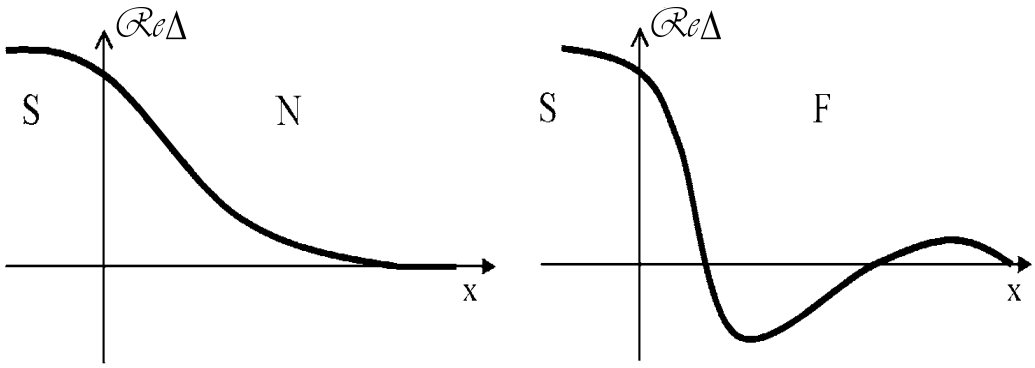

Figure 1.2: Schematic drawing of the real part of the order parameter at the S/N and S/F interface [10].

the characteristic oscillation length $\xi_{f2} = \xi_{f1}$, and in the clean limit the oscillation length $\xi_{f2} = \hbar v_F^f / E_{ex}$ is much shorter than the decay length. So when stacking S/F layers with thickness of the order of the oscillation coherence length, we get the FFLO-like oscillation of the superconducting order parameter.

A simple way to probe the proximity effect is to measure the conductance of an S/N bilayer. In his book[19], Tinkham lays out a very simple semiconductor model, where the density of states (DOS) of a normal metal N_n is constant, while the DOS of the superconductor is $N_s(E) = N_0 E/(E^2 - \Delta^2)^{1/2}$ for $E > \Delta$, otherwise $N_s = 0$, where N_0 denotes the electron density of states at the Fermi level for one spin orientation. Here and in the following we shall use the notation Δ for the absolute value of the order parameter. The tunneling current of the bilayer is then

$$I \sim \int N_n N_s(E) \left[f(E) - f(E - eV) \right] dE$$

where V is the applied voltage and f the Fermi distribution. In the low temperature limit, the conductance $G(V) = dI/dV$ is directly proportional to the DOS.

Andreev reflection

The microscopic mechanism for converting the normal current at the N/S interface into the super-current is the Andreev reflection.

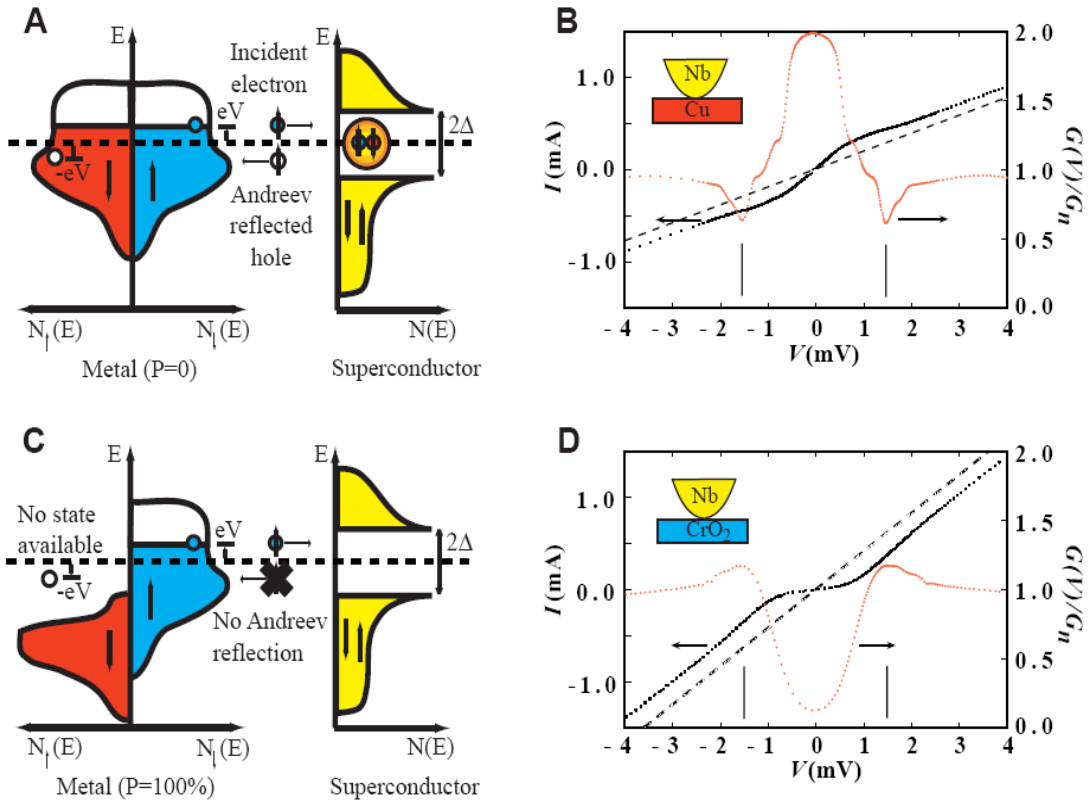

Figure 1.3: Supercurrent conversion at the superconductor-metal interface for spin polarizations of $P = 0$ and $P = 100\%$. **a)** Schematic of the process for $P = 0$ when the Andreev reflection is unhindered by a spin minority population at the Fermi energy E_F. The solid circles denote electrons and open circles denote holes. **b)** Experimental measurement of the IV and differential conductance dI/dV at T=1.6 K via a superconducting Nb point contact on Cu. The vertical lines denote the bulk gap of Nb: $\Delta(T = 0) = 1.5$ meV. The dashed line is the normal state IV for a conductance of $G_n = 0.194\,\Omega^{-1}$. **c)** Schematic of process for $P = 100\%$ when there is no supercurrent conversion at the interface. **d)** Experimental IV and dI/dV at T=1.6 K via the Nb point contact on CrO_2. The dashed line is the normal state IV for a conductance of $G_n = 0.417\,\Omega^{-1}$ [22].

The electron coming from N with the energy $\epsilon < \Delta$ is reflected at the interface as a hole with the opposite momentum, which is equivalent to the creation of a Cooper pair in S [20, 21], see Fig. 1.3a. As measured by Soulen *et al.*[22], the differential conductance $G = dI/dV$ at

the Fermi energy is twice that in the normal state due to the Andreev reflection, Fig. 1.3b. The inverse process is also possible for current passing from S to N, and then a Cooper pair is converted into a so-called Andreev pair of entangled electrons.

At the S/F interface, the Andreev reflection is no longer symmetric to spin reversal. The spin up electron is reflected as a spin down hole, so both bands of the ferromagnet take part in the transport. If the ferromagnet is fully spin polarized, leaving one band empty, the Andreev reflection becomes impossible[23]. The polarization of the ferromagnet can be measured directly by measuring the differential conductance at the S/F interface[22].

1.1.3 Josephson effect and ferromagnetic Josephson junctions

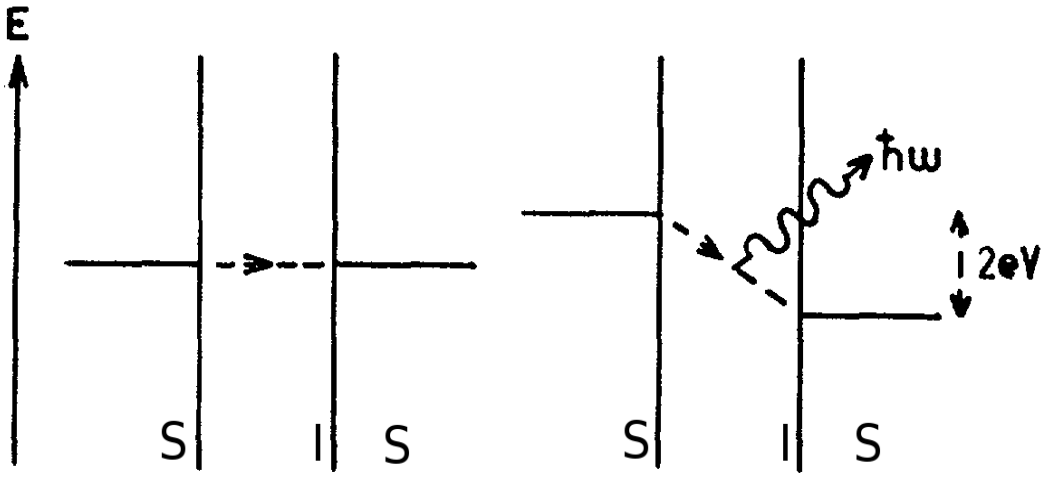

Figure 1.4: The schematics of the dc (left) and ac (right) Josephson effect. At zero imposed voltage, the Cooper pairs can tunnel from the left to the right superconductor S across the insulating barrier I, creating non-dissipative Josephson current. At imposed voltage V, the Cooper pairs pass from left to the right superconductor, giving away the energy $2eV$ as radiation $\hbar\omega$. The inverse process is possible - upon absorbing external radiation $\hbar\omega$, the Cooper pair can tunnel from right to left, overcoming the imposed voltage barrier V [26].

Without imposed voltage, the supercurrent can flow between the two superconducting (S) pads separated by a thin insulating barrier (I)[24, 25, 26], see Fig. 1.4, left panel. The so-

called Josephson current depends on the phase difference between the two superconducting pads, $\varphi = \phi_1 - \phi_2$, where ϕ_1 and ϕ_2 are the corresponding phases of the order parameters of the electrodes, and it is $I = I_C \sin\varphi$, I_C being the critical current. This is the dc Josephson effect. When the voltage V is imposed, the phase changes in time $\dot{\varphi} = (2e/\hbar)V$, with the dot denoting the time derivative. This is the ac Josephson effect. As shown on the right panel of Fig. 1.4, at imposed voltage V the Cooper pairs cross the barrier, radiating away energy $\hbar\omega = 2eV$. The inverse process is also possible - upon absorbing external radiation $\hbar\omega$, a Cooper pair can tunnel from right to left at imposed voltage V, therefore creating non-dissipative current - the so-called Shapiro step[27]. The first Josephson junctions were fabricated by Anderson and Rowell[28, 29].

When enclosing a Josephson junction in a superconducting loop, due to the fact that the total superconducting phase is 2π periodic, and vector potential $\mathbf{A}$ contributes to the phase, the magnetic flux enclosed in the loop is quantified in $\Phi_0 = h/2e$. Such devices, consisting of one or more Josephson junctions enclosed in a superconducting loop, are called the Superconducting QUantum Interference Devices (SQUIDs)[30, 31]. They can behave as macroscopic quantum objects[32, 33] that can be used as building blocks for quantum computing - qubits [34, 35], for Review see [36].

When the barrier inside a Josephson junction is a ferromagnet, due to the oscillation of the superconducting order parameter, the possibility of negative Josephson coupling arises [37]. As was shown by Bulaevskii, *et al.* [38], when the barrier is an insulator with paramagnetic impurities, enabling spin flip processes, the junction can have negative critical current, and its ground state can be for $\varphi = \pi$. It is then described with a current-phase relation $I = |I_C| \sin(\varphi + \pi)$. Such junctions are called π-junctions. Experimentally they have been realized with a barrier made up of a metallic ferromagnet (F)[39, 40] or a normal metal (N) with non-equilibrium quasiparticle distribution (SNS with a gate)[41]. The transition from 0 to the π state as function of thickness of the ferromagnetic barrier has

been demonstrated experimentally[40]. For metallic junctions, the current-carrying Andreev bound states become spin split[42, 43]. Another possibility to create a π junction is with so called grain-boundary, with d-wave superconductors across an insulating barrier. Depending on the position of the insulating interface, one can obtain junctions with different sign of coupling, since the superconducting order parameter is not spatially isotropic[44]. At the 0-π transition and in other particular cases the current-phase relation $I(\varphi)$ can have higher harmonics[45]. When enclosed in a loop, a π junction can take the role of a phase battery[46, 47, 48], since it supplies the phase π without the need to apply the external field. This makes it an interesting low-noise element for use in SQUIDs. However, a question arises if the internal degrees of freedom of the ferromagnet would introduce additional noise, and we shall address that question in this work.

1.1.4 Local coupling between superconductors and ferromagnets - paramagnetic effect

Let us come back to the analogue of the FFLO-like picture for ferromagnetic Josephson junctions. First let us consider the order parameter at the S/F interface. Following the review by Buzdin[10], we generalize the standard Ginzburg-Landau functional

$$F = a(H,T)|\psi|^2 + \gamma(H,T)|\Delta\psi|^2 + \frac{\tilde{\eta}(H,T)}{2}|\Delta^2\psi|^2 + \frac{b(H,T)}{2}|\psi|^4$$

where ψ is the superconducting order parameter. The difference with respect to the standard GL functional is that the coefficients are field dependent and the addition of the third term. We seek the solution of the 1D linear equation for the superconducting order parameter

$$a\psi - \gamma\frac{\partial^2\psi}{\partial x^2} + \frac{\tilde{\eta}}{2}\frac{\partial^4\psi}{\partial x^4} = 0$$

in the form $\psi = \psi_0 \exp(kx)$ for complex $k = k_1 + \imath k_2$. Solving the equation we obtain

$$k_1^2 = \frac{|\gamma|}{2\tilde{\eta}}\left(\sqrt{1+t^*}-1\right)$$

$$k_2^2 = \frac{|\gamma|}{2\tilde{\eta}}\left(\sqrt{1+t^*}+1\right)$$

where $t^* = (T - T_{ci})/(T_{ci} - T_{cu})$, T_{cu} being the transition temperature into the uniform superconducting state and T_{ci} the transition temperature into the FFLO state. If we choose the gauge for the real order parameter in the superconductor, then the order parameter in the ferromagnet is also real and it is

$$\psi = \psi_0 \exp(-k_1 x)\cos(k_2 x). \tag{1.1}$$

In the Ginzburg-Landau formalism the coherence length is defined as $\xi = \sqrt{\gamma/a}$.

Refining the approach, we can calculate the order parameter at the S/F interface using the Usadel equation in the dirty limit or the Eilenberger equation in the clean limit, obtaining

$$\Psi \sim \exp\left(-\frac{x}{\xi_{f1}}\right)\cos\left(\frac{x}{\xi_{f2}}\right). \tag{1.2}$$

In the dirty limit $\xi_{f1} = \xi_{2f} = \sqrt{\hbar D_f/E_{ex}}$, while in the clean limit the decaying length $\xi_{f1} = \hbar v_F^f/2\pi k_B T$ is much longer than the oscillating length $\xi_{f2} = \hbar v_F^f/E_{ex}$.

We can use oscillation of the order parameter with distance from the interface x to obtain Josephson junctions with negative coupling for the appropriate thickness of the ferromagnetic layer.

1.1.5 Nonlocal coupling between superconductors and ferromagnets - crossed Andreev reflection

Let us consider an NSN (or FSF) trilayer. An electron incident from the left from a normal metal into a superconductor with an energy $\epsilon < \Delta$ can undergo one of four possible processes - it can be reflected as a normal electron, it can undergo Andreev reflection, it can co-tunnel as a normal electron or undergo crossed Andreev reflection. The crossed Andreev reflection is possible when S is shorter than the superconducting coherence length ξ_S, and an electron incident from the left N picks up an electron from the right N, leaving a hole, thus forming a Cooper pair in the S. In the inverse process, the two electrons from a Cooper pair form an entangled state after the Andreev reflection and can maintain phase coherence even though spatially separated. This is the non-local aspect of the Josephson effect[49]. The crossed Andreev reflection has been demonstrated experimentally[50, 51].

1.1.6 Orbital effect - contribution of the magnetic field to the Josephson phase

When the magnetic field $\mathbf{B}$ is present, the Aharonov-Bohm contribution $\int \mathbf{A} \cdot d\mathbf{l}$, where $\mathbf{A}$ is the vector potential (curl $\mathbf{A} = \mathbf{B}$) and $\mathbf{l}$ the phase path across the junction[52], enters into the Josephson phase φ. So we have

$$\varphi = \varphi_0 + \frac{2e}{\hbar} \int \mathbf{A} \cdot d\mathbf{l}, \tag{1.3}$$

where φ_0 is a constant. Thus defined, the Josephson phase is gauge-invariant. In ferromagnetic Josephson junctions this expression gives another way to account for the magnetization dynamics - it contributes directly to the Josephson phase via $\mathbf{A}(\mathbf{r}, t)$.

For the in plane field $\mathbf{H} = \mathrm{H}\hat{\mathbf{y}}$, where $\hat{\mathbf{y}}$ is an unit vector in the y direction along the electrodes (and z is perpendicular to the junction plane, see Fig. 1.5), we have the current

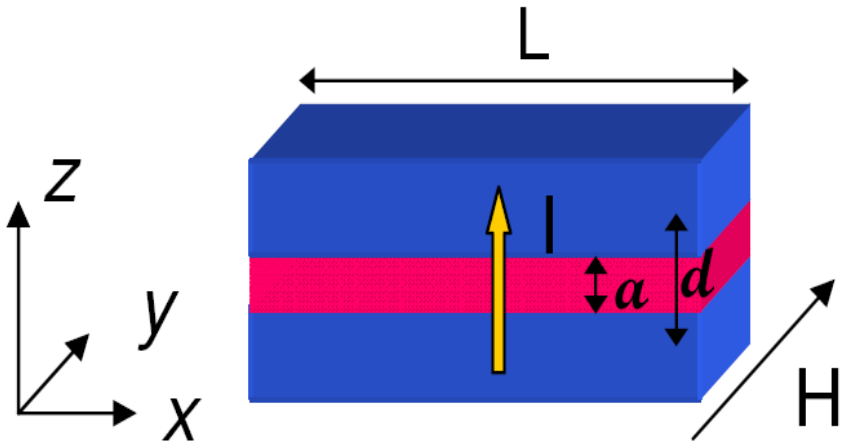

Figure 1.5: The geometry of the ferromagnetic Josephson junction. The blue layers denote the superconducting electrodes and the red layer the ferromagnetic barrier of thickness a and magnetic thickness $d = a + 2\lambda$, where λ is the London penetration depth. The junction's lateral size is L. The field is applied in the y direction, and the current across the junction flows in the z direction. The phase φ is modulated along the x direction.

density

$$\mathbf{j}(x, y) = j_C(x, y) \sin(\varphi_0 + kx)\, \hat{\mathbf{z}},$$

where $k = (2ed\mu_0/\hbar)H$, φ_0 is the Josephson phase in the absence of the magnetic field, and $j_C(x, y)$ is the critical current density. The magnetic barrier thickness is $d = a + 2\lambda$, where a is the barrier thickness and λ is the London penetration depth, for the superconducting electrodes of thickness d_S larger than λ. When $d_S \sim \lambda$ we have $d = 2\lambda \tanh(d_S/2\lambda) + a$. The Fourier transform of the Josephson current across the junction $I(k)$, where k contains the influence of the magnetic field, is obtained when integrating the current density

$$\begin{aligned} I(k, \varphi_0) &= \int_{-L/2}^{L/2} dx \int_{-L/2}^{L/2} dy\, j(x, y) \sin(\varphi_0 + kx) \\ &= \Im m \left[\exp(\imath\varphi_0) \int_{-L/2}^{L/2} dx \left(\int_{-L/2}^{L/2} dy\, j(x, y) \right) \exp(\imath kx) \right], \end{aligned} \tag{1.4}$$

where L is the junction's lateral dimension in the x and y direction. We are only interested

in the spatial modulation of the current density due to the field, so we integrate along the field direction

$$J(x) = \int_{-L/2}^{L/2} j(x,y)dy.$$

Maximizing the expression Eq. (1.4) with respect to φ_0, we see that the maximum critical current dependence on k (or the magnetic field H) is given by

$$I_C(k) = \left| \int_{-\infty}^{\infty} dx J(x) \exp(\imath kx) \right|. \tag{1.5}$$

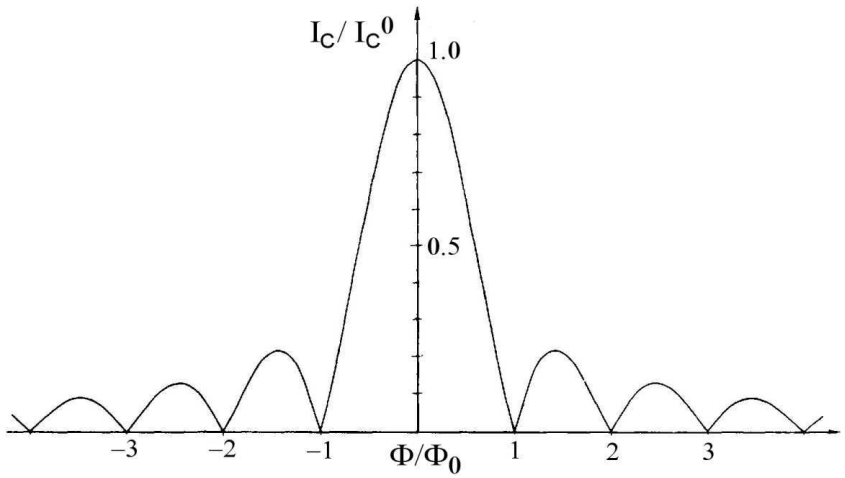

Figure 1.6: The expected critical current dependence on the external flux for a rectangular junction with uniform current distribution, Eq. (1.6).

For a uniform current distribution $J(x) = J_0$

$$I_C = I_C^0 \left| \frac{\sin(kL/2)}{kL/2} \right| = I_C^0 \left| \frac{\sin(\pi\Phi/\Phi_0)}{\pi\Phi/\Phi_0} \right|, \tag{1.6}$$

where $\Phi = dLH$ is the flux through the junction, $I_C^0 = J_0 L$, and $\Phi_0 = h/2e$ is the flux quantum. The maximum critical current I_C^0 is obtained for $H = 0$. This expression is analogous to the expression for the intensity of light on a distant screen, after passing through a rectangular slit with dimensions comparable to the wavelength, showing the Fraunhofer

diffraction, Fig. 1.9.

1.1.7 Josephson junction within the Resistively Capacitively Shunted Junction (RCSJ) model

Within the framework of the Resistively Capacitively Shunted Junction model (RCSJ)[53, 54, 55, 56], the current-biased Josephson junction is modeled by an ideal Josephson junction, a resistance and a capacitance in parallel, Fig. 1.7. The current balance is then

$$C\,\frac{dV}{dt} + \frac{V}{R} + I_C \sin\varphi = I_b, \tag{1.7}$$

where C is the junction capacitance, R the resistance, and I_b the bias current. The model itself does not specify the nature of the resistance, it is in fact the total resistance shunting the junction, which can be dominated by the normal resistance R_n, the quasiparticle resistance R_{qp} or the dissipative junction environment. In our case, it is the quasiparticle resistance R_{qp} which is dominant, as we show later.

The Josephson junction is a nonlinear inductance. We see this if we consider the change in current corresponding to the voltage across the junction, $V = L_J\,dI/dt = (\hbar/2e)\,d\varphi/dt$, where L_J is the Josephson inductance. Using the first Josephson relation, we get $L_J = \hbar/2eI_C\cos\varphi$.

We can rewrite this equation in dimensionless variables and in terms of phase using the second Josephson relation $\dot{\varphi} = (2e/\hbar)V$ as

$$\ddot{\varphi} + \beta\dot{\varphi} + \sin\varphi = \eta_b, \tag{1.8}$$

where $\eta_b = I_b/I_C$, $\beta = (RC\omega_0)^{-1}$, $\omega_0 = \sqrt{2eI_C/\hbar C}$ and the dot denotes $d/d\tau$, where $\tau = \omega_0 t$. This equation describes the movement of the phase in the tilted-washboard potential $U(\varphi) = U_C(1-\cos\varphi-\eta_b\varphi)$, with the Josephson energy $U_C = (\hbar/2e)I_C$, and damping β (Fig.

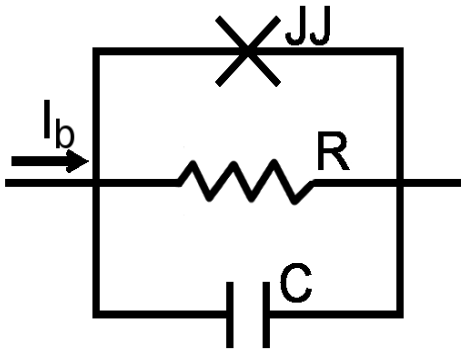

Figure 1.7: RCSJ model: A current I_b biased Josephson junction is modeled as an ideal Josephson junction JJ, a resistance R and a capacitance C in parallel.

1.13). The Josephson phase is oscillating in the local minimum with an attempt frequency $\omega_a = \omega_0(1-\eta_b^2)^{1/4}$ to go over the barrier $\Delta U = U_C(\eta_b(2\sin^{-1}\eta_b - \pi) + 2\cos(\sin^{-1}\eta_b))$. In the limit $I \to I_C$, the potential barrier can be approximated as $\Delta U = \frac{2}{3}U_C(2-2\eta_b)^{3/2}$. While the phase is oscillating in the minimum it has $\langle\dot{\varphi}\rangle = (2e/\hbar)V = 0$, therefore it is in the non-dissipative regime, so called locked state. The passage over the potential barrier corresponds to switching into the dissipative regime, t.i. the running state.

We can distinguish two types of behavior, depending on the value of the quality factor $Q = \omega_0 RC = \beta^{-1}$. (Note that damping β is distinct from the Stewart-McCumber factor $\beta_c = Q^2$.) For $Q > 1$ the phase dynamics is underdamped. Once over the barrier, the phase has sufficient kinetic energy $\langle\dot{\varphi}\rangle^2/2C$ that the damping is not enough to retrap it in the next potential well. The IV curve is hysteretic, with the retrapping current I_r smaller than the critical current by a factor of Q. For $Q < 1$ the dynamics is overdamped, the phase always gets retrapped in the next potential well and its movement is analogous to Brownian diffusion in metastable wells.

In the case of overdamped Josephson junctions, the capacitance is negligible, so the Josephson element is shunted only by the resistance R. (The model's name changes accordingly into Resistively Shunted Junction model - RSJ.) Then the first term in Eq. (1.7) is zero,

and the corresponding phase differential equation is first order

$$\beta\dot{\varphi} + \sin\varphi = \eta_b. \tag{1.9}$$

We integrate it directly from $t = 0$ to $t = T$, where T is the period of time for which the phase augments by 2π, to obtain $\varphi(t)$. Then we use the identity $2eV/\hbar = 2\pi/T$ to write the equation in terms of current and voltage, thus obtaining the IV curve of an overdamped junction

$$I(V) = \sqrt{{I_C}^2 + \left(\frac{V}{R}\right)^2}. \tag{1.10}$$

For large V it can be approximated by

$$I(V) = \frac{V}{R} + \frac{I_C^2\, R}{2V}. \tag{1.11}$$

For overdamped junctions, the IV curve is not hysteretic.

1.2 Coupling between the spin wave modes and the Josephson current

In Fig. 1.8 we illustrate the principle of experiment. The Josephson current passing through the junction excites the spin-wave modes, which in turn get rectified by the Josephson junction, resulting in a dip in the dynamical resistance at the spin-wave frequency.

We shall deconstruct this experiment on several different levels. In the first picture we will develop it as a dynamical Fraunhofer-type experiment. The Fraunhofer experiment is an optical experiment measuring the intensity of light through a small rectangular aperture, showing interference effects. Analogous interference takes place in a Josephson junction between different phase trajectories, leading to a Fraunhofer-like dependence of the critical

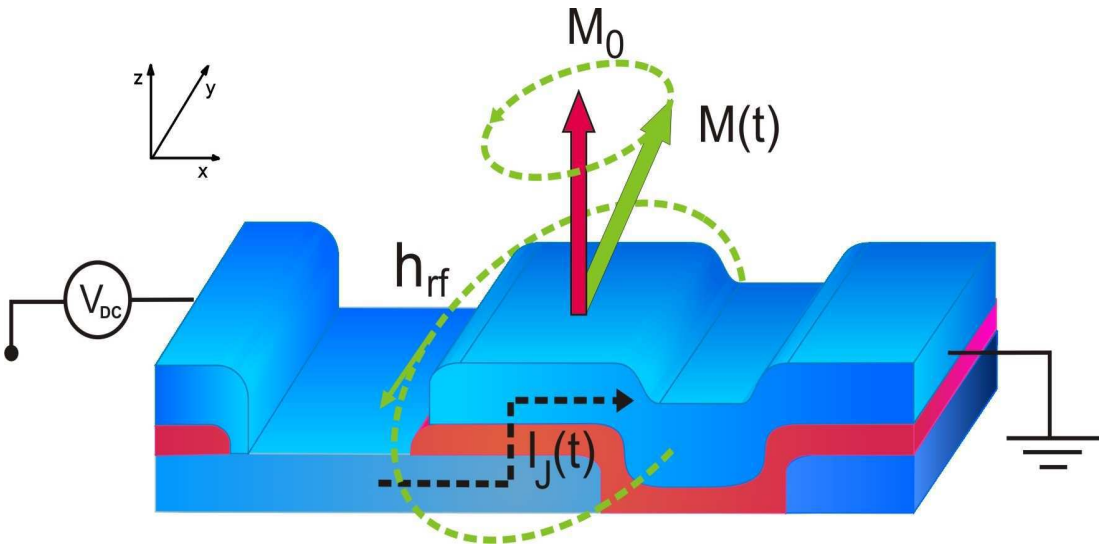

Figure 1.8: Schematic of the principle of experiment, showing the actual geometry of the ferromagnetic Josephson junction used. The blue layers are Nb and the red layer is PdNi. The Josephson current passing through the junction excites the spin-wave modes, which in turn get rectified by the Josephson junction, resulting in a dip in the dynamical resistance at the spin-wave frequency.

current upon the applied magnetic field. In the experiment, we shall consider a dynamical Fraunhofer effect, treating the magnetization dynamics as small movements along the Fraunhofer curve, since the x-axis, the flux, becomes time-dependent.

The second approach will be from the standpoint of the RSJ model - we shall describe an equivalent circuit with a frequency-dependent complex impedance that takes into account the magnetization dynamics.

Then we shall see it as a Ferromagnetic Resonance (FMR) experiment performed with a Josephson junction both as the source of excitation and the detection element. To that end we shall lay out the principle of the conventional cavity FMR experiment and make the analogy with our experiment.

And finally, the most elaborate approach is based on the calculation performed by Barnes and Maekawa[57], where they combined the Josephson relations with the Maxwell equations, explaining the resonant dips at the spin-wave frequency that we measured. The various

aspects of this calculation reflect the intuitive Fraunhofer and effective circuit pictures.

There have been propositions[58, 59] and attempts to measure the coupling of the magnetization dynamics and the Josephson current[60, 61, 62].

The dynamics of the magnetization (0.1 – 1 ns) is much slower than the diffusion time through the ferromagnetic layer (0.5 ps). There is a negligible change in the magnetization as Cooper pairs transit the ferromagnetic layer, justifying the adiabatic approximation. There have been calculations [63, 64, 65, 66] of the interaction between a single precessing spin and a Cooper pair when their timescales are comparable. The influence of the single spin on the Josephson current is the appearance of a current term proportional to $\langle S_z \rangle$, where the direction z is that of an external field H, perpendicular to the current direction. The ac Josephson current across the single spin has the so-called Josephson frequency $\omega_J = 2eV/\hbar$ determined by the applied voltage V (as in any Josephson junction). Finer effect is the dephasing of spin due to the passage of two consecutive electrons forming a Cooper pair, leading to the breathing of the spin component $\langle S_z \rangle$ with the Josephson frequency ω_J in addition to the Larmor precession with the frequency $\omega_L = \gamma_e H$. We, however, always stay in the adiabatic regime where the passage of the whole Cooper pair is considered as instantaneous, and under these conditions the spin should display only the Larmor precession and the $\langle S_z \rangle$ component should remain constant.

1.2.1 Fraunhofer picture

Consider light being diffracted from a single slit of length $\tilde{L}$. In general, for any type of slit, we take x' and y' to be the coordinates in the slit plane and x and y in the screen plane, ζ the amplitude through the slit, and ψ the amplitude at the screen. In the small-angle limit, where the slit is much smaller than the distance between the slit and the screen $\tilde{D}$, t.i. $x/\tilde{D} \ll 1$, $y/\tilde{D} \ll 1$, the amplitude at the screen is the Fourier transform of that at the slit

$$\psi(x,y) = C\int \zeta(x',y')e^{-\imath\tilde{k}(xx'+yy')/\tilde{D}}\,dx'dy', \tag{1.12}$$

where $\tilde{k}$ is the wave number and C is a constant. For a single slit of length $\tilde{L}$ and incident amplitude $\zeta = 1$ we have

$$\psi = C\tilde{L}\int_{-\tilde{L}/2}^{\tilde{L}/2} e^{-\tilde{k}xx'/\tilde{D}}\,dx' \;=\; C\tilde{L}\,\frac{\sin\frac{\tilde{k}\tilde{L}}{2\tilde{D}}x}{\frac{\tilde{k}\tilde{L}}{2\tilde{D}}x}. \tag{1.13}$$

The diffraction pattern is shown in Fig. 1.9.

Now we insert a wedge-shaped phase plate in front of the slit, with a refractive index n and width $a+bx$ as function of x, where a and b are constants. So instead of $\Delta\phi = \tilde{k}x = (2\pi/\lambda)\,x$ we now have

$$\Delta\phi = 2\pi\left(\frac{1-n}{n}\right)\frac{a+bx}{\lambda} \tag{1.14}$$

and therefore

$$\psi = C\tilde{L}\int_{-\tilde{L}/2}^{\tilde{L}/2} e^{-\tilde{k}\left(\frac{1-n}{n}\right)(a+bx)\left(\frac{x'}{\tilde{D}}\right)}\,dx' \;=\; C\tilde{L}\,\frac{\sin\frac{\tilde{k}\tilde{L}}{2\tilde{D}}\left(\frac{1-n}{n}\right)(a+bx)}{\frac{\tilde{k}\tilde{L}}{2\tilde{D}}\left(\frac{1-n}{n}\right)(a+bx)}. \tag{1.15}$$

The Fraunhofer maximum is shifted from the center by $-a/b$.

In analogy to the diffraction of light through a rectangular slit, the phase difference across the Josephson junction in the external magnetic field gets different path-dependent contributions, leading to the interference of the phase-dependent current[24].

In the external magnetic field, the gauge invariant phase has a field-dependent contribution

$$\varphi = \varphi_0 + \frac{2e}{\hbar}\int \mathbf{A}\cdot d\mathbf{l}.$$

As we have seen, for the in plane field $\mathbf{H} = \mathrm{H}\hat{\mathbf{y}}$, where $\hat{\mathbf{y}}$ is an unit vector in the y direction along the electrodes (and z is perpendicular to the junction plane, Figs. 1.5 and 1.8), we have the spatial modulation of the Josephson phase $\varphi \sim kx$ due to the applied field, where

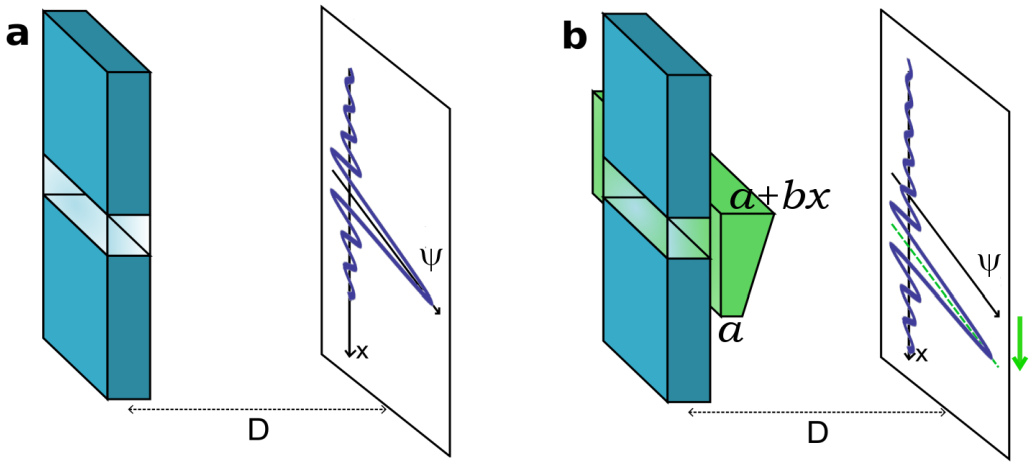

Figure 1.9: The Fraunhofer diffraction without (**a**) and with (**b**) a phase plate. When the phase plate is inserted, the optical paths are changed and the diffraction maximum is moved in the direction of the green arrow. The phase plate thickness as function of x is $a + bx$, where a and b are constants.

$$k = \frac{2ed\mu_0}{\hbar} H, \tag{1.16}$$

and where $d = a + 2\lambda$ is the magnetic thickness of the barrier, t.i. the part of the Josephson junction into which the field can penetrate. The actual thickness of the barrier is a, and λ the London penetration depth, see Fig. 1.5. We obtain the maximum current dependence on k (or the magnetic field H)

$$I_C(k) = \left| \int_{-\infty}^{\infty} dx J(x) \exp(\imath kx) \right|. \tag{1.17}$$

For a uniform current distribution $J(x) = J_0$

$$I = I_C^0 \left| \frac{\sin(kL/2)}{kL/2} \right| = I_C^0 \left| \frac{\sin(\pi\Phi/\Phi_0)}{\pi\Phi/\Phi_0} \right|, \tag{1.18}$$

where $\Phi = dLH$ is the magnetic flux through the junction, $I_C^0 = J_0 L$, and $\Phi_0 = h/2e$ is the flux quantum. The maximum critical current I_C^0 is obtained for $H = 0$. This expression is analogous to the optical result.

For a ferromagnetic Josephson junction, the magnetization of the ferromagnetic layer **M** also contributes to the phase. Again we start from the general expression

$$\varphi = \frac{2e}{\hbar} \int \mathbf{A} \cdot d\mathbf{l}, \tag{1.19}$$

where $\mathbf{B} = \mu_0(\mathbf{H} + \mathbf{M}) = \bigtriangledown \times \mathbf{A}$. We have then

$$\bigtriangledown\varphi = \frac{2e}{\hbar} \int \bigtriangledown (\mathbf{A} \cdot d\mathbf{l}) = \frac{2e}{\hbar} \int d\mathbf{l} \times (\bigtriangledown \times \mathbf{A}) = \frac{2e}{\hbar} \int d\mathbf{l} \times \mathbf{B}. \tag{1.20}$$

Looking at the junction geometry, the field $\mathbf{B} = B\hat{\mathbf{y}}$, and $d\mathbf{l} = dz\hat{\mathbf{z}}$, $d\mathbf{l} \times \mathbf{B} = -B\,dz\,\hat{\mathbf{x}}$, therefore

$$\frac{\partial}{\partial x}\varphi = -\frac{2e}{\hbar} \int B\,dz. \tag{1.21}$$

We now integrate the right side in z. First of all $B = \mu_0(H + M)$, and it is important to notice that H is nonzero between $(-d/2, d/2)$, since the magnetic field penetrates into the superconductor, while M is nonzero only between $(-a/2, a/2)$, the physical thickness of the ferromagnetic layer. We therefore have

$$\frac{\partial}{\partial x}\varphi = -\frac{2e\mu_0}{\hbar}(d\,H + a\,M). \tag{1.22}$$

Integrating now both sides in x we have

$$\varphi(x) = \varphi_0 - \frac{2e\mu_0}{\hbar}(d\,H + a\,M)\,x = \varphi_0 - k\,x, \tag{1.23}$$

where

$$k = \frac{2ed\mu_0}{\hbar}\left(H + \frac{a}{d}M\right), \tag{1.24}$$

is the ferromagnetic analog of Eq. (1.16), and φ_0 the integration constant. The magnetization in the Josephson junction is analogous to the wedge plate in front of the rectangular

slit for the optical diffraction. Maximum critical Josephson current $I_C(H)$ is obtained for $H + (a/d)M(H) = 0$. This equation in H has two solutions that differ only in sign. When we sweep the field in the two different directions, due to the hysteresis of the ferromagnetic layer $M(H)$, we see the current maximum I_C^0 shifted in two directions, corresponding to the positive and negative solutions $H^{\pm}$.

1.2.2 Conventional ferromagnetic resonance

The usual way of investigating the spin-wave spectrum of ferromagnetic films is the electron spin resonance (ESR). The principle of measurement is the following (Fig. 1.10). The sample is placed in an electromagnetic cavity in which a dc magnetic field $\mathbf{H_0}$ is applied perpendicular to the ac field $\mathbf{H_{ac}}$ that oscillates at the cavity resonant frequency $\nu_c = 9.46$ GHz. The sample is oriented such that its surface is parallel to $\mathbf{H_0}$, Fig. 1.10. In this configuration, the static magnetic field $\mathbf{H_0}$ lifts the electron Zeeman degeneracy and the ac field $\mathbf{H_{ac}}$ enables transition between the levels. We sweep the static field until we reach the resonance condition $h\nu_c = g\mu_B H_0$, where g is the gyromagnetic ratio, and μ_B the Bohr magneton. Then the sample absorbs the rf signal emitted by the cavity. A typical ESR signal is given on the right of Fig. 1.10, it is a power absorption peak usually measured in the first or second derivative as function of the dc field H_0.

The dynamics of the total magnetization is described by the Landau-Lifshitz (more precisely Bloch-Bloembergen) equation[67] with relaxation to local equilibrium

$$\frac{d\mathbf{M}}{dt} = -\gamma_e \mathbf{M} \times \mathbf{B_e} - \frac{1}{\tau}[\mathbf{M} - (M_z\hat{\mathbf{z}} + \chi_0 B_y \hat{\mathbf{y}})] \tag{1.25}$$

where $\mathbf{B_e} = B_0\hat{\mathbf{z}} + B_y\hat{\mathbf{y}}$ contains an effective static field $B_0 = \mu_0 H_0$ along with the driving field $B_y = \mu_0 H_{ac}$, and $\gamma_e = \mu_B/\hbar$. The static magnetization $\mathbf{M} = M_z\hat{\mathbf{z}}$. Using standard complex notation, these equations lead to, for the complex susceptibility

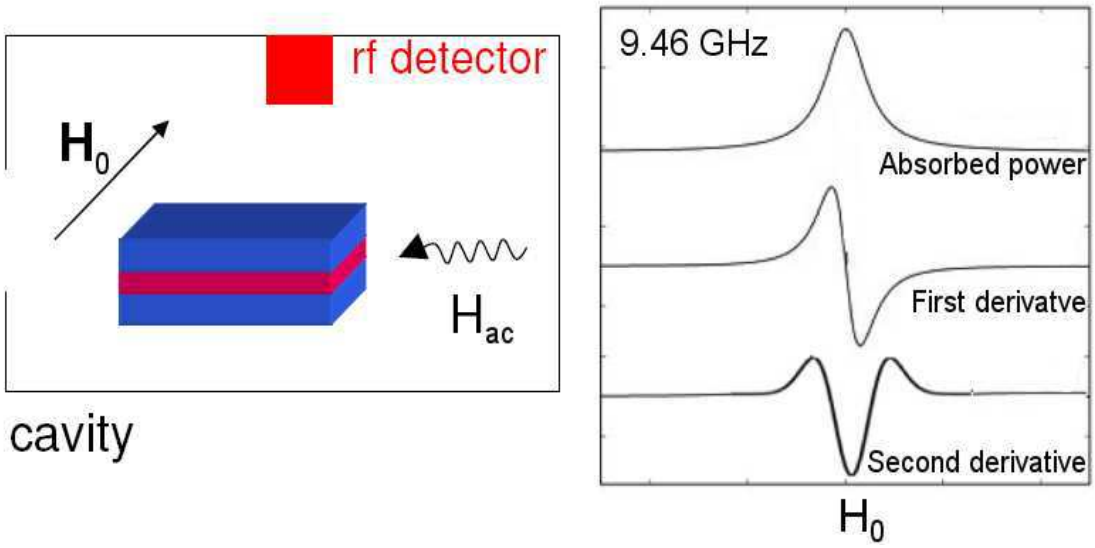

Figure 1.10: **Left**: Schematic of a conventional cavity ferromagnetic resonance experiment setup. The cavity emits microwaves at 9.46 GHz, and static magnetic field H_0 is swept perpendicular to the ac field H_{ac}. At the resonance, the sample absorbs microwaves. **Right:** A typical FMR signal, usually measured in the first or second derivative of the absorbed power as function of the applied dc field.

$$\chi_y(\omega) = \frac{\gamma_e M_z \omega_s + \frac{1}{\tau}\chi_0(i\omega + \frac{1}{\tau})}{(i\omega + \frac{1}{\tau})^2 + {\omega_s}^2}. \tag{1.26}$$

The dissipative, that is imaginary, part $\chi_y''(\omega)$ exhibits resonances at both $\pm\omega_s$. Provided the resonance width $\propto 1/\tau$ is not too large, the expression

$$\chi_y''(\omega) \approx \gamma_e M_z \left[\frac{(\frac{1}{\tau})}{(\omega_s - \omega)^2 + (\frac{1}{\tau})^2}\right] \tag{1.27}$$

is an adequate approximation and is used in the comparison with experiment.

For thin stripes of ferromagnetic films, the resonance spectrum is rather complicated, due to important effects of the demagnetization field[68, 69, 70]. In the case of weakly ferromagnetic PdNi with thickness $\sim$ 10 nm or less, it is plausible that stripe domains will form, with width $\sim$ 50 nm, due to dominantly perpendicular magnetization.

1.2.3 Toy model - effective circuit

In order to get a simple and intuitive picture of the experiment, we present an effective circuit model, in which we represent the ferromagnetic layer as a frequency-dependent complex impedance. The dynamic coupling which is the principal effect here, reflects phase shifts similar to the Fraunhofer ones due to $\mathbf{M}(\mathbf{r}, t)$, which now has both a temporal and a spatial dependence, the equivalent of a phase plate with a similarly dependent refractive index $n(\mathbf{r}, t)$ in the optical experiment.

We model the ferromagnetic layer as an impedance $Z_S(\omega)$, with a resonance at the characteristic spin-wave frequency ω_s. We model it as a series oscillator able to absorb at the resonant frequency ω_s, in parallel with the Josephson junction. Its dissipative part R_s is related to the imaginary part of the ferromagnetic susceptibility χ'', while its reactive part L_s, C_s to the real part χ'.

Starting from the RSJ model [56] and keeping in mind that the junction capacitance is negligible we have first without the impedance Z_S (therefore for a non-ferromagnetic junction)

$$I(V) = \sqrt{{I_C}^2 + \left(\frac{V}{R}\right)^2}, \tag{1.28}$$

where I_C is the critical current, and R is the Ohmic resistance. We develop this expression to the first order for large V

$$I(V) = \frac{V}{R} + \frac{I_C^2\, R}{2V}. \tag{1.29}$$

We want Z_S to be small at all frequencies except the resonant frequency ω_s. The impedance of the series resonator is

$$Z_S = R_s + \imath(\omega L_s - \frac{1}{\omega C_s}).$$

The total impedance is then

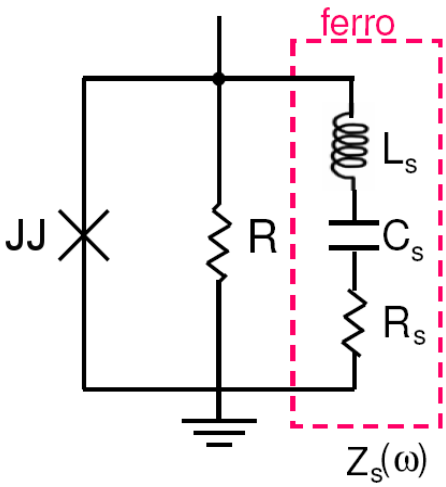

Figure 1.11: The effective circuit taking into account the impedance $Z_S(\omega)$ coming from the ferromagnetic layer.

$$\frac{1}{Z} = \frac{1}{Z_S} + \frac{1}{R}.$$

If we assume that $|Z_S| \gg R$, i.e. in the case of weak absorption, then

$$Z = R\left(1 + \frac{R}{Z_S}\right)^{-1} \approx R - \frac{R^2}{Z_S} = R - \frac{R^2}{R_s + \imath\left(\omega L_s - \frac{1}{\omega C_s}\right)}.$$

The real part is then

$$\Re eZ = R - R^2 \frac{\frac{\omega}{R_s C_s}}{\left(\frac{\omega}{R_s C_s}\right)^2 + \left(\omega^2 - \omega_s^2\right)^2}. \tag{1.30}$$

Coming back to the RSJ model, we have

$$I(V) = \frac{V}{R} + \frac{{I_C}^2}{2V}\Re eZ. \tag{1.31}$$

At fixed voltage, the resonant rise in impedance Z_S will produce a depression in the overall current. We simplify the ferromagnetic term rewriting it as a lorentzian with amplitude A, width σ and resonant frequency ω_s, so that

$$\Re eZ = R - \frac{2V}{I_C}\frac{\tilde{A}\sigma}{\sigma^2 + (\omega - \omega_s)^2}.$$

We have a depression in the IV curve

$$I(V) = \frac{V}{R} + \frac{{I_C}^2}{2V}R - I_C \frac{\tilde{A}\,\sigma}{\sigma^2 + (\omega - \omega_s)^2}. \tag{1.32}$$

We have used $V \sim I_C R$. We find later that $\tilde{A}$ is also proportional to I_C, so the resonant dip (third term) is proportional to I_C^2.

1.2.4 Theory of coupling between the Josephson current and the ferromagnetic resonances

Barnes and Maekawa[57] have developed a theory to describe the experiment which combines the Josephson relations with the Maxwell equations for the relevant range of parameters. The following is reproduced from the notes of Prof. Barnes.

The problem is formulated using the Landau-Ginzburg, rather than the simpler London formalism in order to use the gauge $\mathbf{A} = A(\mathbf{r}, t)\hat{\mathbf{z}}$. Within the Landau-Ginzburg approach[19], the velocity $\mathbf{v_s}$ of the superconducting electrons is given by

$$m^* \mathbf{v_s} = \hbar(\nabla\phi - \frac{2e}{\hbar}\mathbf{A}) \tag{1.33}$$

and, with this gauge, the gradient of the phase in the z-direction is non-zero (see Figs. 1.5 and 1.8). The current in the barrier is taken[71] to be proportional to $|\Delta|^2 e^{i(\phi_1(x,y;t) - \phi_2(x,y;t))}$. It is assumed $|\Delta|$ and the tunneling matrix elements for Cooper pairs are uniform.

It is necessary to determine the appropriate boundary conditions for the approximate solutions of Maxwell's equations. For reasons of transparency, it is not at all useful to solve the very difficult problem in which the solution within the barrier is matched to that in the exterior region to the junction. Within the junction we can ignore the displacement and transport currents since the wavelength of light λ and the skin depth δ are both larger

than the dimensions of the junctions at the Josephson frequency ω_J. We observe that the impedance of the junction of $\sim 1\,\Omega$ is much smaller than 377 Ω of free space and as a consequence there is essentially no radiation from the junction. The displacement current, and evidently the transport current can therefore be also ignored in the exterior region. It is therefore only necessary to integrate Ampère's circulation law for the Josephson current

$$\nabla \times \mathbf{H} = J_C \sin\phi(\mathbf{r},t)\hat{\mathbf{z}} \tag{1.34}$$

where $\phi(\mathbf{r},t) = kx + \omega_J t + \phi_1$.

Required is the additional phase shift[28]

$$\phi_1 = \frac{2e}{\hbar}\int_{\mathbf{r}}^{\mathbf{r}+a\hat{\mathbf{z}}} \mathbf{A^1}\cdot d\mathbf{r} = \frac{2ae}{\hbar}A_z^1, \tag{1.35}$$

with the magnetic system reflected in $\mathbf{A^1}$. In linear response appropriate to our experiments, ϕ_1 is considered as a perturbation and the signal is contained in

$$I_1 = \frac{2ae}{\hbar}\int_{-L/2}^{L/2} dx \int_{-L/2}^{L/2} dy \cos(kx+\omega_J t)\phi_1 \tag{1.36}$$

The determination of $\mathbf{A^1}$ requires first the vector integration of $\nabla \times \mathbf{H} = J_C \sin\phi(\mathbf{r},t)\hat{\mathbf{z}}$ and then $\nabla \times \mathbf{A} = \mathbf{B}$ with $\mathbf{B} = \mu_0(\mathbf{H}+\mathbf{M})$. Even with the simplifications of the previous paragraph, this is an involved calculation. It is useful to make some formal manipulations in order to avoid this double integration. In a complex notation where J_z is the imaginary part of $J_C e^{i(kx+\omega_J t)}$, the $J_C\cos(kx+\omega_J t)$ is the imaginary part of iJ_z and so the total current signal is

$$I_1 = \frac{2ae}{\hbar}\int_{-L/2}^{L/2} dx \int_{-L/2}^{L/2} dy [\Im m(i\vec{\nabla}\times\vec{H})]\cdot[\Im m(\vec{A})] \tag{1.37}$$

using Ampère's law $\mathbf{J} = \nabla \times \mathbf{H}$. Note, importantly, the imaginary parts are to be taken before the dot-product and integral. Noting, corresponding to a zero Poynting vector, either

$\mathbf{H}$ or $\mathbf{E}$ (and hence $\mathbf{A}$) are zero on the surface, this is integrated by parts using $\nabla\cdot(\mathbf{A}\times\mathbf{H}) = \mathbf{H}\cdot\nabla\times\mathbf{A} - \mathbf{A}\cdot\nabla\times\mathbf{H}$. Then substituting, $\nabla\times\mathbf{A} = \mathbf{B}$ and $\mathbf{B} = \mu_0(\mathbf{H}+\mathbf{M})$ we have that the signal is the average part of

$$I_1 = -\frac{2ae}{\hbar}\int_{-L/2}^{L/2} dx \int_{-L/2}^{L/2} dy[\Im m(i\mathbf{H})]\cdot[\Im m(\mathbf{M})], \tag{1.38}$$

which requires only a single integration of $\nabla\times\mathbf{H} = J_C \sin\phi(\mathbf{r},t)\,\hat{\mathbf{z}}$.

We use the expansion

$$J_s = J_C\sin(kx+\omega_J t) = J_C(\sin kx\cos\omega_J t + \cos kx\sin\omega_J t)$$

and treat the $\sin kx$ and $\cos kx$ part separately. We need to integrate $J_C\sin kx\cos\omega_J t$ to give

$$\mathbf{H_e} \equiv -J_C\frac{\cos kx - \cos k\frac{L}{2}}{k}\cos\omega_J t\,\hat{\mathbf{y}}.$$

The constant of integration was chosen to give zero when $x = L/2$. This is appropriate since the field at the edges reflects uniquely the average current and the odd part contains no such average. This is not the case for $J_C\cos kx\sin\omega_J t$ which has a finite average current density proportional to $(1/L)\int_{-L/2}^{L/2} dx\cos kx = (2/kL)\sin(kL/2)$. Using symmetry considerations, it must be that the integration of the constant part is

$$J_C\frac{\sin\frac{kL}{2}}{\frac{kL}{2}}\frac{1}{2}(x\hat{\mathbf{y}} - y\hat{\mathbf{x}})\cos\omega_J t$$

with half of the average being accounted for by the y-component. We therefore integrate $J_C(\cos kx - (2/kL)\sin kL/2)\sin\omega_J t$ to give

$$\mathbf{H_o} \equiv J_C\left(\frac{\sin kx}{k} - \frac{\sin\frac{kL}{2}}{\frac{kL}{2}}x\right)\sin\omega_J t\hat{\mathbf{y}}$$

The "i" in the formula for the signal changes $\sin\omega_J t \to \cos\omega_J t$ and so the $\hat{\mathbf{y}}$ component of

the real part of the iH_y is

$$\left[-J_C\frac{\cos kx-\cos k\frac{L}{2}}{k}\sin\omega_J t+J_C\left(\frac{\sin kx}{k}-\frac{\sin\frac{kL}{2}}{\frac{kL}{2}}x\right)\cos\omega_J t\right]$$

while the similar magnetization

$$M_y=\mu_0\Big[J_C\frac{\cos kx-\cos k\frac{L}{2}}{k}(\chi_y'\cos\omega_J t-\chi_y''\sin\omega_J t)$$
$$+J_C\left(\frac{\sin kx}{k}-\frac{\sin\frac{kL}{2}}{\frac{kL}{2}}x\right)(\chi_y'\sin\omega_J t+\chi_y''\cos\omega_J t)\Big]$$

which involves both the real (dispersion) χ_y' and imaginary (dissipative) χ_y'' parts of the usual complex susceptibility[67]. In Eq. (1.38) the only part with a finite average is proportional to either $\sin^2\omega_J t$ or $\cos^2\omega_J t$ and so

$$I_1^y=-\mu_0\chi_y''{J_C}^2L^4\frac{2ae}{\hbar}(F_e+F_o)=-2\pi I_c\frac{\Phi_{\rm rf}}{\Phi_0}F_y\chi_y''(\omega_J) \tag{1.39}$$

where $F_y=(F_e+F_o)$, $\Phi_{\rm rf}=(aL)(\mu_0 I_c/L)$ and

$$L^3F_e=\int_{-L/2}^{L/2}dx\left(\frac{\cos kx-\cos k\frac{L}{2}}{k}\right)^2=\frac{L}{2k^2}+\frac{1}{k^3}\sin\frac{kL}{2}\cos\frac{kL}{2}+\left(\frac{1}{12}\frac{L}{k^2}-\frac{4}{k^4L}\right)\sin^2\frac{kL}{2}$$

while

$$L^3F_o=\int_{-L/2}^{L/2}dx\left(\frac{\sin kx}{k}-\frac{1}{kL}\sin k\frac{L}{2}x\right)^2=\frac{L}{2k^2}+\frac{L}{k^2}\cos^2\frac{kL}{2}-\frac{3}{k^3}\sin\frac{kL}{2}\cos\frac{kL}{2}.$$

The sum $F_y=(F_e+F_o)$ is plotted in Fig. 1.12, blue curve. We write it down in the simplified form

$$F_y=\frac{2}{x^2}\left[1+\sin\frac{x}{2}\cos\frac{x}{2}+\left(\frac{13}{12}-\frac{4}{x^2}\right)\sin^2\frac{x}{2}\right],\qquad x=kL \tag{1.40}$$

The similar integral for the x-response gives,

$$I_1^x=-2\pi I_c\frac{\Phi_{\rm rf}}{\Phi_0}F_x\chi_x''(\omega_J), \tag{1.41}$$

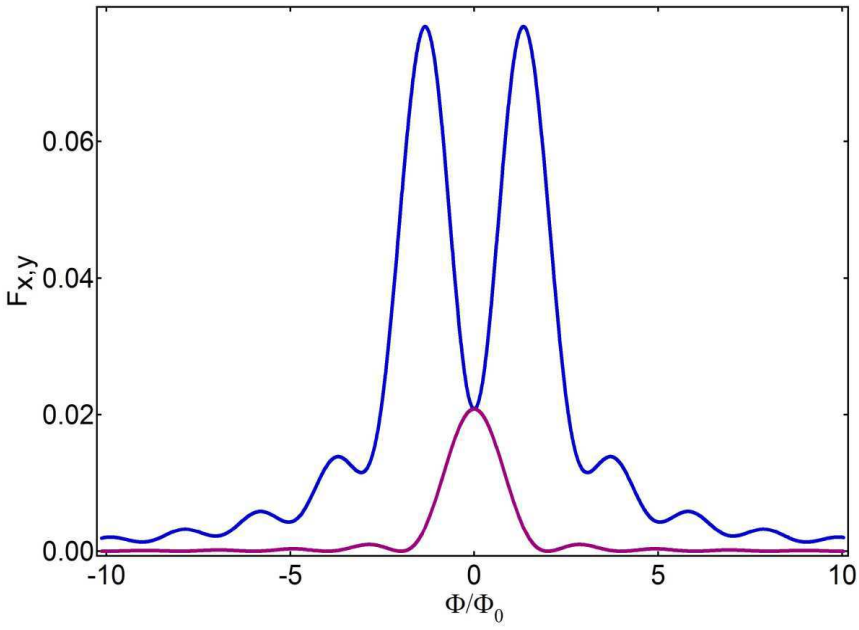

Figure 1.12: The response coefficients F_y in blue and F_x in purple, see Eqs. (1.40) and (1.42).

where

$$F_x = (1/12)(I_C(H)/I_C)^2, \tag{1.42}$$

also shown in Fig. 1.12, purple curve.

The coefficients F_x and F_y describe the geometry of the magnetic coupling to the Josephson current. Since the field is applied in the y direction, we obtain what is expected, that the response perpendicular to the field direction reflects the Fraunhofer pattern, and F_x is the square of $I_C(H)$. The response in the field direction is more pronounced. At zero field, both responses are equal.

1.3 Proper phase dynamics

The maximum dissipationless current that a Josephson junction can carry is not only given by the coupling energy between the two superconductors forming the junction but also by the dynamics of their phase difference. Thermal and quantum fluctuations of the phase, for instance, lower the value expected without fluctuations and set by the Josephson energy, $U_C = (\hbar/2e)I_C$, where I_C is the critical current. Furthermore, they introduce in a current-biased junction a probability distribution of the threshold current to switch into the dissipative state. Similarly, current and voltage noise from biasing also affect the phase dynamics and hence switching. Two timescales are pertinent: the inverse plasma frequency, and the phase relaxation time set by the junction damping. Since the plasma frequency is in the GHz range it is actually the microwave impedance, including the impedance of the junction environment, that sets the relaxation. However, in large area tunnel junctions, the effect of the environment is negligible as the quasiparticle resistance is much smaller than the vacuum impedance and the phase dynamics is intrinsic in the sense that it only depends on junction parameters.

1.3.1 Kramers problem - escape from the potential well

Within the framework of the Resistively Capacitively Shunted Junction model (RCSJ), we have at zero temperature the second order differential equation for the Josephson phase φ

$$\ddot{\varphi} + \beta\dot{\varphi} + \sin\varphi = \eta_b, \tag{1.43}$$

where $\eta_b = I_b/I_C$, damping $\beta = (RC\omega_0)^{-1}$, plasma frequency $\omega_0 = \sqrt{2eI_C/\hbar C}$ and the dot denotes $d/d\tau$, where $\tau = \omega_0 t$. This equation describes the movement of the phase in the tilted-washboard potential $U(\varphi) = U_C(1 - \cos\varphi - \eta_b\varphi)$, see Fig. 1.13. The Josephson phase is oscillating in the local minimum with an attempt frequency $\omega_a = \omega_0(1 - \eta_b^2)^{1/4}$ to go over

the barrier $\Delta U = U_C(\eta_b(2\sin^{-1}\eta_b - \pi) + 2\cos(\sin^{-1}\eta_b))$. In the limit $I \to I_C$, the potential barrier can be approximated by $\Delta U = \frac{2}{3}U_C(2-2\eta_b)^{3/2}$. While the phase is oscillating in the minimum it has $\langle\dot{\varphi}\rangle = (2e/\hbar)V = 0$, therefore it is in the non-dissipative regime, so called locked state. The passage over the potential barrier corresponds to switching into the dissipative regime, t.i. the running state.

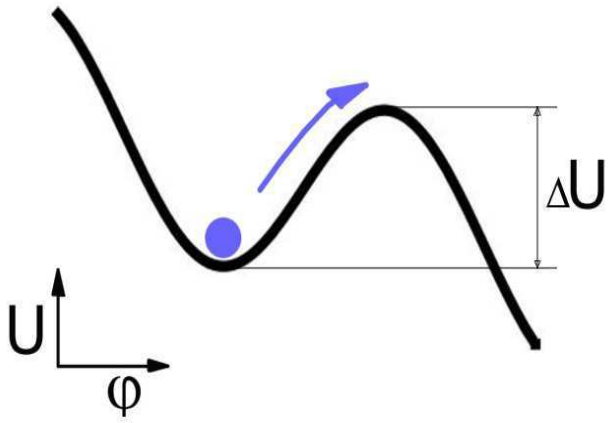

Figure 1.13: The phase in the tilted washboard potential. By thermal activation it goes over the barrier ΔU.

We can distinguish two types of behavior, depending on the value of the quality factor $Q = \omega_0 RC$. For $Q > 1$ the phase dynamics is underdamped. Once over the barrier, the phase has sufficient kinetic energy $\langle\dot{\varphi}\rangle^2/2C$ that the damping is not enough to retrap it in the next potential well. The IV curve is hysteretic, with the retrapping current I_r smaller than the critical current by a factor of Q. For $Q < 1$ the dynamics is overdamped, the phase always gets retrapped in the next potential well and its movement is analogous to Brownian diffusion in metastable wells. During the diffusion $\langle\dot{\varphi}\rangle \neq 0$, but since the phase is not in the free running state, when we know (or impose) the voltage across the junction we have determined (imposed) the phase. Another way to say this is that the IV curve is not hysteretic, so one value of voltage corresponds to a single value of current (phase).

There are two possible ways to activate the phase across the barrier - thermal activation and

quantum tunneling. The crossover temperature from the quantum to the thermal regime is $T^* = \hbar\omega_0/2\pi k_B$. From now on we shall be interested in the thermal regime.

Following the groundbreaking work of Kramers[72], we formalize the thermal activation across the barrier in the following way. For constant current bias the activation rate over the barrier is

$$\Gamma = \frac{\omega_a}{2\pi} \exp\left(-\frac{\Delta U}{k_B T}\right). \tag{1.44}$$

For adiabatically changing current bias, the phase has the Boltzmann distribution and we calculate the switching probability [73]

$$W(I(t)) = \exp\left[-\int_0^t \Gamma(I(t'))dt'\right] = \exp\left[-\int_0^I \frac{\Gamma(I')}{\dot{I}} dI'\right], \tag{1.45}$$

and the probability distribution

$$P(I) = -\frac{d}{dI} W(I) = \frac{\Gamma(I)}{\dot{I}} \exp\left[-\int_0^I \frac{\Gamma(I')}{\dot{I}} dI'\right], \tag{1.46}$$

where $\dot{I}$ is the speed with which we ramp the junction, the dot here denoting d/dt. In the adiabatic regime the ramp frequency is much smaller than both the plasma frequency and the inverse damping time.

Kramers distinguished the moderately underdamped from the extremely underdamped case (the criterion will be given shortly). Later were calculated the activation rates for all intermediate damping regimes[74, 75, 76]. In general, the escape rate can be expressed as

$$\Gamma = a_t \frac{\omega_a}{2\pi} \exp\left(-\frac{\Delta U}{k_B T}\right), \tag{1.47}$$

where the prefactor factor a_t is given in Table 1.1. Ruggiero, *et al.* [77] gave the conditions of validity for each regime.

The notable difference is that in the case of moderate damping the escape rate is independent

Damping	Validity range	a_t
Underdamped, low	$(\omega_a RC)^{-1} < 1,\ 2\pi\frac{\Delta U}{k_B T}\frac{\beta\omega_0}{\omega_a} < 1$	$2\pi\frac{\Delta U}{k_B T}\frac{\beta\omega_0}{\omega_a}$
Underdamped, moderate	$(\omega_a RC)^{-1} < 1,\ 2\pi\frac{\Delta U}{k_B T}\frac{\beta\omega_0}{\omega_a} > 1$	1
Overdamped	$(\omega_a RC)^{-1} > 1$	$\frac{\omega_a}{\beta\omega_0}$

Table 1.1: The criterion for crossover between different damping regimes and the prefactor a_t as given by Ruggiero, *et al.*[77].

of damping β, while for the extremely low and high damping this is not the case. For extremely low damping, $\beta \to 0$, we see that the thermal energy $k_B T$ plays an important role. The motion is almost conservative, and the energy lost in one cycle due to damping is much smaller than the thermal energy, $8\beta U_C \ll k_B T$, so mere thermal fluctuations stop the particle from getting retrapped. Also please note that the condition for crossover between the underdamped and overdamped regime is refined here - instead of comparing the quality factor $Q = RC\omega_0$ to 1, we are replacing the plasma frequency ω_0 with the attempt frequency ω_a. As the switching current approaches the critical current, the attempt frequency can be one or two orders of magnitude smaller than the plasma frequency.

In his paper[73], Garg gave a generic form of the activation rate

$$\Gamma(\eta_b) = A(1-\eta_b)^{a+b-1}\exp(-B(1-\eta_b)^b) \tag{1.48}$$

where the coefficients a, b, A and B are given in Table 1.2.

Escape parameters in the thermal regime				
Damping	A	B	a	b
Low	$\frac{18\beta\omega_0 U_C}{5\pi k_B T}$	$\frac{U_C}{k_B T}$	1	3/2
Moderate	$\frac{\omega_0}{2\pi}$	$\frac{U_C}{k_B T}$	-1/4	3/2
High	$\frac{\omega_0}{2\pi\beta}$	$\frac{U_C}{k_B T}$	0	3/2

Table 1.2: Escape parameters for various damping regimes for thermal activation[73].

In order to obtain analytical expressions for mean switching current $\langle I \rangle$ and standard deviation $\sigma = (\langle I^2 \rangle - \langle I \rangle^2)^{1/2}$, he approximated the activation frequency $\omega_a = \omega_0(1-\eta_b^2)^{1/4}$ with $\omega_a = \omega_0(1-\eta_b)^{1/4}$. This approximation is valid for $\eta_b \to 1$. The mean switching current $\langle I \rangle$ is then

$$\langle\, I \rangle \;=\; I_C \left[1 - \left(\frac{\log X}{B}\right)^{\frac{1}{b}}\right], \tag{1.49}$$

and the standard deviation σ is given by

$$\sigma^2 \;=\; I_C^2 \,\frac{\pi^2}{6b^2}\,\frac{(\log X)^{-2+\frac{2}{b}}}{B^{\frac{2}{b}}}, \tag{1.50}$$

where

$$X = \frac{I_C}{\dot{I}}\frac{A}{bB^{1+\frac{a}{b}}}.$$

The expressions for $\langle I \rangle$ and σ are asymptotic, with correction terms and the derivation to be found in the original paper. In the case of moderate damping we find, as expected, $\sigma \sim I_C^{1/3}\, T^{2/3}$.

It is not clear in the RCSJ model which resistance R governs the phase escape. We will show later that the relevant resistance in our experiment is R_{qp} – the quasiparticle resistance. Inherent to the RCSJ model is the supposition that there exists an effective constant resistance that describes the phase movement in the whole range of voltage. However, the real resistance of the junction is strongly nonlinear. For the Kramers intermediate damping regime, the question is not important, since the resistance does not enter in the activation rate, but for other damping regimes it is, and it is essential for the transition between the regimes[78, 79], since the resistance can be temperature dependent. It is also crucial for quantum tunneling, which is exponentially dependent on the resistance. In other experimental situations, the effective R may be any parallel internal or external (circuit) resistance.

1.3.2 Dynamical bifurcation regime

The nonlinear oscillator can enter into the bifurcation regime, meaning a small smooth change made to the parameter values or to the initial conditions of a system causes a sudden qualitative or topological change in its behavior. Bifurcation usually occurs when an anharmonic oscillator is driven at a frequency equal to its resonant plasma frequency, and it results in a resonant amplification of the oscillation amplitude. Out of equilibrium, in the dynamical regime, it is the initial kinetic energy that plays the role of the driving force. Two scenarios are possible, see Fig. 1.14 : either the phase relaxes to the bottom of the potential well leading to a switching current equal to that at equilibrium or the phase does not relax and escape occurs at a much smaller current bias of the order of the retrapping current. In strongly underdamped junctions the retrapping current can be vanishingly small. Out-of-equilibrium induced bifurcation depends on the bias frequency and damping.

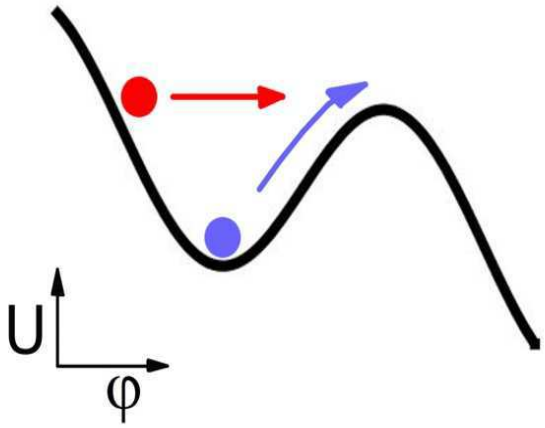

Figure 1.14: Tilted washboard potential and two bifurcation scenarios: the relaxation of phase to the bottom of the well, or jump over the potential well due to kinetic energy.

The phase dynamics of the current biased Josephson junction is that of a nonlinear driven oscillator,

$$\ddot{\varphi} + \beta\dot{\varphi} + \sin\varphi = 2\,\eta_b \left(\frac{\omega_b \tau}{2\pi} - \left[\frac{\omega_b \tau}{2\pi} \right] \right), \tag{1.51}$$

where ω_b is the ramp frequency. The bracket $[r]$ denotes the biggest integer smaller than r. We bias with a sawtooth ramp in the experiment, so we also write it here, but it would be the same if we used a sinusoidal ramp. The system being a nonlinear oscillator, with a suitable choice of parameters we can access bifurcation, or the chaotic regime. We shall focus only on bifurcation, which we measure. We have three pertinent time-scales, set by three characteristic frequencies: the plasma frequency ω_0, the inverse damping time β and the driving frequency ω_b. For the underdamped junctions we always have $\beta \ll \omega_0$. In the adiabatic regime the ramp is considered infinitely slow, $\omega_b \ll \beta$, while in the non-adiabatic regime it is comparable to the characteristic damping time, $\omega_b \sim \beta$. In our experiment $\omega_0/2\pi \sim$ GHz, while $\beta \sim 10$ – 100 kHz (when converted from ω_0 units), so the ramp frequency $\omega_b/2\pi$ goes from ~ 100 Hz in the stationary regime, up to ~ 10 – 100 kHz in the non-stationary regime.

Following Büttiker, *et al.* [74], we see that the underdamped Josephson junction biased with constant current smaller than its critical current has a possibility to be either in the locked, non-dissipative state or in the running, dissipative state. However, for a certain range of parameters, it can display bifurcation between the two, hence the hysteresis in the IV curve. The thermal noise has the role of activating one or the other state[80, 81]. We give in Fig. 1.15 the range of bistability for damping β as function of ramp amplitude η_b, as calculated in [74].

Since damping is very small in our junctions, of the order of 10^{-4} (in the plasma frequency units), we see in Fig. 1.15 that bistability is possible for almost any bias current. (Another way to say this is that the retrapping current is close to zero.) But we are interested in dynamical bistability. We measure it with a time-dependent current ramp. When the ramp time becomes comparable to the damping time, the junction has a finite probability of being in the locked or in the running state.

There were theoretical [82] and experimental [83] investigations of bistability induced by

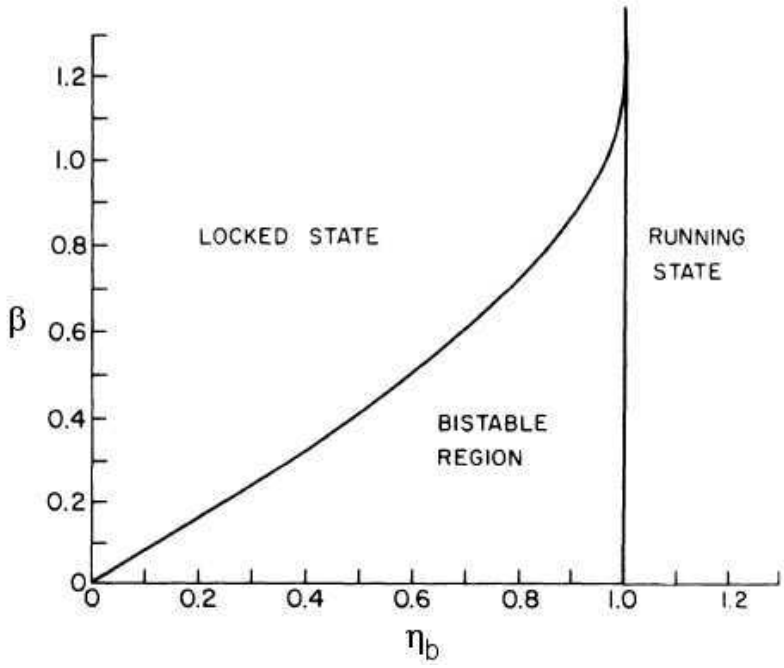

Figure 1.15: Range of bistability in the tilted washboard potential, in the space of parameters damping β and imposed current η_b [74].

external photon irradiation at subgap frequency, as well as experiments with a bifurcation amplifier by I. Siddiqi, *et al.* [84], where suitable microwave irradiation at frequency close to ω_0 excites the phase into large amplitude oscillations. The bifurcation is between the small amplitude oscillations at the bottom of the well, and large amplitude oscillations, and the Josephson junction in this experiment never goes into dissipation.

Bifurcation in Josephson junctions was theoretically investigated by Dykman [85, 86, 87, 88]. The Kramers form for the escape rate

$$\Gamma = \frac{\omega_a}{2\pi} \exp\left(-\frac{\Delta U}{k_B T}\right) \tag{1.52}$$

still holds, but the potential barrier ΔU and the activation frequency ω_a are redefined in the phase space. There has been extensive work in this direction for overdamped Josephson junctions, which are easier to solve, since the differential equation is only first-order[89]. Then we have

$$\dot{\varphi} = -\nabla V + \xi,$$

where V is the potential and ξ thermal noise, and the potential barrier $\Delta U = V(1) - V(2)$, where point (2) is at the bottom of the potential and (1) at the top. However, for the underdamped junctions the situation is more complicated, and we can say in general that ΔU is not a difference between the two potentials, but an integral of action S in the phase space corresponding to the attractor, t.i. the energetic cost of going over the barrier[90, 91].

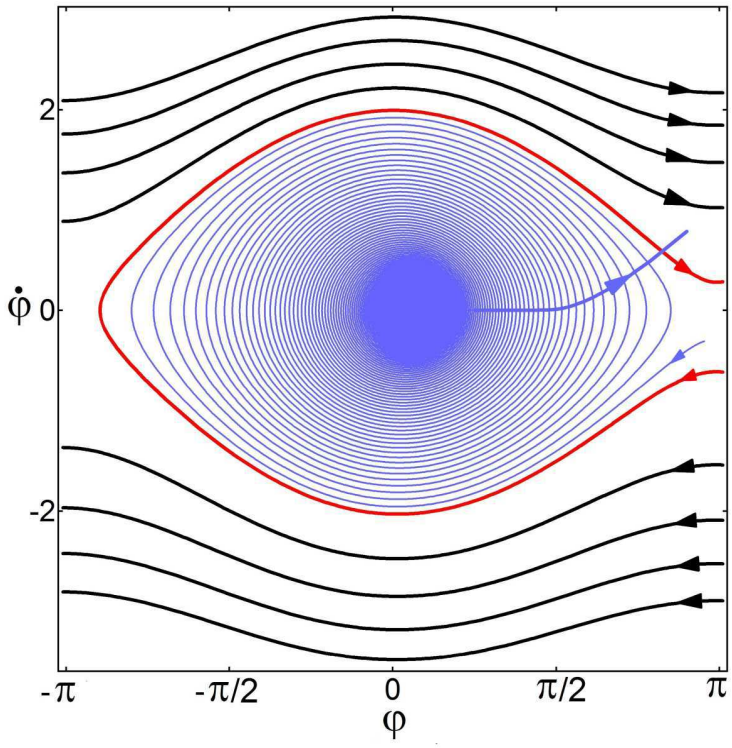

Figure 1.16: Phase space of the tilted washboard potential obtained by numerical simulation. The bifurcation means that sometimes the phase falls into the attractor (blue curves), while sometimes it stays on the separatrix (red curve). The black curves are in the dissipative regime.

We shall solve Eq. (1.51) numerically in Chapter 3, and make a correspondence with the experimental results. In Figs. 1.16 and 1.17 we show the phase diagram $(\varphi, \dot{\varphi})$ and $V(t)$ respectively, obtained by this calculation, in order to illustrate the mechanism of the effect.

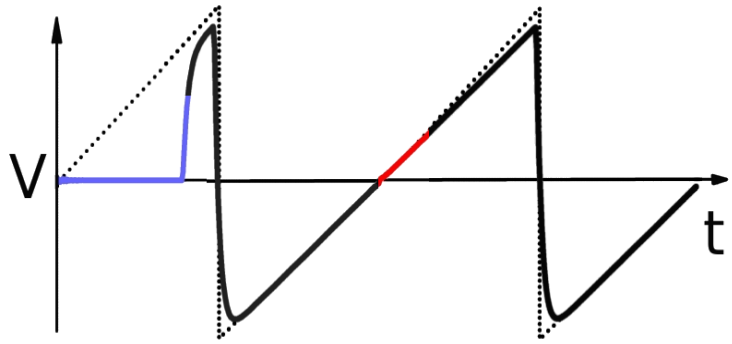

Figure 1.17: The voltage across the junction $V(t)$ corresponding to the previous Figure, that illustrates which parts of the $V(t)$ curve correspond to which parts of the phase space.

At the start of the cycle, the phase has some kinetic energy and its trajectory is one of the black curves, corresponding to dissipation. At some values of kinetic energy, due to damping, the phase will cross the red separatrix (retrapping branch) and fall into the blue attractor, corresponding to the locked state. At some others it will stay just outside, on the red retrapping branch, and bounce back into dissipation, t.i. one of the black curves.

1.3.3 Fiske resonances and dynamical bifurcation

Fiske resonances

Fiske resonance is a resonance between the Josephson current and the electromagnetic modes that propagate through the barrier as if it were a transmission line and form standing waves with the junction's lateral size[92, 93, 94, 95].

Following Tinkham[19] and Barone[96], we combine the Josephson relations and the Maxwell equations in order to describe the Josephson junction in the external magnetic field. If the magnetic field is applied along the y direction, whilst the direction z is perpendicular to the junction surface and parallel to the current j_z (see Fig. 1.5 for junction geometry), we have for magnetic field h_y and electric field e_z in the barrier

$$\frac{\partial e_z}{\partial x} = \frac{d}{a}\mu_0 \frac{\partial h_y}{\partial t} \qquad \frac{\partial h_y}{\partial x} = j_z + \epsilon \frac{\partial e_z}{\partial t},$$

where a is the physical thickness of the barrier and $d = a + 2\lambda$ its magnetic thickness, λ being the London penetration depth. Eliminating h_y and using $V = e_z a$, where V is the voltage across the junction, and integrating the whole equation in t whilst using the Josephson relation $\dot{\varphi} = (2e/\hbar)V$, we can write the dimensionless equation

$$\frac{\partial^2 \varphi}{\partial \tau^2} + \beta \frac{\partial \varphi}{\partial \tau} + \sin\varphi - \frac{\bar{c}^2}{\omega_0^2} \frac{\partial^2 \varphi}{\partial x^2} = 2\,\eta_b \left(\frac{\omega_b \tau}{2\pi} - \left[\frac{\omega_b \tau}{2\pi} \right] \right), \tag{1.53}$$

where $\bar{c}$ is the propagation speed of electromagnetic waves through the junction barrier, and time is given in the plasma frequency units as before, $\tau = \omega_0 t$. This is the driven sine-Gordon equation. We assume the solution in the form

$$\varphi = \varphi_0 + \omega\tau - kx,$$

where $\omega = (2e/\hbar)V$ and $k = (2ed\mu_0/\hbar)H$. The speed of propagation of the electromagnetic field through the barrier is

$$\bar{c} = \omega_0 \lambda_J = c\sqrt{\frac{a}{\epsilon_r d}},$$

where $\lambda_J = \sqrt{\hbar/2e\mu_0 d\, j}$ is the Josephson penetration depth, j being the current density, ϵ_r the relative dielectric constant and μ_0 the magnetic constant.

Due to the boundary conditions there is quantization of frequency

$$\omega_n = \frac{2e}{\hbar} V_n = n \frac{\bar{c}}{2L}, \tag{1.54}$$

where L is the lateral size of the junction. These are the Fiske resonance frequencies. Fiske resonances are between the Josephson oscillations and the electromagnetic standing waves with the junction's lateral size. In the IV curve at equidistant voltages $V_n = (\hbar/2e)\,\omega_n$ we

have current steps ${I_f}^n$.

Sine-Gordon equation and dynamical bifurcation

We can ask now what happens with the dynamical bifurcation when the junction also displays Fiske resonances. We have seen that the phase equation has changed from Eq. (1.51) to Eq. (1.53). The available states for bifurcation were the locked and the running state, while now we also have a multitude of Fiske resonances. We shall see that, in addition to the critical current branch and the retrapping branch, all the Fiske resonances present different branches and bifurcation enables hopping between them.

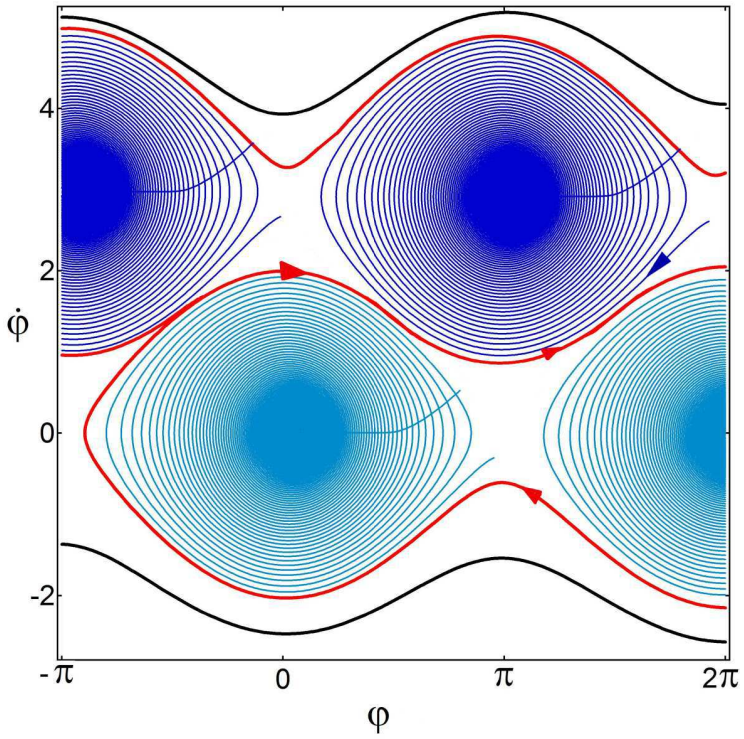

Figure 1.18: The schematics of the expected phase diagram in the presence of magnetic field. The dark blue attractors at finite voltage correspond to the Fiske resonances. Note that the Fiske attractors have not been obtained numerically.

In Fig. 1.18 we come back to the schematics of the phase diagram in the case we have Fiske resonances. (Note that the dark blue parts of this diagram are not a result of calculation).

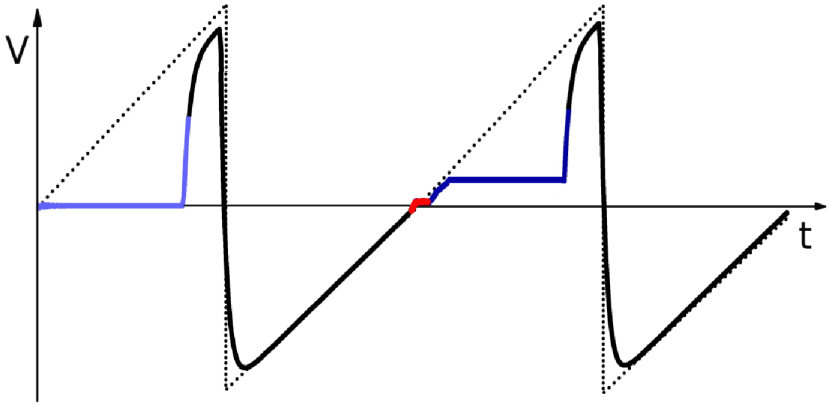

Figure 1.19: The expected $V(t)$ curve in presence of the Fiske resonances.

In addition to the locked state at $\langle\dot{\varphi}\rangle = (2e/\hbar)V = 0$, corresponding to the attractor given in light blue, we now have the possibility of locked states at finite V_n, corresponding to the attractors given in dark blue. So the phase has a choice either to fall into the attractor at zero voltage, or, due to its kinetic energy, to stay on the red line just above the attractor, and fall into the next attractor at finite voltage, corresponding to the Fiske branch. In reality there would also probably be a dissipative region between the two attractors. In Fig. 1.19 we show the corresponding $V(t)$ curve. This curve, however, is similar to the curves we measure, shown in Fig. 3.27.

And the final remark is that we may not always need the external magnetic field to have Fiske resonances. In the ferromagnetic Josephson junctions Fiske steps can appear in zero field. Also, we shall experimentally demonstrate that the dispersion relation in this case is $\omega_n = \varpi + n\bar{c}/2L$, with a constant shift ϖ compared to the non-ferromagnetic case, Eq. (1.54). This is due to the fact that the ferromagnetic layer influences the transmission of the electromagnetic waves through the junction barrier.

Chapter 2

Ferromagnetic Josephson resonance

2.1 Principle of experiment

The challenge addressed here is that of dynamically coupling two seemingly incompatible order parameters - superconductivity and ferromagnetism. We do that by coupling them locally on a nanometric scale in ferromagnetic Josephson junctions. The coupling is resonant between the Josephson phase and the characteristic modes, in particular the spin-wave modes. A magnetic resonance of frequency ω_s appears as a depression in the current-voltage curve of the Josephson junction when the applied voltage V is $\hbar\omega_s = 2eV$. The magnetic system is excited via singlet supercurrent and, through back-action, the Josephson junction plays the role of a detector in a resonance experiment on a thin layer of weak ferromagnet.

This Chapter contains the experimental results. First we demonstrate the static influence of magnetization on the Josephson critical current, producing a shift in the Fraunhofer pattern. Then we investigate the resonances in the IV curve, their behavior in the external magnetic field and with external microwave irradiation. We compare the results with standard Ferromagnetic Resonance (FMR) measurements on a similar albeit macroscopic reference trilayer. Finally, we look at the thermal noise properties of these small ferromagnetic junctions with overdamped phase dynamics.

2.2 Sample fabrication

We have fabricated sub-micron ferromagnetic Josephson junctions in ultra-high vacuum (UHV) using the technique of overlap angle evaporation. To that end, we have adapted a trilayer resist process described in the following. This process is quite demanding, but gives a high level of reproducibility and control. The reason we need this particular trilayer resist is the evaporation of Nb, which takes place at high temperatures, so we need a mask that will be able to endure this.

2.2.1 Mask preparation

The purpose of the mask is to produce hanging bridges and a large undercut, enabling angle evaporation. The hanging bridge's length is 500 nm and its width is around 400 nm, and needed undercut is 500 nm.

We have fabricated the mask using a trilayer resist technique[97] consisting of PES (Poly Ether Sulfone - commercially known as Victrex and often used to thermally insulate airplanes), a layer of rigid Si_3N_4 and a layer of electron-sensitive polymer PMMA (Poly Methyl Methacrylate). The resist PMMA is a standard electron positive resist (positive means that the irradiated parts are removed during lift-off) offering precision up to tens of nm. The polymer PES has several excellent properties. Although it can be used in its own right as a negative electron resist, we are not performing lithography on it. Its role is to support the rigid Si_3N_4 mask during evaporation, since it sustains high temperature. The mask is etched into it. The resist PES undergoes a glass transition at 235°C, and it is chemically stable up to 400°C. This is needed for the evaporation of refractory metal Nb, which heats the chamber during evaporation, and is very sensitive to contamination by oxygen and other compounds that could outgas from the mask. If we were to make a mask in PMMA alone, which is routinely done for the evaporation of Al, for example, it would melt or outgas during the evaporation of Nb. (In our process the PMMA is removed before evaporation.) The

layer of Si_3N_4 can be etched and provides rigid hanging structures. It offers good control of dimensions, stability and reproducibility. The trilayer is deposited on the silicon wafer with a thin oxide layer, and it consists of the 500 nm thick PES layer, followed by 60 nm of Si_3N_4 and then 350 nm of PMMA.

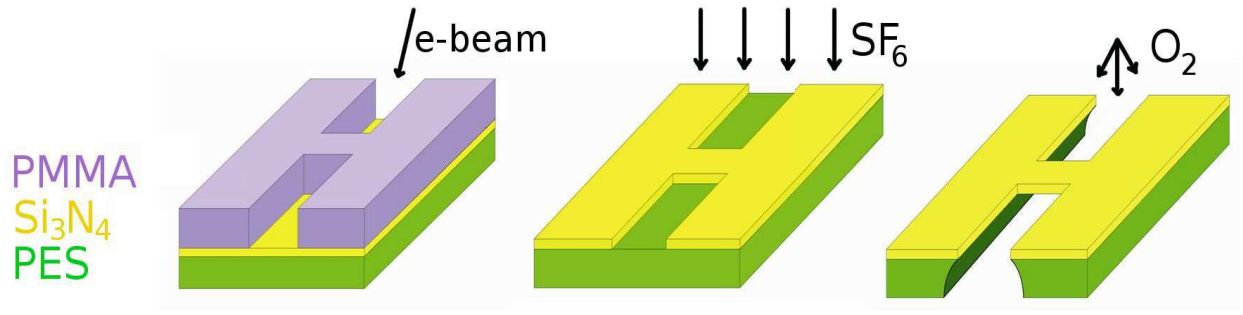

Figure 2.1: Stages of mask fabrication. From the left: **a)** Electron-beam lithography transmits the mask onto the PMMA layer. **b)** Directional Reactive Ion Etching (RIE) with SF_6 transmits the mask onto the Si_3N_4 and etches away the remaining PMMA. **c)** Isotropic RIE with oxygen plasma etches the mask all the way to the wafer, creating an undercut and leaving the Si_3N_4 layer intact. Colors represent different layers: green is for PES, yellow is for Si_3N_4 and violet is for PMMA.

The main stages of mask fabrication are illustrated in Fig. 2.1. First we performed electron-beam lithography with a Scanning Electron Microscope (SEM), drawing the pattern onto the PMMA layer. Then we etched the structure in the Reactive Ion Etching (RIE) chamber in several steps. The first step, directional etching with SF_6 plasma for 1 minute 30 seconds, transmitted the pattern onto the Si_3N_4 layer and removed the remaining PMMA. The second step, etching with oxygen plasma for 2 minutes, transmitted the pattern onto the PES leaving Si_3N_4 intact. The remaining etching of PES with oxygen plasma for 10 minutes (without a pause) created a 500 nm undercut in PES and suspended bridges, again only slightly thinning the Si_3N_4. In order to make oxygen etching isotropic and produce a sufficient undercut, we etched at a very high pressure of 300 mTorr.

The photo of the mask before the evaporation, showing seven junction masks in parallel, is given in Fig. 2.2, with a zoom on one junction mask on Fig. 2.3, showing a suspended

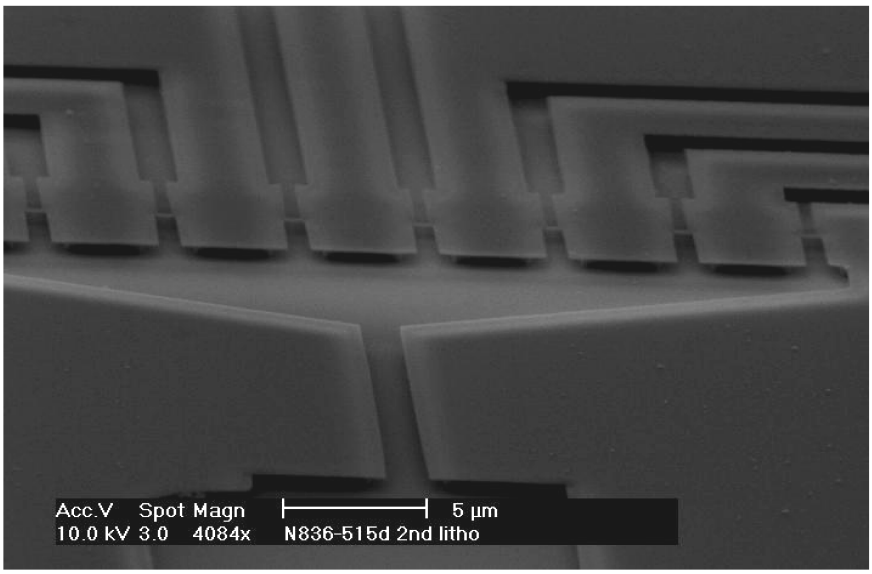

Figure 2.2: SEM photo of the mask before the evaporation showing seven junction masks in parallel, out of eight fabricated on the same wafer.

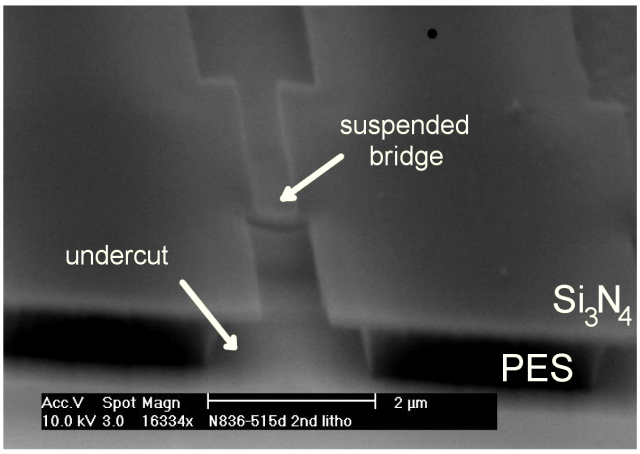

Figure 2.3: SEM photo of the mask for one junction, showing a suspended bridge in Si_3N_4 and a 500 nm undercut in the PES.

bridge and the undercut in the PES. Eight junction masks are fabricated on the same wafer.

The RIE was performed at Laboratoire de Photonique et Nanostructures (LPN) in Marcoussis, with the help of L. Ferlazzo. The detailed recipe is given in the Appendix.

2.2.2 Junction fabrication

We evaporated the junctions *in situ* in a custom-made UHV evaporator, under a base pressure of 10^{-9} mbar. We evaporated each layer of material onto the wafer under a different incident angle, and the overlap of different layers under a suspended Si_3N_4 bridge made up the junction. The evaporation angles are shown in Fig. 2.4, with the schematic drawing of the obtained cross-section in Fig. 2.5. First we evaporated 50 nm of Nb under the incident angle of -45° from the vertical axis, then we oxidized Nb for 10 minutes under the pressure of 10 mbar, then we evaporated 20 nm of PdNi under the angle of +45°, and finally another 50 nm of Nb under the angle of +47° to avoid shortcircuit between the two Nb layers. While evaporating Nb we used liquid nitrogen to cool down the walls of the evaporating chamber, ensuring better Nb quality. Finally 50 nm thick Nb layers had a critical temperature $T_C^{\text{leads}} = 7.3$ K. The liftoff is performed in a solution of NMP (N Methyl 2 Pyrrolidone), a solvent for PES. The Ni concentration has been measured by Rutherford Backscattering (RBS) on a test sample[98]. Further fabrication details are given in the Appendix.

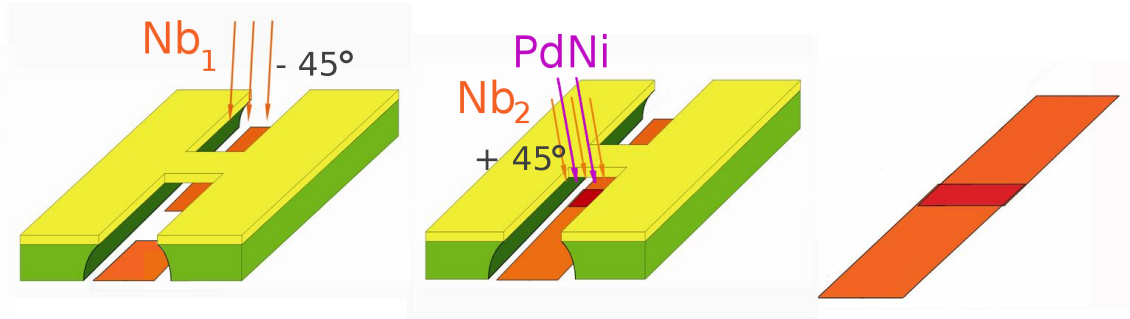

Figure 2.4: Stages of angle evaporation across a mask with a suspended bridge. From the left: **a)** First we evaporated 50 nm of Nb (layer marked as Nb_1) under the incident angle of -45° from the vertical axis. **b)** Then we evaporated 20 nm of PdNi under the angle of +45° followed by another 50 nm of Nb (Nb_2) under the angle of +47°. **c)** After lift-off, the mask is removed. Red region is the overlap defining the junction.

The junction is bonded with Al wires using an ultrasound soldering machine, and mounted on a dilution refrigerator probe. The dilution refrigerator is able to descend to 35 mK.

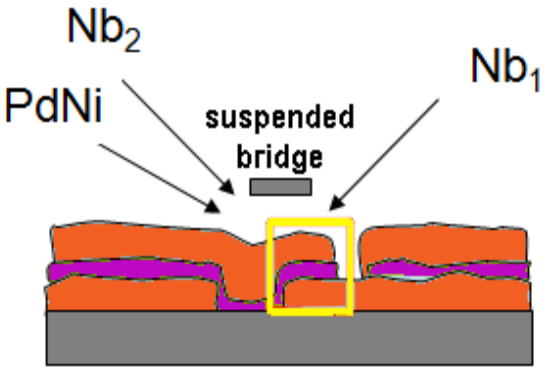

Figure 2.5: The cross-section after evaporation. Red layers stand for Nb, the index denoting the order in which the evaporation is performed, while the purple layer denotes the PdNi. The junction is indicated with a yellow square.

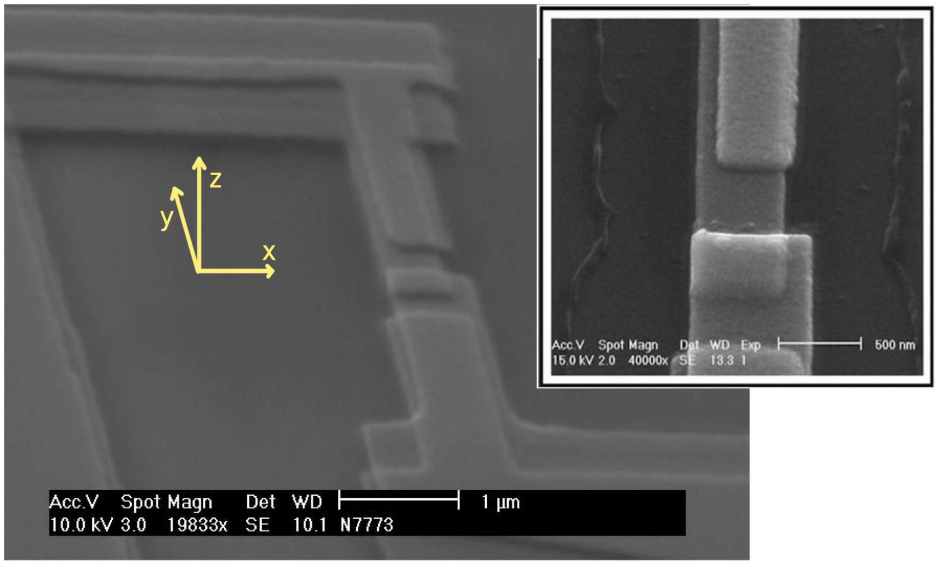

Figure 2.6: SEM photo of a fabricated junction with leads. Inset shows the zoom on the junction.

In Fig. 2.6 we show two SEM photos of the fabricated junctions, one showing a junction with leads, and another, in the inset, showing a zoom on the junction. The leads are gradually narrowing when approaching the junction, from millimetric bonding pads to micrometric leads shown here. The drawing of the whole wafer is given in the Appendix. Every junction has four different leads, enabling a four point transport measurement (two leads for current bias and two for voltage measurement). Leads are effectively trilayers due to the shadow

evaporation of PdNi, but the current passes through the superconducting Nb. The junction surface is 500 nm × 500 nm.

We show in Fig. 2.7 the characterization of junction J8 on the wafer I4.

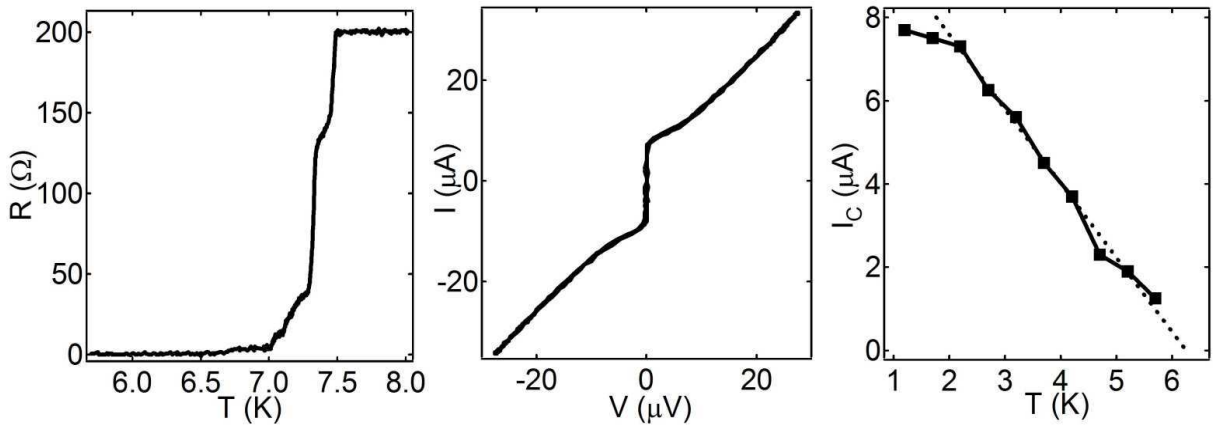

Figure 2.7: Junction characterization. **Left**: Resistance of the junction with leads as function of temperature. The junction critical temperature is $T_C = 6.5$ K, and the leads' critical temperature is $T_C^{\text{leads}} = 7.3$ K. The step at 7.5 K corresponds to a transition of wider leads. **Middle**: IV curve taken at 1.2 K. **Right**: Junction critical current as function of temperature.

On the first panel from the left we show the resistance of the junction with leads as function of temperature. The junction transition temperature is $T_C = 6.5$ K, and the leads, which are narrowing when approaching the junction, have a critical temperature of $T_C^{\text{leads}} = 7.3$ K for the narrowest leads and 7.5 K for wider leads. The leads' critical current is over 500 μA at low temperature.

On the middle panel we see the current I as function of voltage V, taken at 1.2 K. The IV curve is non-hysteretic, characteristic of overdamped Josephson junctions (weak links with negligible capacitance). The normal resistance is $R_n \sim 1\,\Omega$, and the critical current $I_C \sim 7\,\mu$A, giving a Josephson coupling $I_C R_n \sim 7\,\mu$V, consistent with early studies on highly overdamped PdNi-based Josephson junctions. We have measured three ferromagnetic junctions on the same wafer (I4). The dispersion of the critical current from junction to junction

is about $\pm 1\,\mu$A, $\Delta R_n = 0.15\,\Omega$, while the $I_C R_n$ varies by less than 3% from junction to junction. The niobium oxide barrier, which has very low capacitance compared to aluminium oxide, serves to lower the junction critical current compared to the leads' critical current and avoid the mixup in the result interpretation.

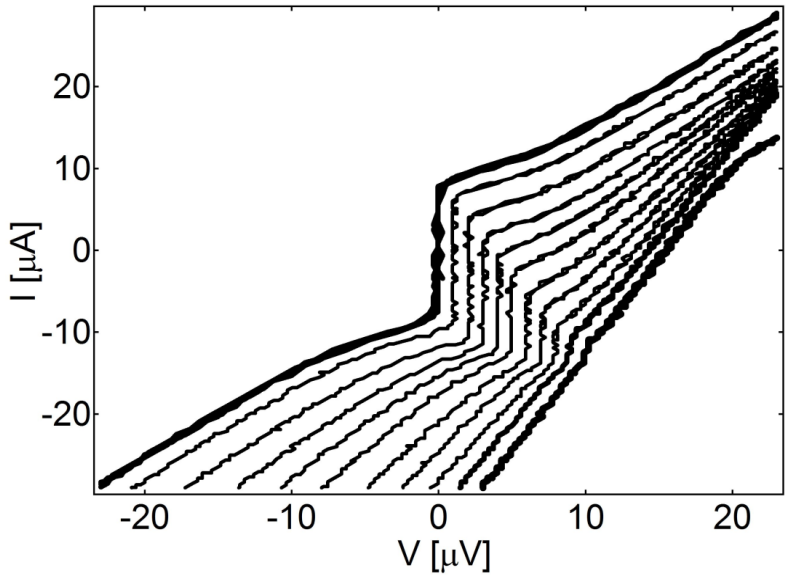

Figure 2.8: IV curves for temperature ranging from 1.2 to 6.2 K in steps of 0.5 K from left to right. The first curve on the left is given without an offset, and each subsequent curve is shifted for clarity to the left by 0.5 μV and down by 0.5 μA.

On the right panel we show the junction critical current as function of temperature, extrapolated to the junction critical temperature $T_C = 6.5$ K. The critical current $I_C(T)$ is obtained from the measurement presented in Fig. 2.8, showing the dependence of the IV curves on temperature, ranging from 1.2 K (first on the left) to 6.2 K in steps of 0.5 K. Linear dependence $I_C(T)$ is expected when the Thouless energy of the ferromagnetic layer $E_{Th} = \hbar D/a^2$ is larger than the Nb superconducting energy gap Δ. Here a is the thickness of the barrier, $D = v_F l_e/3$ is the diffusion coefficient of the ferromagnet, v_F its Fermi velocity and l_e the elastic mean free path. We estimate $l_e = 20$ nm, $v_F = 2 \times 10^7$ cm/s, $D = 13.3\,\mathrm{cm}^2/\mathrm{s}$, $\hbar D = 878\,\mathrm{meV\,nm}^2$ and $E_{Th} = 22$ meV for a junction of barrier thickness $a = 20$ nm[98]. The bulk Nb gap $\Delta = 1.5$ meV, therefore $E_{Th} \gg \Delta$. This linear dependence of $I_C(T)$ has

been observed previously in highly underdamped junctions[99].

2.2.3 Conductance/dynamical resistance measurement setup

Now we shall detail the setup for measuring the differential conductance $G = dI/dV(V_{dc})$, i.e. its inverse - the dynamical resistance $dV/dI(V_{dc})$, Fig. 2.9.

We measure the dynamical resistance with a lock-in amplifier. We bias the junction with dc current, and on top of it a small ac modulation current. The dc current is imposed with a voltage source, giving the voltage of the amplitude $V_b^{dc} \sim 80$ mV over a resistance of typically $R_b^{dc} \sim 1$ kΩ, making it a $I_b^{dc} = V_b^{dc}/R_b^{dc} \sim 80\,\mu A$ current ramp, with an extremely low frequency of 500 μHz. Since the junction is overdamped, with a normal resistance of typically 1 Ω, we typically sweep the dc voltage across the junction up to 80 μV, mounting from zero to this value for about half an hour. On top of the dc bias we impose a small ac bias, from a lock-in - $V_b^{ac} \sim 1$ V, $R_b^{ac} \sim 1$ MΩ, making it a $I_b^{ac} \sim 1\,\mu A$ excitation, corresponding to $1\,\mu V$ across the junction, at the frequency of $\nu = 177$ Hz.

The next step is the bias current measurement. We detect the current by measuring a voltage across a resistance of $R_i = 100\,\Omega$ in series with the sample, then amplifying it 100 times, and separating the dc from the ac part. We filter one line with a low band pass with a cutoff frequency of 3 kHz and detect I_{dc}, while the other line is not filtered and is detected with a lock-in as I_{ac}.

Similarly we detect the voltage across the junction. First we amplify the signal 100 times with a low noise preamplifier, then we separate it into two lines. The dc line gets amplified another 100 times, and filtered with a low band pass, and detected as V_{dc}. The ac line gets detected with a lock-in, in first harmonic as V_{ac}, and in second harmonic as $V_{ac}^{(2)}$.

The dynamical resistance is then $dV/dI = V_{ac}/I_{ac}$. We develop the junction response in a

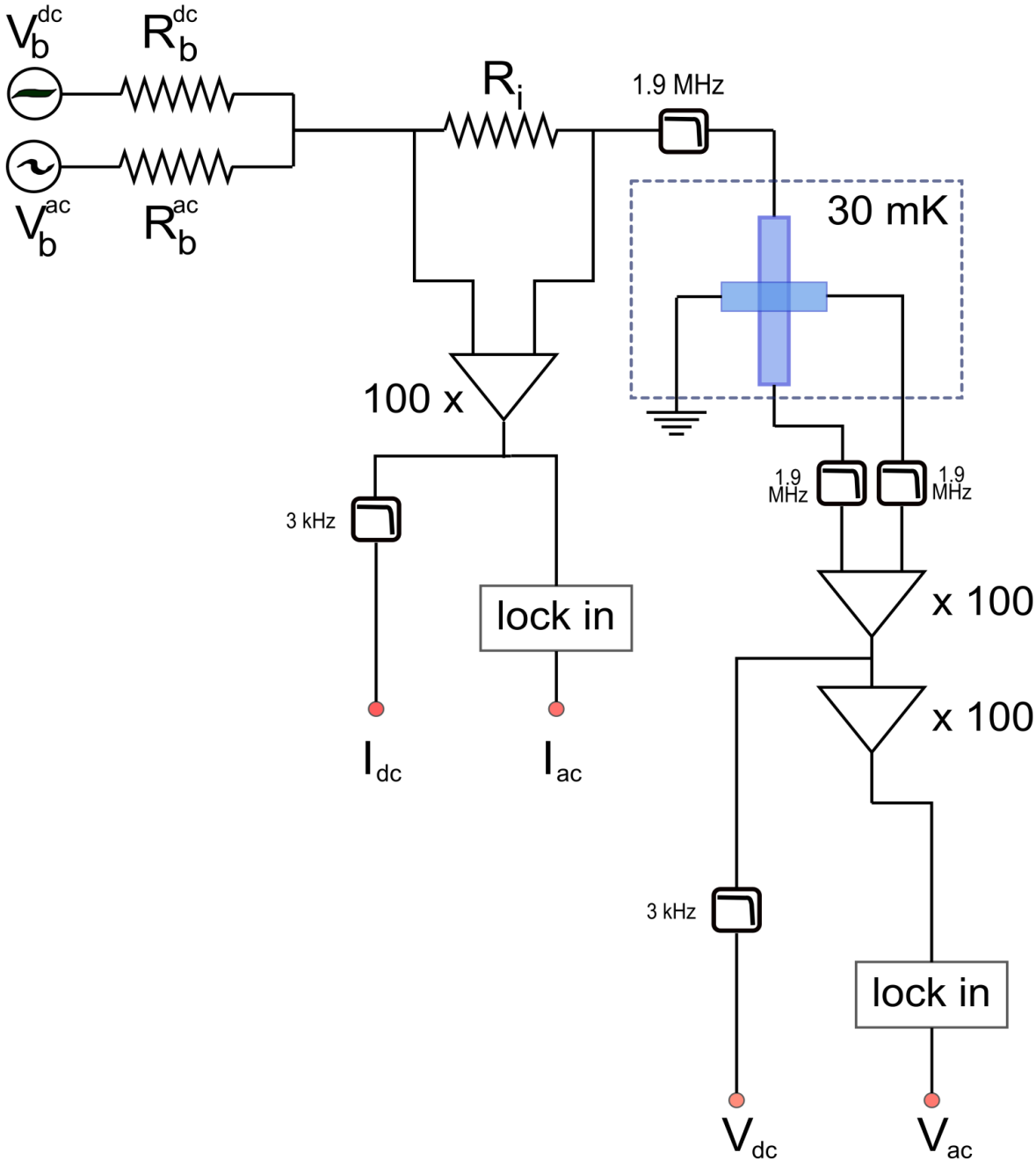

Figure 2.9: Conductance measurement setup.

Taylor series for $I_{ac} \ll I_{dc}$

$$V(I_{dc} + I_{ac}\sin(\omega_b t)) = V(I_{dc}) + \frac{dV}{dI} I_{ac}\sin(\omega_b t) + \frac{1}{2}\frac{d^2V}{dI^2} I_{ac}^2 \sin^2(\omega_b t) + ...$$

We measure the first term $V_{dc}(I_{dc})$ with dc voltmeters and it is the inverse of the IV

curve. The second term is detected with a lock-in, meaning the signal is multiplied with the reference at the frequency ω_b and averaged over many oscillation periods so the result $V_{ac} \sim (dV/dI)I_{ac}$. In the same way from the second term, by developing $\sin^2(\omega_b t) = (1 - \cos(2\omega_b t))/2$ and detecting the second harmonic, at $2\omega_b$, we get $V_{ac}^{(2)} \sim (d^2V/dI^2)I_{ac}^2$. In this way, in a single measurement we get the IV curve, the dynamical resistance and its derivative.

The incoming and outcoming lines are filtered with low band pass with a cutoff frequency of 1.9 MHz. Typically the dc bias current goes up to $100\,\mu$A, while the ac modulation voltage ranges between 0.5 and $2\,\mu$V. The amplifiers used are low noise preamplifiers NF Electronic Inst. LI-75A, and Stanford SR560 amplifiers, with variable cutoff filters. All of our filtering takes place at room temperature.

Some of our measurements are performed in a dilution refrigerator at 35 mK, and some others in a ^{4}He cryostat at 1.3 K.

The main challenge of this measurement is controlling the drift of the amplifiers. Since one sweep can take up to half an hour, during that time we can have $\sim 1\,\mu V$ of dc drift, so for the precise determination of frequency of resonances appearing in the dynamical resistance, we took special care to sweep many times, to make the sweeps symmetric around zero voltage, and sometimes to do faster sweeps only in the region we are interested in. Great care was taken to implement proper grounding and minimize the noise. We typically had $1\,\mu V$ of voltage noise.

Not shown in the schematic, we also often monitored the IV curve directly on the oscilloscope. For recording the data, we connected the instruments via GPIB ports and used a LabView program to read them. The temperature was measured by measuring the resistances of pre-calibrated resistors placed close to the sample.

In the 35 mK cryostat we put a commercial Hall probe on the sample holder in order to

measure the magnetic field close to the sample. The Hall probe's optimal working regime was for a current bias of 1 mA, rendering measurement impossible due to enormous heating, so we made tests to determine a stable regime with minimum bias current. We found the lowest possible value to be around 50 μA. The measurement was noisy but we were nevertheless able to measure the inductive delay of the superconducting coil used to impose the magnetic field, showing it to be not more than 30 Gauss when mounting up to 2000 Gauss over typically one hour.

2.3 Magnetostatic reference measurements on a macroscopic S/F/S trilayer

In order to investigate with a SQUID magnetometer the magnetic properties of thin ferromagnetic films embedded in the Josephson junctions, we have fabricated a macroscopic trilayer of the same cross-section as the junctions. Its surface is 6 mm × 8 mm and it consists of three layers: Nb (50 nm), $Pd_{0.9}Ni_{0.1}$ (20 nm) and Nb (50 nm), evaporated *in situ* under the same conditions as the junctions.

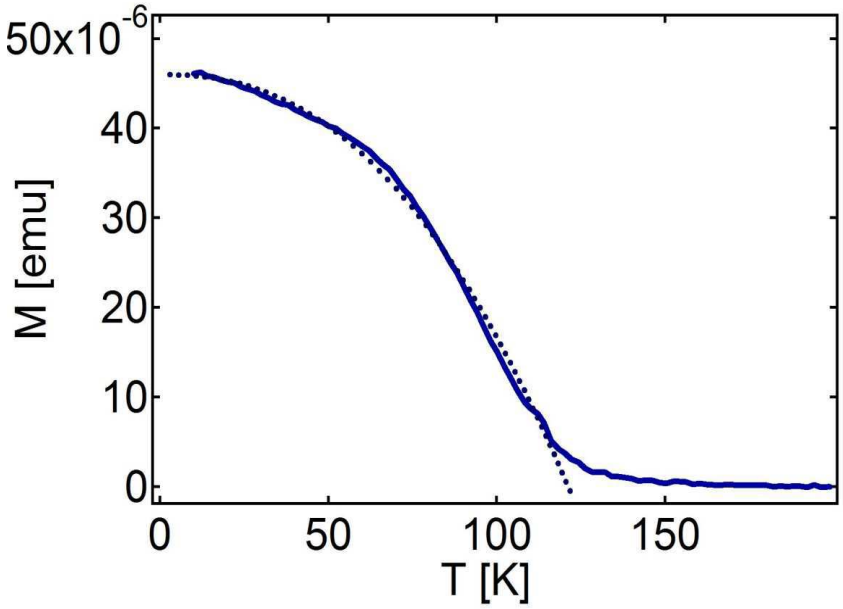

Figure 2.10: Magnetostatic measurement performed with a SQUID magnetometer on a 6 mm × 8 mm trilayer of Nb(50 nm)/ $Pd_{0.9}Ni_{0.1}$(20 nm)/ Nb(50 nm) (same cross-section as the junction) with the applied in plane field of 2000 G. Fitting parameters to the Bloch-like law $M = M_0(1 - (T/T_{\text{Curie}})^{\gamma})$ are the saturation magnetic moment $M_0 = 45.9 * 10^{-6}$ emu (corresponding to 600.5 Gauss), the Curie temperature $T_{\text{Curie}} = 120.6$ K and the obtained exponent is $\gamma = 2.38$.

First we measure the magnetic moment as function of temperature with the applied in plane field of 2000 G, Fig. 2.10. We fit $M(T) = M_0(1 - (T/T_{\text{Curie}})^{\gamma})$, where M_0 is the saturation magnetic moment, T_C is the Curie temperature and γ is the exponent. We find

$M_0 = 45.9 * 10^{-6}$ emu (corresponding to 600.5 Gauss - note that at $H = 2000$ G we are not at saturation), $T_C = 120.6$ K and $\gamma = 2.38$. The Curie temperature value is in accord with the previous measurements on 10% Ni thin films[98]. The exponent is somewhat larger than 3/2 in the Bloch $T^{3/2}$ law, valid for a monodomain.

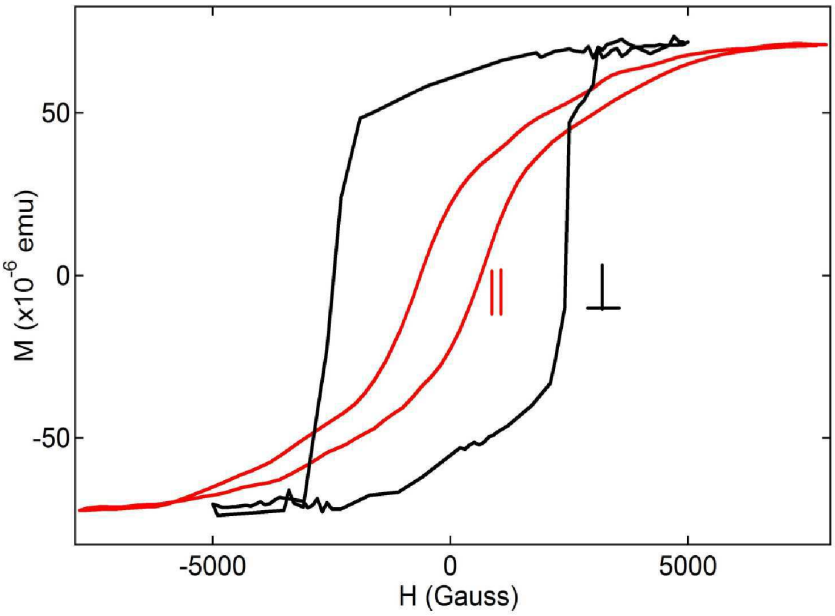

Figure 2.11: Magnetization as function of the external field measured on a 6 mm × 8 mm trilayer of Nb(50 nm)/ $Pd_{0.9}Ni_{0.1}$(20 nm)/ Nb(50 nm) (same cross-section as the junction) at 10 K. The red curve is measured with field in plane and the black curve with perpendicular field. The saturation magnetization of $71 * 10^{-6}$ emu corresponds to 929 Gauss.

Then we measured the magnetization curves M(H) at 10 K in parallel (red curve) and perpendicular (black curve) field, Fig. 2.11. The saturation magnetization is $M_S = 71 * 10^{-6}$ emu, corresponding to 929 Gauss. We see that the hysteretic cycle is rectangular in the perpendicular field and very narrow in the parallel field, showing that the magnetization has a dominant component perpendicular to the layer surface. From this measurement we can also estimate the magnetic anisotropy $H_K \sim 5000$ Gauss.

2.4 Static influence of magnetization on the critical current

In analogy to the diffraction of light through a rectangular slit, the phase difference across the Josephson junction in the external magnetic field gets different path-dependent contributions, leading to the interference of the phase-dependent current. The critical current as function of the applied field shows the Fraunhofer pattern. Later we extend the Fraunhofer picture to describe the influence of the time-dependent magnetization $\mathbf{M}(t)$ on the Josephson current, but in this Section we shall consider only the static effect.

The static contribution of magnetization $\mathbf{M}$ to the Josephson phase is via the vector potential $\mathbf{A}$

$$\varphi = \varphi_0 + \frac{2e}{\hbar} \int \mathbf{A} \cdot d\mathbf{l},$$

where φ_0 is the Josephson phase without the magnetic field, and $\mathbf{l}$ the phase path. The current density is

$$\mathbf{j}(x, y) = j_C(x, y) \sin(\varphi_0 + kx)\, \hat{\mathbf{z}},$$

where j_C is the critical current density, and the all-important field dependence is contained in the wave vector

$$k = \frac{2ed\mu_0}{\hbar} \left(H + \frac{a}{d} M \right), \tag{2.1}$$

for $\mathbf{H}$ and $\mathbf{M}$ in the y direction, z being perpendicular to the junction surface, Figs. 1.5 and 2.6. The ferromagnetic barrier thickness is a, while d is the magnetic barrier thickness. When d_S, the thickness of the superconducting layer, is much larger than the penetration depth λ, then $d = a + 2\lambda$. When $d_S \sim \lambda$, as is the case in the experiment, the effective

magnetic thickness is $d = 2\lambda \tanh(d_S/2\lambda) + a$[96]. Integrating the current density along the field direction coordinate for the junction length L, we have

$$J(x) = \int_{-L/2}^{L/2} j(x,y)dy.$$

Critical current $I_C(k)$, with the field dependence contained in k, is then

$$I_C(k) = \left| \int_{-L/2}^{L/2} dx J(x) \exp(\imath k x) \right|. \tag{2.2}$$

For a uniform current distribution $J(x) = J_0$, we would obtain the Fraunhofer pattern, with its maximum shifted due to magnetization. Maximum current is achieved for $H + (a/d)M(H) = 0$. This equation in H has two solutions that differ only in sign. When we sweep the field in two different directions, due to the hysteresis of the ferromagnetic layer, we see the current maximum shifted in two directions, corresponding to the positive and negative solution, see Fig. 2.12. This is the central result of this Section.

We have measured the Fraunhofer pattern using the counter. We bias the junction with current in the form of a sawtooth ramp of frequency $\nu_b = 117$ Hz and amplitude of $V_b = 90$ mV across $R_b = 10$ kΩ, making it a $I_b = V_b/R_b = 9\,\mu$A ramp, with the critical current of the junction $I_C = 6.7\,\mu$A. We trigger at finite voltage of $2\,\mu$V. The voltage is amplified 2×10^5 times. The counter measures the time between the start of the ramp and the triggering event, which is proportional to the critical current. We ramp the field with a symmetrical ramp from -2000 to 2000 Gauss, with the speed of 0.4 Gauss/s. In this way it takes 5.5 hours to do one full sweep and we accumulate traces over 72 hours, and average them to obtain the curves presented in Fig. 2.12 in red. The absolute current error is 50 nA. The two branches corresponding to the two sweep directions are normalized to their own maximum values. The critical current for the mounting field branch is $I_C = 6.7\,\mu$A, while for the descending field branch it is slightly different, $I_C = 6.2\,\mu$A. This measurement is taken in the dilution

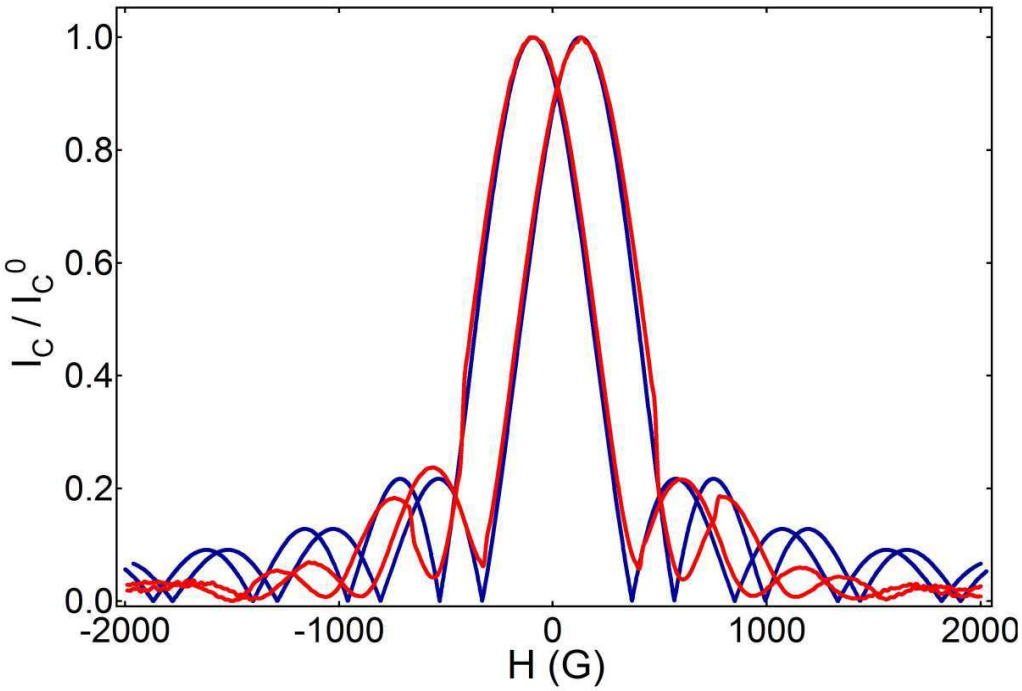

Figure 2.12: Fraunhofer pattern for two in plane field sweep directions showing the magnetic hysteresis of the ferromagnetic barrier. Red curve: experimental data, blue curve: fit supposing the magnetization $M(H)$ shown in Fig. 2.13 (blue full curves) and the current distribution $J(x)$ shown in Fig. 2.14. Critical currents for two sweep directions are normalized to their own maximum values. Temperature is $T = 35$ mK.

refrigerator at the temperature of 35 mK, with the temperature possibly varying between 35 and 50 mK, which does not affect the IV curve. The drawing of the measurement setup is given in the following Chapter, Fig. 3.5.

In Fig. 2.12 we have shown a shift in the Fraunhofer pattern corresponding to the contribution of the ferromagnetic layer to the overall field inside the Josephson junction. We see this shift to be around 150 Gauss in each direction, corresponding to the hysteresis width measured on a macroscopic trilayer of the same material (Fig. 2.13), when bearing in mind that the magnetization enters with a prefactor $a/d \sim 1/4$. This is the reflection of the fact that the external magnetic field penetrates into the superconductor, while the magnetization only plays a significant role in the ferromagnetic layer itself. The superconducting coil used to impose the external in plane field has an inductive delay, but with independent Hall probe

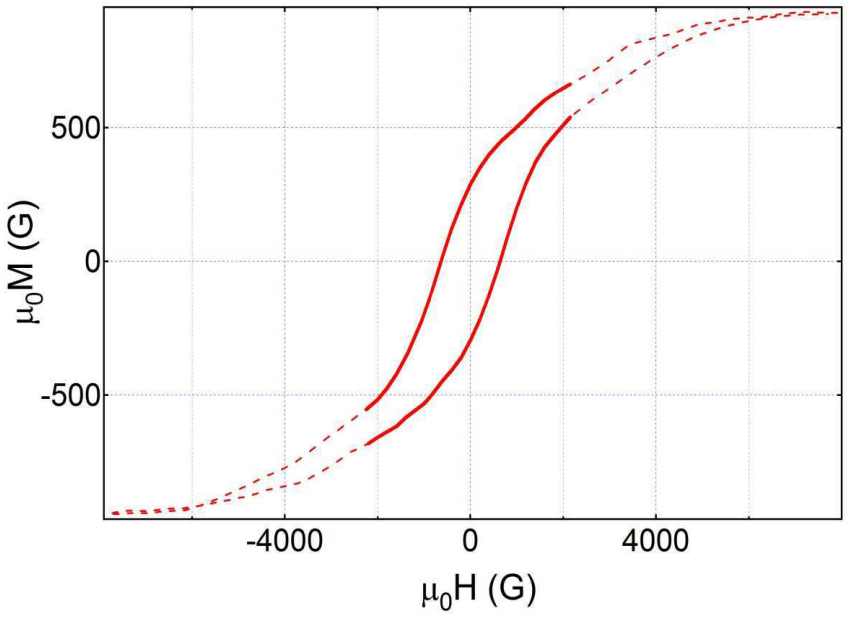

Figure 2.13: Hysteretic curve M(H) of the reference trilayer. Magnetostatic measurement is performed in a dc SQUID on a 6 mm × 8 mm trilayer of Nb(50 nm)/ $Pd_{0.9}Ni_{0.1}$(20 nm)/ Nb(50 nm) (same cross-section as the junction) at 10 K with field in plane. The solid curves between -2000 G and 2000 G were used for fitting the Fraunhofer curve, and the fit is given in blue in Fig. 2.12.

measurements we show it does not exceed 30 Gauss for this ramp speed and amplitude.

As we can see from Eq. (2.1), we can fit the $I_C(H)$ by taking into account $M(H)$ measured independently on a macroscopic trilayer, Fig. 2.13. The dotted curve is $M(H)$ taken when sweeping the field to saturation, while the full curves are the part of the hysteretic cycle between -2000 and 2000 G, corresponding to the sweep in the $I_C(H)$ experiment. The agreement between the fit and the measured $I_C(H)$ is good, and we reproduce the shift in $I_C(H = \pm(a/d)M)$. Although we expect the hysteretic loop of the trilayer when sweeping only up to 2000 G to be smaller, on the other hand, we expect the hysteretic loop inside the junction to be wider than the one on the trilayer, t.i. a higher coercive field.

Since the second maxima in the measured Fraunhofer pattern are lower than expected for a uniform current distribution, we should have a current distribution $J(x)$ that is slightly

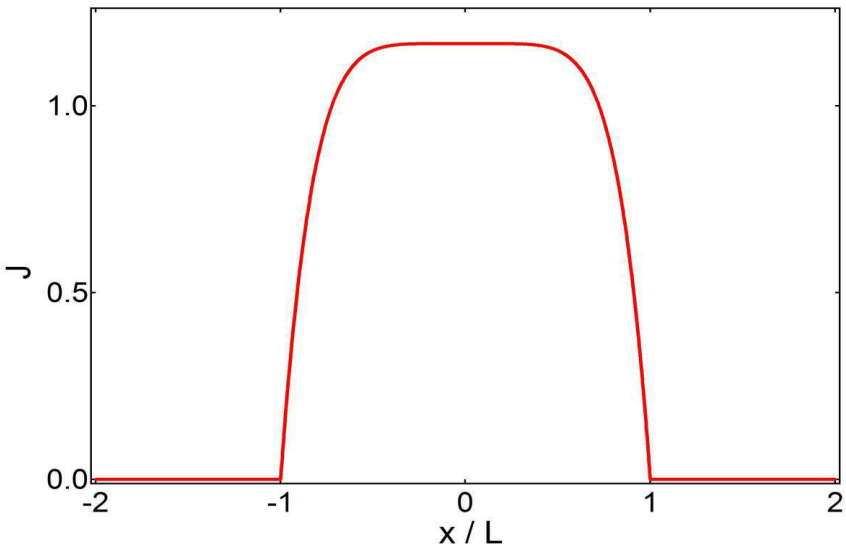

Figure 2.14: Current distribution across the junction in the direction perpendicular to the applied in plane field. The current distribution is used for the fit of the Fraunhofer pattern, Fig. 2.12.

rounded in the middle of the junction[96]. We fit the data $I_C(H)$ supposing the distribution

$$J(x) = J_0 \left[1 - \left(\frac{2x}{L} \right)^6 \right], \tag{2.3}$$

where L is the junction's lateral size, Fig. 2.14.

The known constants are the ferromagnetic barrier thickness $a = 20$ nm and the superconducting layer thickness $d_S = 50$ nm. The fitting parameter is the product $d * L$, obtained from the $I_C(H)$ periodicity, where d is the magnetic barrier thickness. We get $d * L = 36.2\,\mu\text{m} \cdot \text{nm}$. We do not have the exact value of λ, the penetration depth, but we know that $d(\lambda) = 2\lambda \tanh(d_S/2\lambda) + a$ is a very slowly varying function in the range we are interested in, for $\lambda \sim 50$. We know that $\lambda > \lambda_{bulkNb} = 40$ nm, since it is a thin film of a critical temperature lower than bulk. When assuming $\lambda = 50$ nm we obtain $d = 66.2$ nm, yielding $L = 0.54\,\mu$m, which is quite reasonable, since the measured length of a similar junction fabricated in the same way was $0.5\,\mu$m.

In Fig. 2.15 we show the IV curves taken at 35 mK for different field values. This measure-

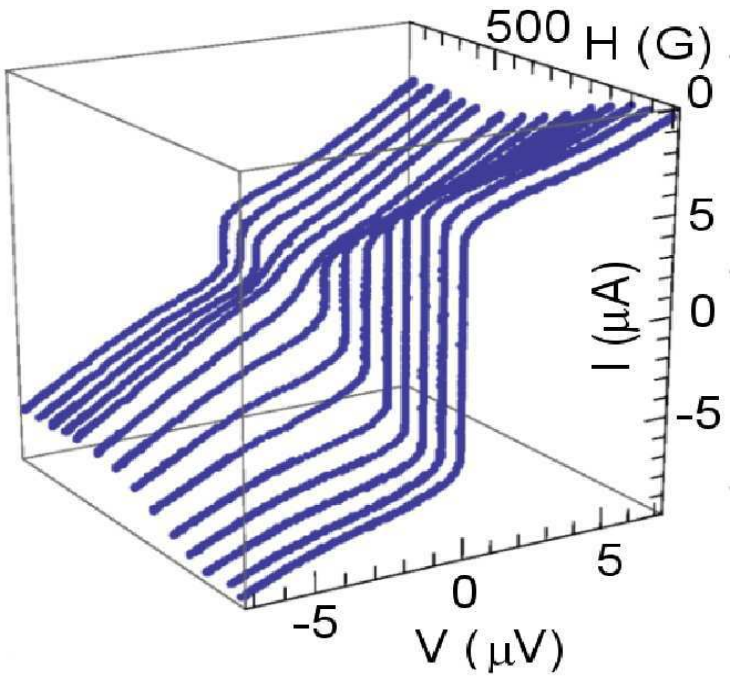

Figure 2.15: Current-voltage characteristics taken at 35 mK for different values of the in plane external magnetic field.

ment is taken separately with an oscilloscope. Since this measurement was taken for field between -800 G and 800 G (only one sign of field is shown), the corresponding shift in the maximum critical current is less than in Fig. 2.12, when we swept up to 2000 G.

A very important aspect of the $I_C(H)$ measurement is the demonstration of the time reversal invariance, proving that the shift in the Fraunhofer pattern is of magnetic origin. As expected, $t \to -t$ is equivalent to $H \to -H$ and $M \to -M$. This can be best seen if we notice a small step in $I_C(H)$ around 760 G, corresponding probably to a domain switching, and it is also found on the curve for the other sweep direction, at -760 G.

However, the time reversal symmetry is not entirely preserved with regard to the absolute value of maximum I_C: the maxima $I_C^{\text{up}} = 6.7\,\mu\text{A}$ and $I_C^{\text{down}} = 6.2\,\mu\text{A}$ for two sweep directions are not equal. We can attribute this asymmetry either possibly to the domain structure, where the domains are slightly differently pinned for two sweep directions, or to a small voltage drift in the triggering value.

2.5 Coupling between the spin waves and the Josephson current

In the previous Section, we saw the static influence of magnetization of the ferromagnetic layer inside the Josephson junction on the critical current I_C. In a non-magnetic junction, the $I_C(H)$ shows a Fraunhofer pattern, analogous to the intensity of light through a rectangular slit as function of position on the screen, with a maximum at $H = 0$. Adding a ferromagnetic layer inside the junction is analogous to adding a wedge-plate in front of the rectangular slit - it shifts the Fraunhofer pattern maximum from $H = 0$ to $H^{\pm} = \pm(a/d)M$, depending on the sweep direction. Now let us imagine that the magnetization is time dependent, corresponding to spin wave modes, domain wall movement etc. We can extend the Fraunhofer analogy to consider how this affects the current, $\langle I_C(t)\rangle$. Basically, we are moving along the Fraunhofer pattern. The Josephson junction offers an additional possibility - resonant coupling between the magnetic modes and the Josephson current, when the Josephson frequency $\omega_J = (2e/\hbar)V_J$ at imposed voltage V_J matches the magnetic mode's frequency ω_s. The characteristic frequencies are in the GHz range, accessible for measurement in our overdamped Josephson junctions, since there is no hysteretic jump in the IV curve. Therefore, by measuring the IV curve or its derivatives, we expect to see resonances as dips at the spin wave frequencies.

In this Section we present the measurements of the dynamical resistance of ferromagnetic Josephson junctions, showing these resonant modes. By subsequent investigation of their behavior in the external magnetic field and their coupling with the Shapiro resonances, we confirm that they are of ferromagnetic origin and coupled to the supercurrent.

2.5.1 Resonant dips in the dynamical resistance

For an overdamped Josephson junction, the phase is entirely determined by a voltage across the junction, and it is well described within the RSJ model, modeling a Josephson junction as an ideal Josephson element in parallel only with an Ohmic resistance, since the capacitance is negligible. Then, the current across the junction is a function of voltage,

$$I(V) = \sqrt{{I_C}^2 + \left(\frac{V}{R}\right)^2},$$

where I_C is the critical current, and R is the Ohmic resistance. We can develop this expression in V and keep only the first term

$$I(V) = \frac{V}{R} + \frac{I_C^2\, R}{2V}. \tag{2.4}$$

By introducing the Landau-Lifshitz equation which describes the magnetization dynamics into the Josephson effect, we see the coupling between the two is contained in the additional term

$$I = \frac{V}{R} + \frac{{I_C}^2(B_0)}{2V} R - 2\pi I_C(0) \frac{\Phi_{\rm rf}}{\Phi_0} \left[F_x \chi_x''(\omega_J) + F_y \chi_y''(\omega_J) \right], \tag{2.5}$$

where Φ_0 is the flux quantum, $\Phi_{\rm rf} = (2aL)B_{\rm rf} = (2aL)\mu_0 I_C(0)/L$ is the flux due to the radio frequency field, while $F_x = (1/12)(I_C(B_0)/I_C)^2$ and $F_y = (2/x^2)[1 + \sin(x/2)\cos(x/2) + ((13/12) - (4/x^2))\sin^2(x/2)]$; $x = kL$, reflect the geometrical structure of the coupling. The junction surface is $L \times L$, and $B_0 = \langle B(t) \rangle$ is the static part of B. The magnetic resonance signal is contained in $\chi_x''(\omega_J)$ and $\chi_y''(\omega_J)$, which correspond to the Fourier transform of the imaginary part of susceptibility $\chi_i(t)$, $i = x, y$. Note that $F_x(B_0)$ is proportional to the Fraunhofer function $I_C(B_0)$. This is the basis of the Fraunhofer description of the effect.

We measure the dynamical resistance

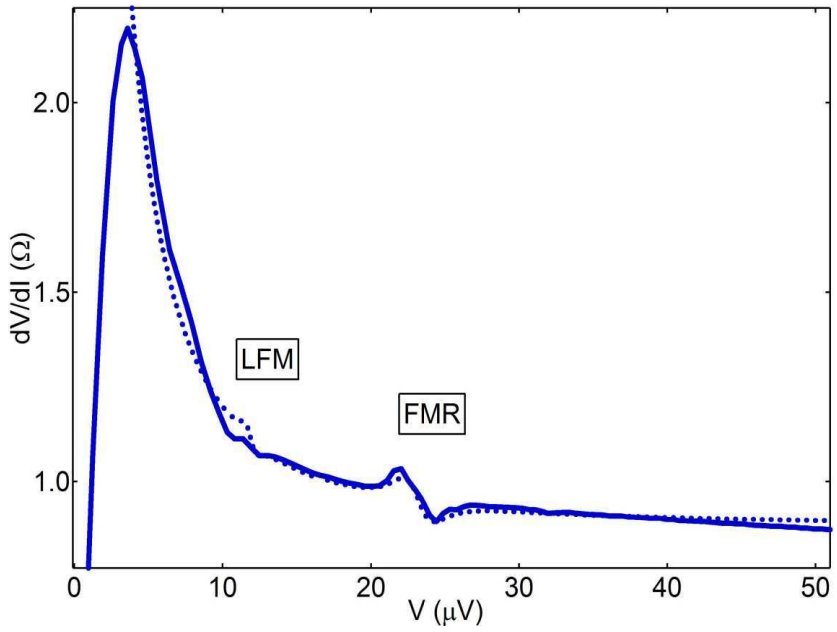

Figure 2.16: Dynamical resistance of the ferromagnetic Josephson junction. We see the resonances at $10\,\mu$V (Low Frequency Mode - LFM) and at $23.2\,\mu$V (Ferromagnetic Mode - FMR). The full curve is the experimental data, while the dotted curve is a fit using Eqs. (2.7) and (2.6) with the parameters given in the text. This curve is measured with the ac modulation voltage of $1\,\mu$V, at 35 mK.

$$R(V) = \left(\frac{dI(V)}{dV}\right)^{-1} = \frac{dV}{dI}, \tag{2.6}$$

shown in Fig. 2.16 as the full curve. We see two resonances, one at $10\,\mu$V, which we call a Low Frequency Mode (LFM), and another at $23\,\mu$V, a Ferromagnetic Resonance (FMR). The fit is also shown as the dotted curve, using Eq. (2.6) and the following simplification of Eq. (2.5)

$$I(V) = \frac{V}{R} + \frac{{I_C}^2}{2V}R - {I_C}^2\frac{A\,\sigma}{\sigma^2 + (V - V_s)^2}, \tag{2.7}$$

where A is the resonance amplitude, $V_s = (2e/\hbar)\omega_s$ is the voltage corresponding to the resonant frequency ω_s and σ is the resonance width (also in voltage units). The measurement is taken at zero external field. We have used the usual form for the imaginary part of the

magnetic susceptibility

$$\chi''_{x,y}(V) \approx \gamma_e M_z \left[\frac{\sigma}{(V - V_s)^2 + \sigma^2} \right], \tag{2.8}$$

so $A = 4\pi\mu_0 a \gamma_e M_z F_x$ ($F_x = F_y$ at zero field).

We measure the dynamical resistance with a lock-in amplifier. The setup is detailed in 2.2.3. We bias the junction with dc current with a small ac component, and use the lock-in amplifier to measure the ac voltage across the junction. Typically the dc bias current goes up to 100 μA, while the ac modulation voltage ranges between 0.5 and 2 μV. Some of our measurements are performed in a dilution refrigerator at 35 mK, and some others in a ^{4}He cryostat at 1.3 K.

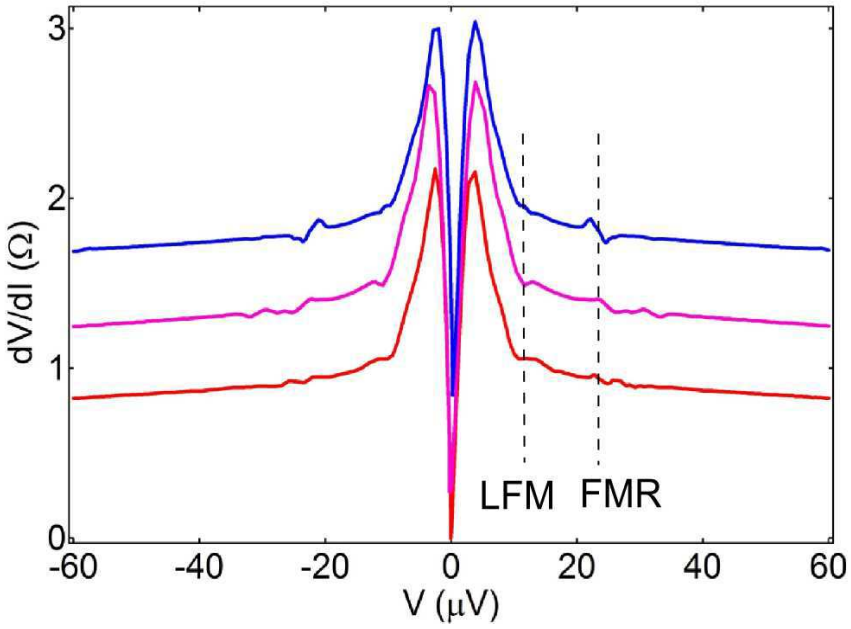

Figure 2.17: Dynamical resistance of the three ferromagnetic Josephson junctions fabricated on the same wafer, taken at 1.3 K. Curves are shifted for clarity. The vertical dotted lines denote the Low Frequency Mode (LFM) and the Ferromagnetic Resonance (FMR).

We fit the dynamical resistance of the ferromagnetic Josephson junction using Eqs. (2.6) and (2.7). We obtain $I_C = 10.3 \pm 0.2\,\mu$A and $R = 0.88\,\Omega$; for LFM : $V_s = 11.88\,\mu$V,

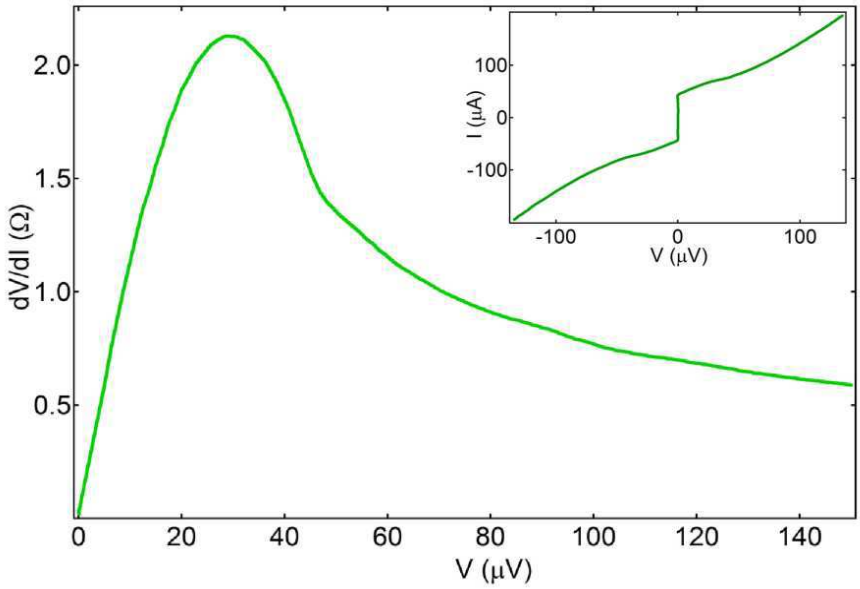

Figure 2.18: Dynamical resistance of the non-ferromagnetic Josephson junction, taken at 2 K. **Inset**: IV curve taken at the same time.

$A = 2\times10^{-4}\,\Omega^{-1}$ and $\sigma = 0.7\,\mu$V; for FMR : $V_s = 23.2\pm0.2\,\mu$V, $A = (2.5\pm1)\times10^{-3}\,\Omega^{-1}$, and $\sigma = 1.7\pm0.5\,\mu$V. The fitting parameters A and σ contain the smearing with ac modulation voltage. We shall discuss the actual resonance width and amplitude shortly. Note that the background fit is not able to reproduce the correct critical current value, due to excess current at voltage close to zero which is a deviation from the RSJ model, Eq. (2.4). Directly measured value of I_C is 6.7 μA.

We have obtained the same ferromagnetic resonances for three different junctions fabricated on the same wafer, measured in the ^{4}He refrigerator at 1.3 K, Fig. 2.17. For all junctions we see the LFM at approximately 10 μV, and the FMR at 23 - 25 μV. We have repeated the measurement in the dilution refrigerator at 35 mK, obtaining the same results.

When considering the resonance width, it is important to take into account the influence of the modulation ac voltage, which smears out the resonance. We have typically used the modulation voltages between 0.5 and 2 μV. Results of measurements presented in this Chapter are mostly taken with an ac modulation voltage of 1 μV. The resonance width is

also typically around $1\,\mu$V, so the details are only visible with a smaller ac modulation voltage. We shall study the resonance width in more detail in the Chapter 2.7, dedicated to the comparison between the signal taken via the Josephson effect and in a conventional cavity FMR experiment. The value of A for the FMR mode taken at $0.5\,\mu$V modulation voltage corresponds to $\chi'' \sim 10$, which is consistent with conventional FMR measurements on the similar film. For ac modulation voltage below 0.5 μV, the measurement becomes more difficult, due to the voltage noise of the order of 0.2 μV.

We also fabricated junctions with a stronger ferromagnet, a 11 nm thick $Pd_{0.5}Ni_{0.5}$ layer, with 50% of Ni. We were only able to investigate the dc bias up to $20\,\mu$V (corresponding to frequencies up to 10 GHz), since the junction leads switched into the normal state at higher bias. We did not see any resonances in that range.

Next we compared the dynamical resistance of a ferromagnetic Josephson junction with that of a non-ferromagnetic one. We have fabricated the junction in the same way, but this time instead of the layer of 20 nm of $Pd_{0.9}Ni_{0.1}$, we have evaporated 70 nm of non-ferromagnetic Pd, see Fig. 2.18. The critical current is $I_C = 40\,\mu$A, and the normal resistance $R_N = 0.7\ \Omega$. The dynamical resistance of this junction does not show any resonances. This is confirmed by the second derivative measurement. We have investigated the dc voltage range up to $150\,\mu$V. At higher bias the junction leads switch to the normal state.

2.5.2 Shapiro step sideband resonances

The next step is to confirm that the ferromagnetic resonant modes couple to the Josephson rather than to the normal current. We do that by irradiating the Josephson junction with microwaves. The IV curve then displays constant-voltage steps, which can be viewed as replicas of the Josephson current[27]. We expect side-band resonances corresponding to the ferromagnetic modes.

The simplest way to model Shapiro steps is to consider the microwaves as an addition to the voltage bias

$$V(t) = V_J + v\cos\Omega t,$$

where v and Ω are the amplitude and frequency of the applied microwave field, and V_J is the dc voltage bias, corresponding to the Josephson frequency $\omega_J = (2e/\hbar)V_J$. The phase is then

$$\varphi = \frac{2e}{\hbar}\int V(t)\,dt = \varphi_0 + \omega_J t + \frac{2ev}{\hbar\Omega}\sin\Omega t,$$

where φ_0 is an arbitrary integration constant. The corresponding Josephson current is

$$I = I_C\sin\varphi = I_C\sin\left(\varphi_0 + \omega_J t + \frac{2ev}{\hbar\Omega}\sin\Omega t\right).$$

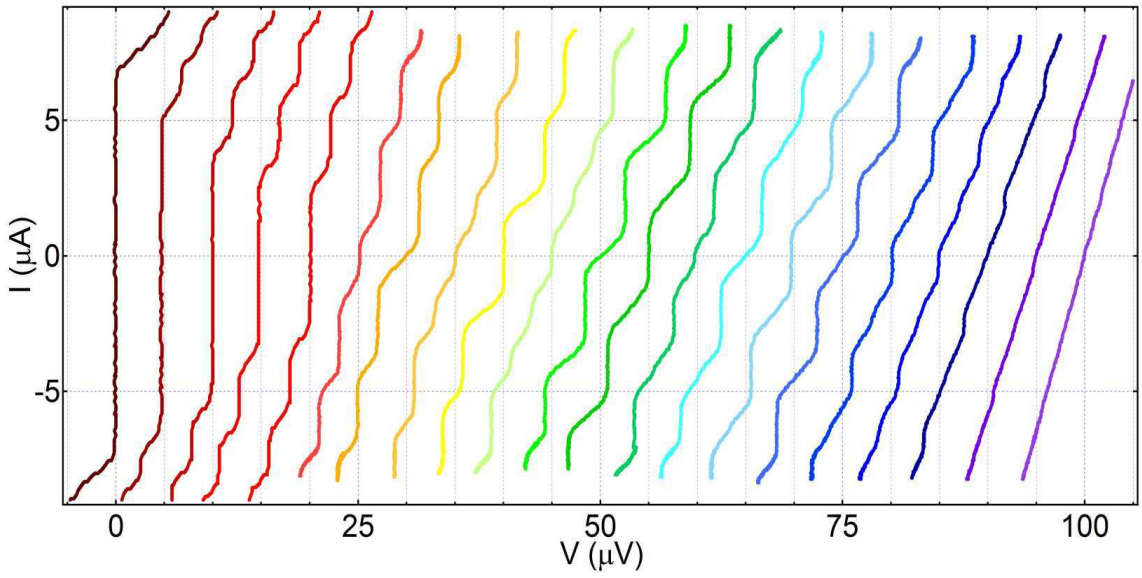

Figure 2.19: The IV curves taken at 1.3 K in the ^{4}He with external microwave irradiation at $\nu_{\mathrm{rf}} = 1$ GHz and with power varying between -50 dBm (left) up to 10 dBm (right) at the top of the cryostat. The first curve on the left (dark red) is given without shift, and each subsequent n-th curve is shifted horizontally for $n \times 5\,\mu$V to the right.

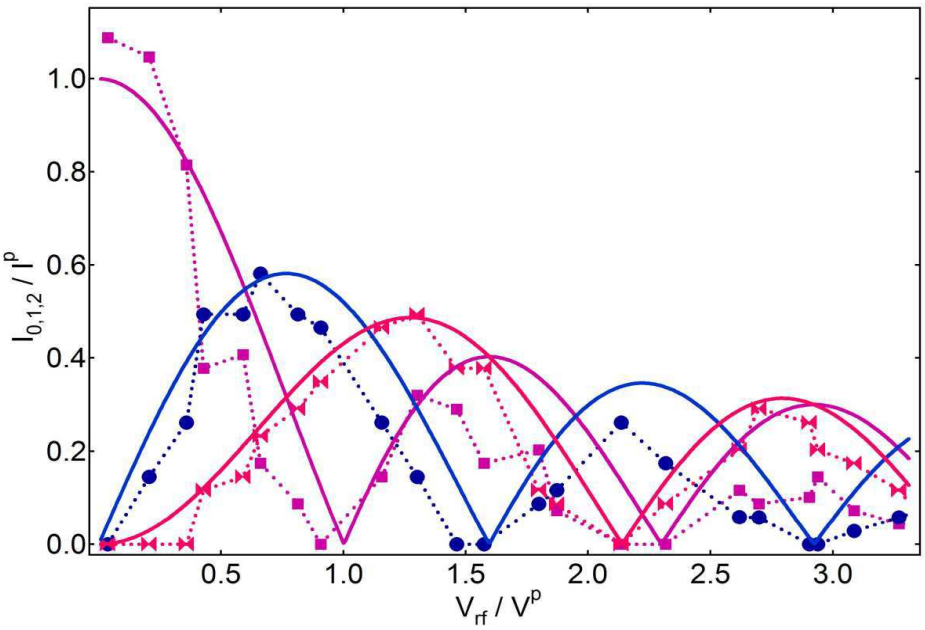

Figure 2.20: The IV curves taken at 38 mK with external microwave irradiation at $\nu_{\rm rf} = 8$ GHz. Markers connected by dotted curves are measured data and full curves are Bessel functions of the corresponding order, indicated by color (step 0 - purple, step 1 - blue and step 2 - pink). The normalization constants, obtained as the fitting parameters, are $I^p = 5.5\,\mu$A, and $V^p = 58.7$ mV (these values refer to power at the top of the cryostat).

As is well known, this expression can be expanded in terms of $\sin[(\omega_J - n\Omega)t]$ for integer n, giving a dc contribution for $\omega_J = n\Omega$, corresponding to voltage $V_n = n(\hbar/2e)\Omega$, with an amplitude $I_n = I_C J_n$, proportional to a first-order Bessel function $J_n(2ev/\hbar\Omega)$, where I_C is the critical current of the non-irradiated junction. For the magnetic modes, the coupling with the Josephson current is reproduced at each step, so Eq. (2.7) is valid in the form

$$I(V) = \sqrt{{I_n}^2 + \left(\frac{V_n}{R} - \frac{A\,\sigma {I_n}^2}{\sigma^2 + (V_n - V_s)^2}\right)^2}. \tag{2.9}$$

We expect the side-band resonances in the vicinity of each step, at $V_n \pm V_s = (2e/\hbar)(n\Omega \pm \omega_s)$.

The setup is the same as previously. We measure the dynamical resistance with lock-in detection. The microwaves are guided to the bottom of the dilution refrigerator with a coaxial cable, ending with an antenna.

First we will focus on the Shapiro steps themselves in order to verify their expected power dependence. In Fig. 2.19 we see the IV curves taken for different power of microwave radiation at $\nu_{\rm rf} = \Omega/2\pi = 1$ GHz. Power is varying between -50 dBm (left) and 10 dBm (right) at the top of the cryostat. The curves are shifted for clarity: the first curve on the left (dark red) is given without shift, and each subsequent n-th curve is shifted $n \times 5\,\mu$V to the right.

Next we measure the dependence of the current steps upon the voltage determined by the microwave power, $I_n(v)$, expecting it to be proportional to the first order Bessel functions $J_n(2ev/\hbar\Omega)$. This measurement is taken in the dilution refrigerator, which ensured better coupling with the external microwaves over a wide range of frequencies, and is presented in Fig. 2.20. The normalization constants, obtained as the fitting parameters, are $I^P = 5.5\,\mu$A, and $V^P = 58.7$ mV. I^P is the junction's critical current in this measurement, and V^P is the ac voltage corresponding to the irradiated microwaves at the top of the cryostat. We see that our Shapiro step values correspond rather well to the Bessel functions, obtained assuming unform current distribution.

However, the magnetic modes are too small an effect to be visible in the IV measurement, so we shall measure the dynamical resistance dV/dI.

In order to demonstrate that the ferromagnetic modes couple to the Josephson current, and not to the normal current, we irradiated the ferromagnetic Josephson junctions with external microwaves at the frequencies higher than the low frequency mode (LFM) at $V_{\rm LFM}$ =10 μV ($\nu_{\rm LFM} = \omega_{\rm LFM}/2\pi$ =5 GHz), expecting side-band resonances at frequencies $\omega_J = \Omega \pm \omega_{\rm LFM}$. We measured the dynamical resistance in two cryostats, first in the ^{4}He cryostat at 1.3 K and with the external microwave frequency $\nu_{\rm rf} = 7.7$ GHz, and second in the dilution refrigerator at 40 mK and external microwave frequency $\nu_{\rm rf} = 17$ GHz (see Fig. 2.21). In both cases we see the sideband resonances as the $10\,\mu$V mode. The maximum external frequency we were able to apply was 20 GHz, leaving the investigation of the coupling of the ferromagnetic

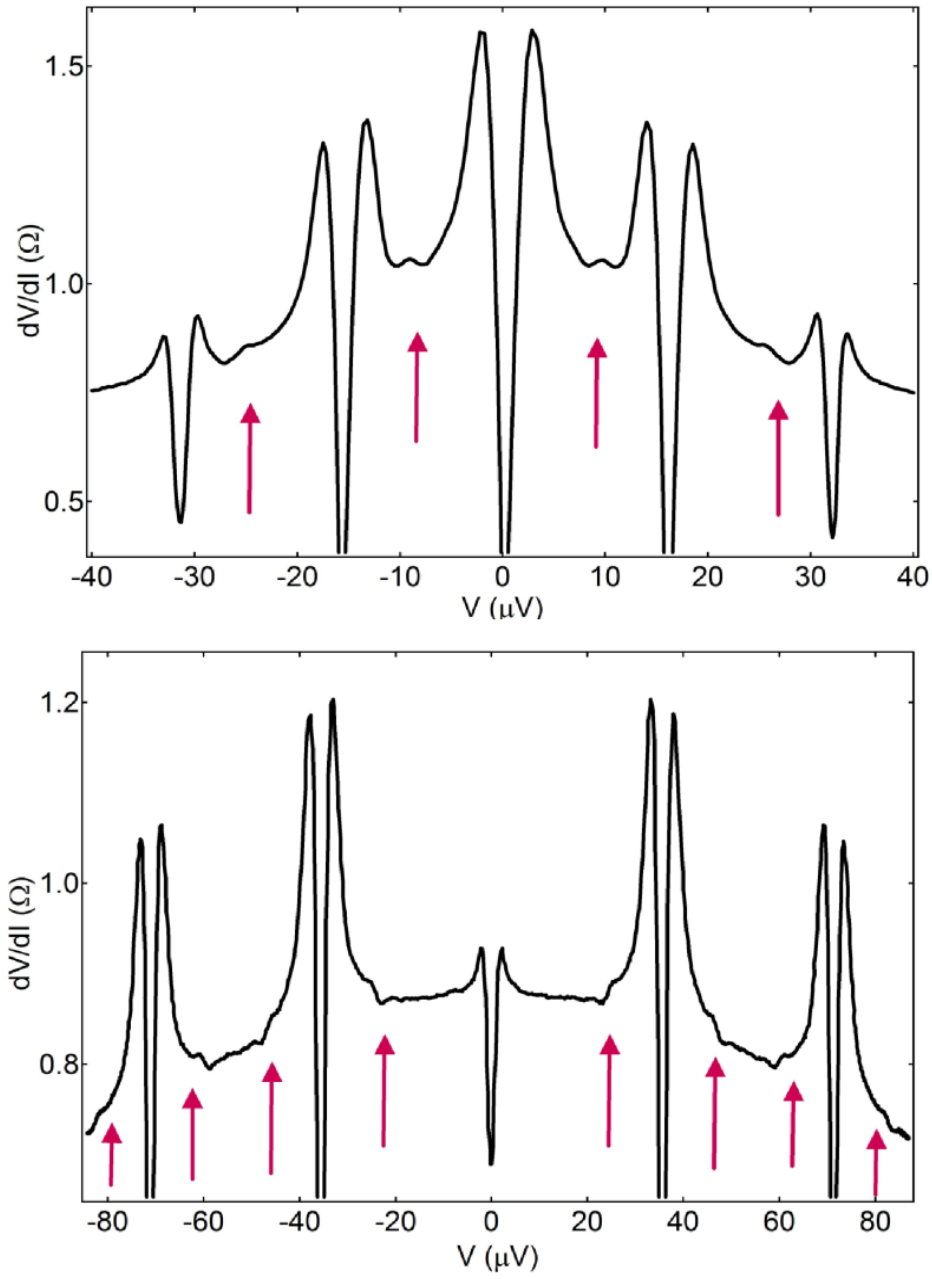

Figure 2.21: Dynamical resistance taken at temperature T=1.3 K with microwave frequency $\nu_{\rm rf} = 7.7$ GHz on the top panel and at T=40 mK and frequency $\nu_{\rm rf} = 17$ GHz on the bottom panel. The large dips correspond to the Shapiro resonances. The sideband resonances of the Low Frequency Mode (LFM) are indicated by arrows.

mode (FMR) at 23 μV to the Josephson current out of range.

As shown previously, the amplitude of the resonances scales with the critical current ${I_C}^2$. By

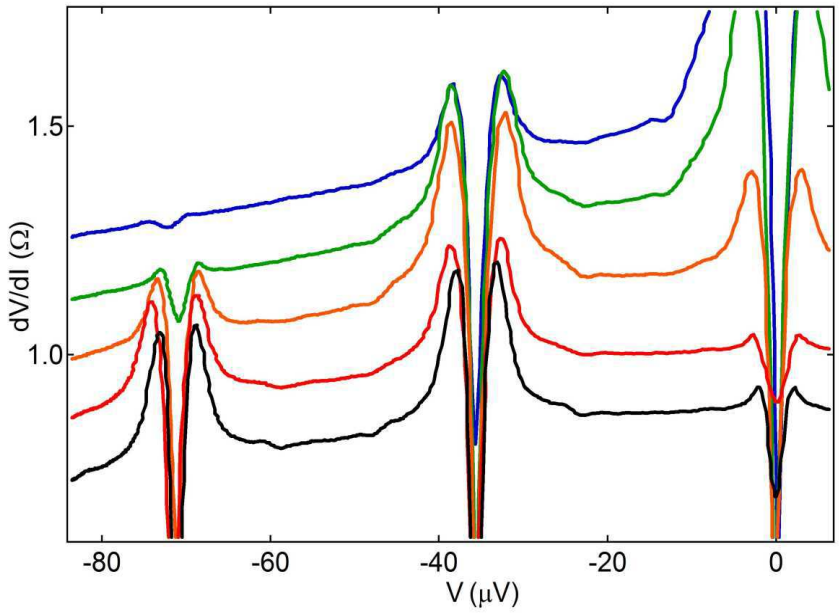

Figure 2.22: Dynamical resistance taken at temperature T=40 mK with microwave frequency $\nu_{\rm rf}$ = 17.35 GHz with different power, from bottom to top: 0 (black), 5 (red), 10 (orange), 15 (green), 20 dBm (blue). The first curve is given without shift, and each subsequent curve is shifted vertically by 0.13 Ω. The large dips correspond to the Shapiro resonances.

analogy, we expect the sideband resonances' amplitudes to scale with ${I_n}^2$, where I_n are the Shapiro steps (which, in turn, follow the Bessel functions with the square root of irradiated power). In Fig. 2.22 we show data from the measurement of the dynamical resistance for junctions irradiated with microwave frequency $\nu_{\rm rf}$ = 17.35 GHz and power varying from 0 to 20 dBm in steps of 5 dBm (bottom to top). The bottom curve is given without shift, and each subsequent curve is shifted vertically. We see the amplitude of the ferromagnetic resonances change with power, following the change in the main dip amplitude, which represents I_n.

2.6 Field dependence of the resonant modes

In this Section we shall investigate the field dependence of the low frequency modes (LFM), observed typically at 10 μV, in the dynamical resistance of the ferromagnetic Josephson junctions. The field is applied in the y direction, along the electrodes, and z is perpendicular

to the junction surface (and parallel to the direction of current), see Fig. 1.5.
The current through the junction is

$$I = \frac{V}{R} + \frac{{I_C}^2(H)}{2V}R - 2\pi I_C(0)\frac{\Phi_{\rm rf}}{\Phi_0}\left[F_x\chi_x''(\omega_J) + F_y\chi_y''(\omega_J)\right] \tag{2.10}$$

where V is the voltage across the junction, R is the junction resistance, I_C is the critical current, Φ_0 is the flux quantum, $\Phi_{\rm rf} = (2aL)B_{\rm rf} = (2aL)\mu_0 I_C(0)/L$ is the flux due to the radio frequency field and $F_x = (1/12)(I_C(H)/I_C)^2$ and $F_y = (2/x^2)[1 + \sin(x/2)\cos(x/2) + ((13/12) - (4/x^2))\sin^2(x/2)]$, $x = kL$, reflect the geometrical structure of coupling to the magnetic modes. We have used the usual form for the imaginary part of magnetic susceptibility

$$\chi_{x,y}''(V) \approx \gamma_e M_z \left[\frac{\sigma}{(V - V_s)^2 + \sigma^2}\right], \tag{2.11}$$

where M_z is the magnetization, γ_e is the gyromagnetic ratio, V_s is the resonance voltage corresponding to the spin-wave frequency $\omega_s = (2e/\hbar)\,V_s$ and σ is the resonance width. As we shall see later, only χ_x'' but not χ_y'' contributes to the resonant signal. So we can compact Eq. (2.10) into

$$I(V,H) = \frac{V}{R} + \frac{{I_C}^2(H)}{2V}R - {I_C(0)}^2\,\frac{A(H)\,\sigma}{\sigma^2 + (V - V_s(H))^2}, \tag{2.12}$$

where $A(H) = 2\pi\gamma_e\mu_0 M_z F_x(H)$ is the resonance amplitude. Here we have used the theory for the FMR resonances to describe the LFM modes. While we can not explain the frequency of the LFM modes, we show they have a field dependence, indicating they are of the ferromagnetic origin.

The data shown in Fig. 2.23 are taken with a lock-in amplifier as detailed in 2.2.3. The second derivatives d^2V/dI^2 are taken at 35 mK for different values of in-plane field. The dc bias current is a linear ramp going to 80 μA, with a typical ramp speed of 500 μHz, the

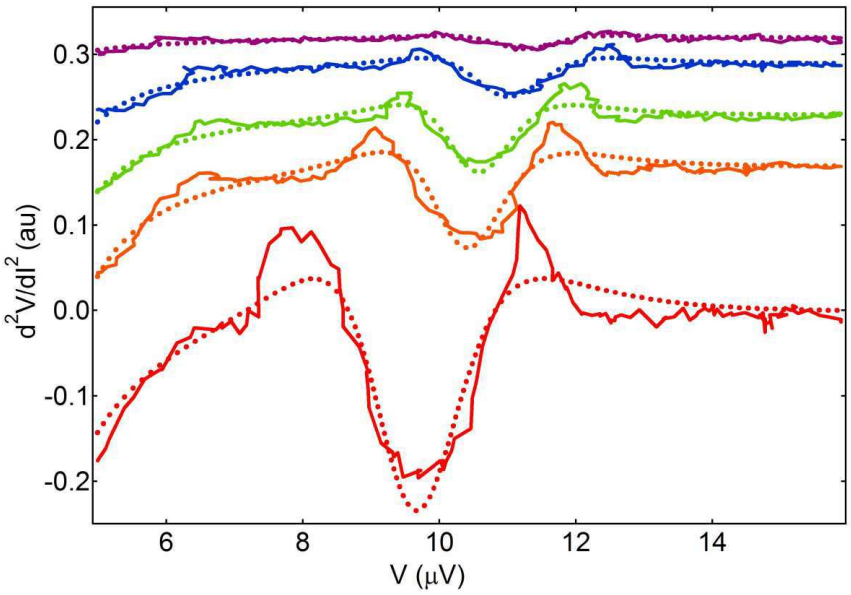

Figure 2.23: Second derivative d^2V/dI^2 of the inverse IV characteristics taken at 42 mK for various values of the external field applied in plane. Colors represent external magnetic field values: 0 (red), 327 G (orange), 360 G (green), 400 G (blue) and 800 G (violet). Solid curves are experimental data, while dotted curves are a fit using Eq. (2.12).

ac bias current is $1\,\mu$A with a frequency of 177.7 Hz. The voltage is amplified 100 times, the ac and dc components are filtered separately, and the ac component is measured with a lock-in amplifier in the second harmonic mode, giving d^2V/dI^2. The main challenge of this measurement was to control the drift of the amplifiers, going up to 1 μV over typically one hour. The measurement was therefore taken sweeping back and forth several times, and this significantly reduced the error in V. The solid curves represent experimental data, and the dotted curves are a fit using Eq. (2.12). The curves are shifted vertically for clarity. Field values are, from bottom to top: 0 (red), 327 G (orange), 360 G (green), 400 G (blue) and 800 G (violet). A commercial Hall probe was mounted on the sample-holder and the field was carefully calibrated.

The LFM shows a linear increase with $\mathbf{H}$ which implies the relevant $\mathbf{M}$ has an appreciable component parallel to $\mathbf{H}$, t.i. in the y direction. In turn this implies that χ''_x, but not χ''_y, contributes to the signal. The coupling to such a mode follows $I_C(H)^2$, as is seen

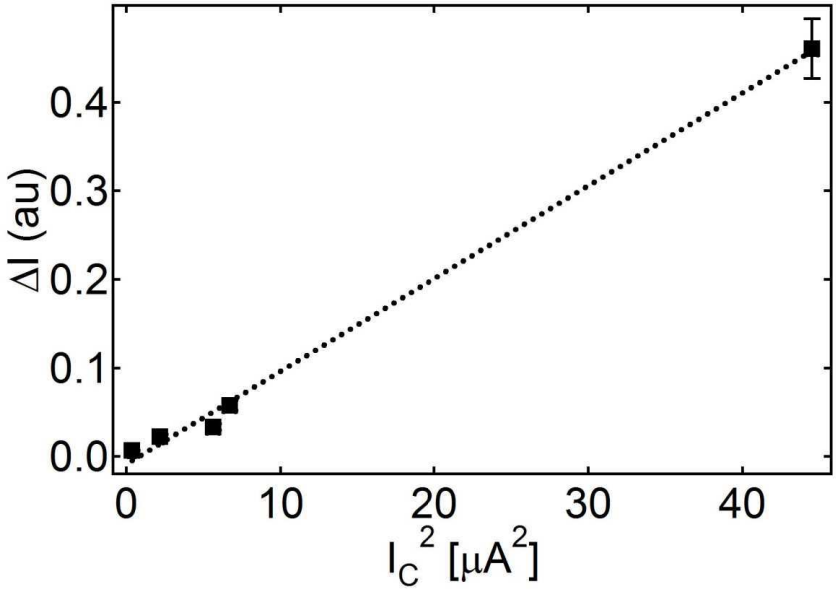

Figure 2.24: The dip amplitude in the IV characteristics ΔI corresponding to the LFM, as a function of ${I_C}^2$ when modulating the critical current with the external magnetic field. The measurement is taken at 35 mK.

experimentally. In the stripe structure the walls have a mixed Bloch-Néel character with the Bloch component in the y direction. In Fig. 2.24 we show the integrated resonance amplitude ΔI corresponding to the depression in the IV curve, as function of ${I_C}^2$. We confirm the scaling law predicted by theory. The dip amplitude ΔI is integrated from the dV/dI data taken simultaneously with the d^2V/dI^2 data shown in Fig. 2.12.

2.7 Comparison with the cavity ferromagnetic resonance measurements

In order to learn more about the spin-wave spectrum in 20 nm thin films of 10 % $Pd_{0.9}Ni_{0.1}$, we fabricated a macroscopic layer and investigated its spectrum in a cavity FMR spectrometer at low temperature.

We have fabricated a trilayer consisting of 50 nm of Nb, 20 nm of $Pd_{0.9}Ni_{0.1}$ and 50 nm of

Nb, with surface of 6 mm × 8 mm in the same way as the junctions, in ultra high vacuum with 10^{-9} mbar base pressure.

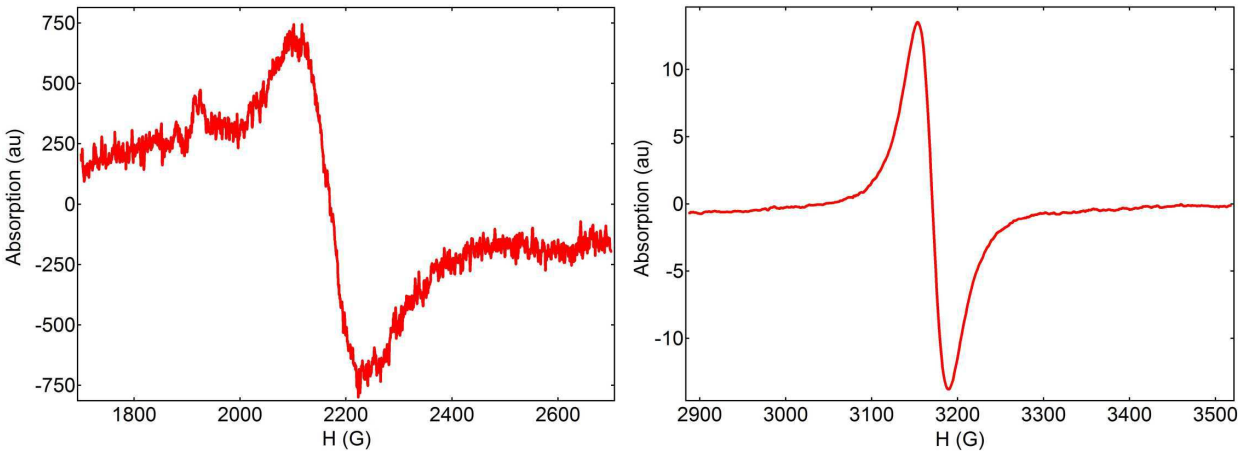

Figure 2.25: Standard cavity ferromagnetic resonance absorption signal for a macroscopic trilayer Nb (50 nm) / $Pd_{0.9}Ni_{0.1}$ (20 nm) / Nb (50 nm) taken at 10.5 K (left panel) and at 4.2 K (right panel), above and below the superconducting transition temperature. The cavity frequency is 9.46 GHz, with typical rf power of 2 mW and a field modulation of 5 G.

The measurements presented in Fig. 2.25 were performed on the macroscopic trilayer with a Bruker EMX electron-spin resonance spectrometer equipped with an X-band (9.46 GHz) TE_{104} resonant cavity and an Oxford ESR 900 continuous flow liquid helium cryostat. Data were taken using a typical rf power of 2 mW and a field modulation of 5 G. On the left panel is the absorption signal taken at 10.5 K, and on the right at 4.2 K, above and under the superconducting transition of Nb.

Experimentally the two perpendicular directions in the $x0y$ plane show quite similar magnetic behaviour. In this case $\chi''_y = \chi''_x$ and the resonance is given by

$$\omega_s = \gamma_e \sqrt{(H_K - 4\pi M_S)^2 - H^2}, \tag{2.13}$$

where H_K is the anisotropy field, M_S the saturation magnetization and γ_e the gyromagnetic ratio. We take $\gamma_e = g\mu_B/\hbar$ where $g = 2$. From the magnetostatic measurements we have $H_K = 4900$ G and $M_S = 929$ G (see Section 2.2). The downward quadratic trend of $\omega_s(H)$

is characteristic of the case when a field is perpendicular to the magnetization.

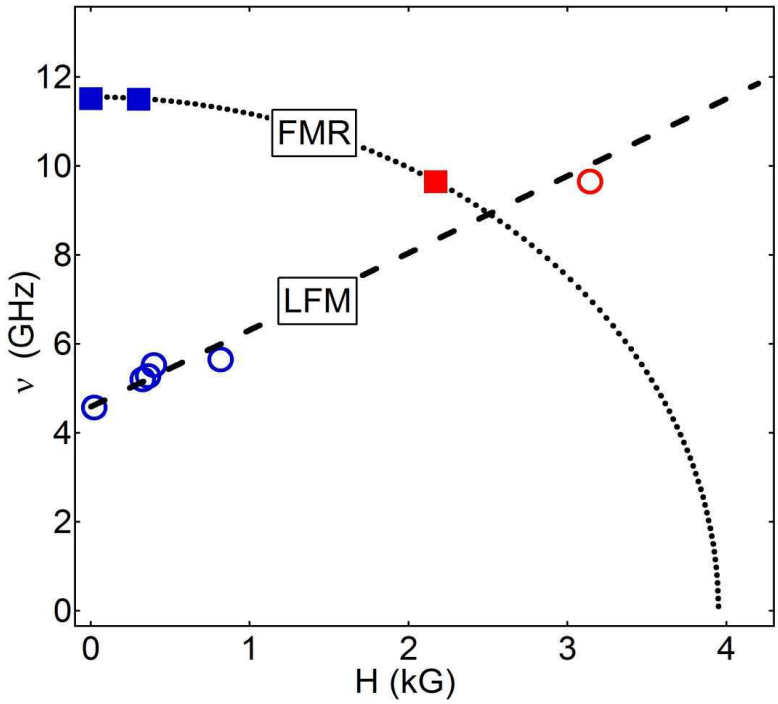

Figure 2.26: Comparison of the two resonant modes in the Josephson junction at 35 mK (blue markers) and in the macroscopic trilayer at 10.5 K (red full square) and at 4.2 K (red open circle). The dotted curve is a FMR mode calculated by the Kittel formula, Eq. (2.13), without fitting parameters, and the dashed line is a linear fit for the low frequency mode (LFM). FMR data are represented in full squares and the LFM data in open circles.

Films with a perpendicular **M** form stripe domains. We estimate the domain size $p \sim 50$ nm, much less than our junction dimensions. Previous conventional magnetic resonance studies[70] of such domain structures exhibit a rich spectrum. The FMR mode occurs at $V_s = 23\,\mu$V. This is unambiguously identified as such, since the frequency $\omega_s = 2eV_s/\hbar$ agrees, without fitting parameters, with the Kittel formula, Eq. (2.13). This is shown in Fig. 2.26. The blue squares represent the FMR mode at 23 μV measured with a Josephson junction, while the red square represents the resonance measured on a trilayer. Since the Josephson signal is suppressed by a large applied magnetic field, the measurement of the field dependence is limited to fields smaller than about 1000 G, corresponding to two flux quanta in the junction. The cavity FMR occurs at 2160 G, again exactly as predicted by

Eq. (2.13). This is the central result and the main proof that we actually measure the FMR resonances with the Josephson junction.

Unlike the FMR mode, the frequency of the LFM does not follow Eq. (2.13). The field dependence of this mode has been studied in more detail in the second derivative, d^2V/dI^2 (previous Section), and is reported as blue open circles in Fig. 2.26. Measurements were limited in field due to the rapid decrease of the signal above 1000 G. The linear trend in the low field junction data can be extrapolated to pass through the second cavity mode (right panel, Fig. 2.25). The LFM shows a linear increase with **H** and which implies the relevant **M** has an appreciable component parallel to **H**, that is in the y direction.

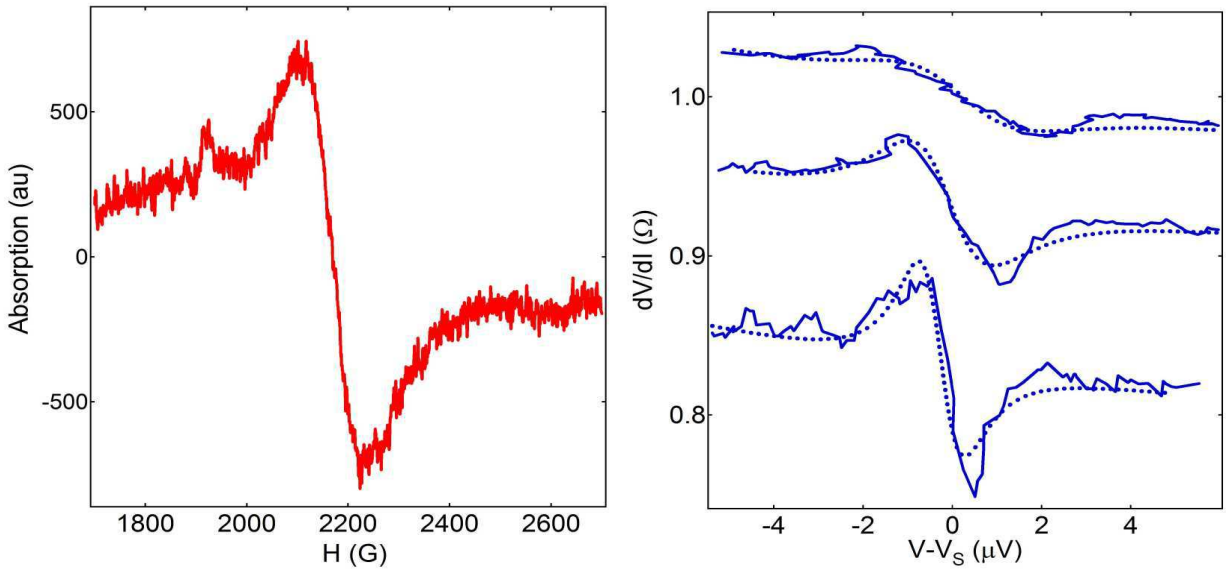

Figure 2.27: **Left**: The FMR absorption as a function of the magnetic field H measured on a macroscopic trilayer. **Right**: The absorption (dynamical resistance) as a function of voltage V measured with a Josephson junction (full curves). Three curves correspond to the absorption measured with three values of ac modulation voltage - from top to bottom: 2 μV, 1 μV and 0.5 μV. The dotted lines are a fit using Eq. (2.5).

Now we shall discuss the resonance width and amplitude. The peak-to-peak width of the junction result is comparable to that of the conventional resonance (150 G). The junction result presented on the right panel of Fig. 2.27 contains an extrinsic broadening caused by

a lock-in modulation voltage, ranging from 2 μV and 0.5 μV, top to bottom. For the ac modulation voltage of 0.5 μV, we see the finer features of the resonance, from which we infer that the smearing is becoming negligible. Thus obtained junction resonance has a width close to 0.5 μV, which corresponds to the conventional resonance width (150 G - left panel of Fig. 2.27). The junction resonance amplitude corresponds to a resonant susceptibility of approximately 10, which is also consistent with the trilayer values.

The cavity FMR measurements were performed by F. Beuneu at Laboratoire des Solides Irradiés, École Polytechnique, in Palaiseau.

2.8 Noise of the overdamped ferromagnetic Josephson junctions

We have also investigated the phase dynamics of the overdamped ferromagnetic Josephson junctions by measuring the statistics of switching from the non-dissipative into the dissipative state. The switching statistics contain information on the Josephson phase noise. We are interested to see if the phase behaves as expected in the thermal limit, and if there is additional noise due to the ferromagnetic modes.

We measure the histograms in the same way we measured the Fraunhofer pattern, with a counter, only this time we keep the whole statistics of switching, not just the average switching current. The switching histogram contains information on the effective temperature.

The measurement details are the following. We bias the junction with current in the form of a sawtooth ramp of frequency $\nu_b = 347$ Hz and amplitude of $V_b = 90$ mV across $R_b = 10$ kΩ, making it a $I_b = V_b/R_b = 9\,\mu$A ramp, with the critical current of the junction $I_C = 6.7\,\mu$A. We trigger at the finite voltage of $1.5\,\mu$V. The voltage is amplified 2×10^5 times. We filter the voltage with a low band pass with a cutoff frequency of 10 kHz. The counter measures

the time between the start of the ramp and the triggering event, which is proportional to the switching current. We accumulate 250 000 points in each histogram. The counter time constant is 1.26 μs. The measurement is done in a dilution refrigerator, at temperatures ranging from 35 mK to 4 K. The field is applied with a superconducting coil, ranging up to 1000 G in this measurement, in plane with the junction.

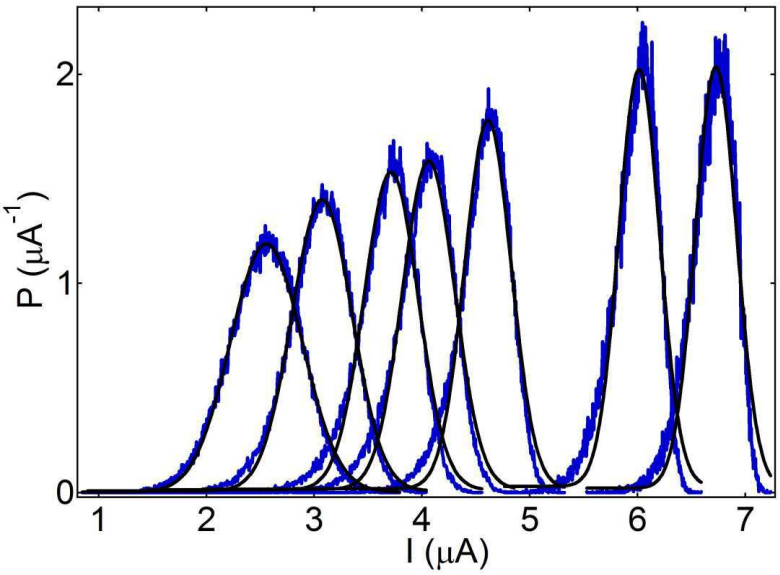

Figure 2.28: Switching histograms as function of temperature in zero external field. Respectively from the right T=1.95, 2.95, 4.2, 4.7, 5.1, 5.76, and 6.45 K. Measurement is given in blue curves, while black curves are a gaussian fit.

The behavior of current biased Josephson junctions can be seen as movement of the Josephson phase in the tilted-washboard potential. There are two possible ways for the Josephson phase to go over the potential barrier, corresponding to the switching into the dissipative state - thermal activation and quantum tunneling. For highly overdamped junctions, the crossover between the two regimes is for $\hbar\omega_T = k_B T^*$, where $\omega_T = \omega_0^2/2\pi\eta$, ω_0 being the Josephson plasma frequency and $\eta = (RC)^{-1}$ the damping parameter [100]. Note that $\omega_T = (2e/\hbar)I_C R$ does not depend on the junction capacitance. In our case typically $R = 0.9\,\Omega$, $I_C = 6.7\,\mu$A, so $\omega_T = 2.9 \times 10^9$ rad/s. The frequency $\nu_T = \omega_T/2\pi = 0.46$ GHz corresponds to the crossover temperature $T^* = 11$ mK, so we stay in the thermal regime.

We investigate the histogram width as function of temperature between 1.95 K and 6.45 K. In Fig. 2.28 we show the measured histograms (blue curves), each fitted with a gaussian curve (black curve). The gaussian is a fairly good approximation when estimating the histogram width.

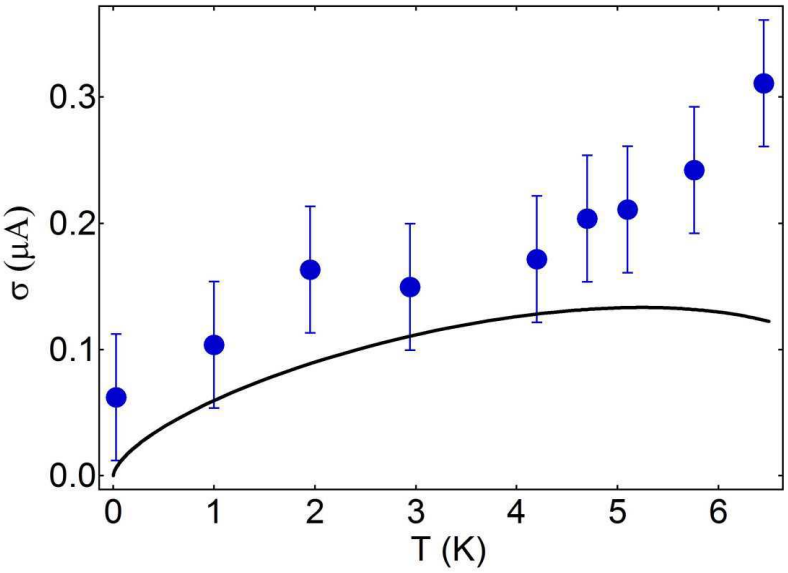

Figure 2.29: Measured histogram standard deviation σ as function of temperature (markers), corrected for the extrinsic width coming from the measurement procedure as explained in the text. The full line is the fit using the formula of Garg[73] for overdamped junctions in the thermal regime.

In the thermal limit we expect the histogram standard deviation (width) to depend on the temperature as $\sigma \sim T^{2/3}$[72] for $T \to 0$. In Fig. 2.29 we use the asymptotic expression for σ given by Garg, Eq. (1.50), for overdamped junctions in the thermal regime[73].

We need to separate the intrinsic histogram width coming from the thermal smearing σ from the extrinsic width σ_{ext} coming from the way we measure switching. Since we always trigger at finite voltage, $1.5\,\mu$V in this measurement, and we have typically $\delta V_{ext} = 0.5\,\mu V$ voltage noise, which is seen as $\delta I_{ext} = R(T)^{-1}\,\delta V_{ext}$ noise in current. When inspecting the IV curves as a function of T, we see that around $V = 1.5\,\mu$V we can approximate $R(T)^{-1}$ as $R(T)^{-1} = 0.47 + 1.36\,T/T_C$. This form of $R(T)^{-1}$ is obtained as a fit from Fig. 2.8. At

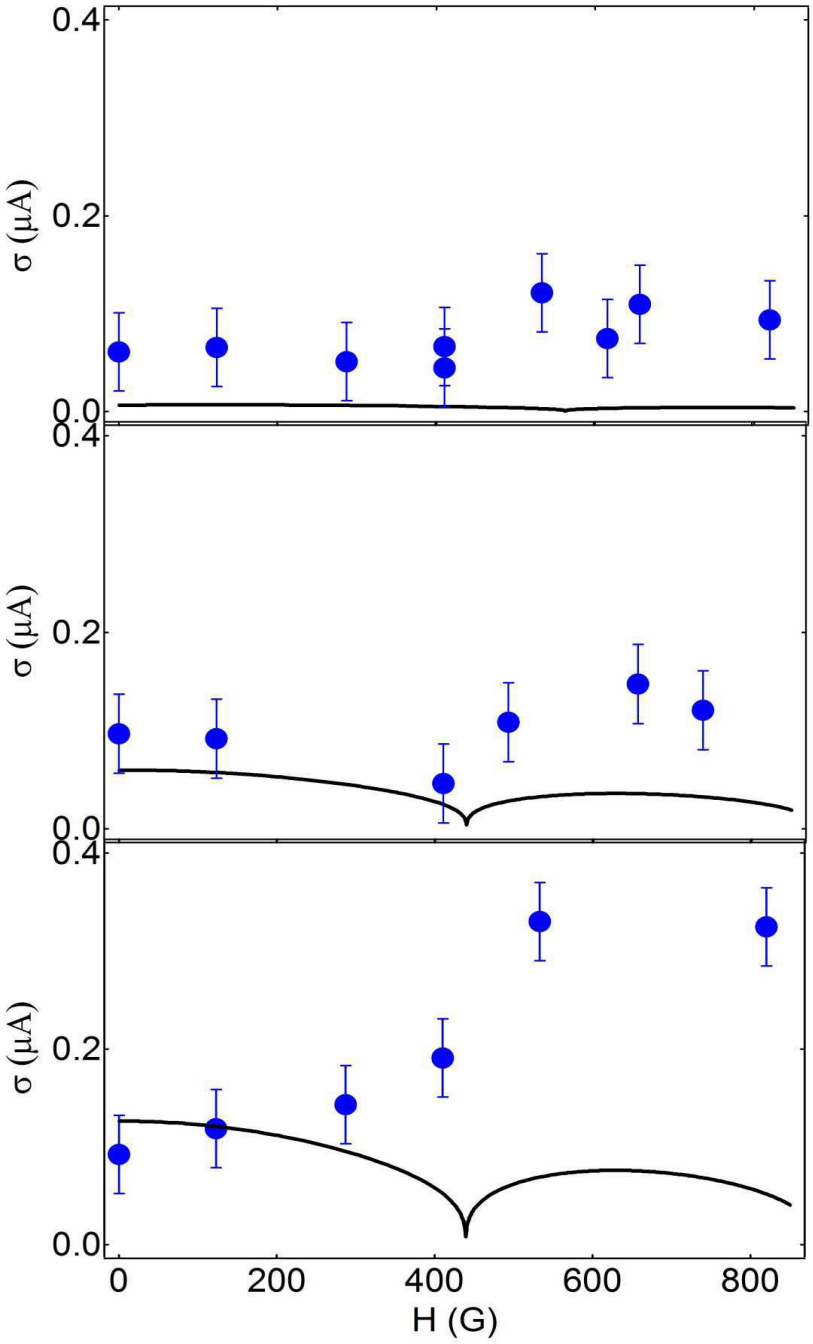

Figure 2.30: Measured histogram standard deviation σ as function of the external field (markers), corrected for the extrinsic width coming from the measurement procedure as explained in the text. The temperature is (top to bottom): 35 mK, 1 K and 4 K. The full line is the fit using the formula of Garg[73] for overdamped junctions in the thermal regime.

low temperature $\delta I \sim 0.25\,\mu A$, while at high temperature $\delta I \sim 0.8\,\mu A$. This is only valid around the triggering voltage of $1.5\,\mu$V.

We then assume that $\delta I_{ext} = 6\,\sigma_{ext}$, since we are close to the Gaussian distribution, where 99.7 % of δI_{ext} is comprised in $6\,\sigma_{ext}$, so

$$\sigma_{ext}(T) = \frac{1}{6}(0.47 + 1.36\,T/T_C)\,\delta V_{ext}.$$

We subtract the extrinsic contribution from the measured value σ_m, i.e. $\sigma = \sigma_m - \sigma_{ext}$. In Fig. 2.29 we show σ (markers) and the fit (full curve) as function of temperature in zero external field. We see that at lower temperatures the fit is satisfactory, albeit with a constant $0.05\,\mu$A shift, while at higher temperatures, the histogram width is larger than expected.

In Fig. 2.30 we show σ (markers) and the fit (full curve) as function of the external field for three different values of temperature from top to bottom: 35 mK, 1 K and 4 K. We see that at $T = 35$ mK the measured histogram deviation σ is significantly larger than expected from theory. For $T = 1$ K the fit reproduces the data rather well at low field, and at $T = 4$ K we see σ rise significantly with field. The histogram deviation σ is higher for fields above 500 G. More work is needed to explain the increase in the histogram width.

Chapter 3

Proper phase dynamics of the ferromagnetic Josephson junctions

3.1 Principle of experiment

Nonlinearity of the Josephson effect is well known and gives rise to interesting phenomena. The Josephson phase in the tilted washboard potential is a realization of a nonlinear oscillator. Under the external microwave irradiation, the Josephson phase in the non-dissipative regime can show bifurcation[84]. In this Chapter we show for the first time a novel type of bifurcation - dynamical bifurcation - set off at certain bias ramp frequencies, comparable to the inverse phase relaxation time. For low ramp frequency, switching takes place for current values close to the critical current. When the ramp frequency becomes comparable to the inverse phase relaxation time $\tau_{\varphi}^{-1} \sim (R_{qp}C)^{-1}$, where R_{qp} is the quasiparticle resistance and C capacitance, the phase can either relax to the bottom of the potential well and switch near the critical current, or switch early, at much lower, retrapping, current. In a way, we perform a pump-probe measurement: we tilt the washboard potential fast, and then probe the phase dynamics, which we detect as voltage generated across the junction[101].

In this Chapter, first we measure the expected equilibrium phase dynamics when biasing with a slow ramp - we confirm that the phase is activated thermally. Then, with higher ramp frequency, we measure bifurcation as a bimodal switching distribution, where the two switching current values have frequency dependent probabilities of occurrence. We calculate the bifurcation probability numerically within the RCSJ model with a time-dependent current bias and make a correspondence with the experiment. Finally we include the external

magnetic field in the RCSJ model and discuss the obtained general solutions, identifying the resonances as Fiske steps. We show that the ferromagnetic Josephson junctions have a different dispersion relation $\omega(k)$ of Fiske resonances compared to the non-ferromagnetic ones.

3.2 Sample fabrication

The PdNi-based ferromagnetic Josephson junctions have been fabricated previously in the group[98]. On these junctions was demonstrated the transition from 0 to π state as function of the ferromagnetic barrier thickness, Fig. 3.4 [40]. I will briefly repeat here the fabrication procedure.

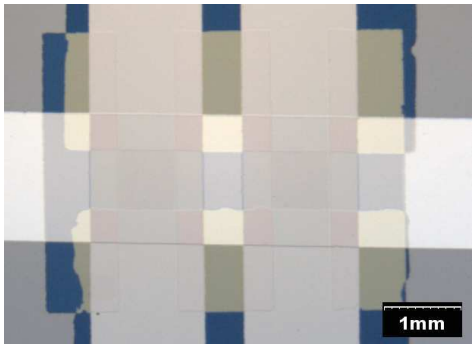

Figure 3.1: Photo of two junctions on a wafer, taken with an optical microscope. The white horizontal stripe is the bottom layer of Nb, and the two vertical stripes are PdNi/Nb bilayers. Yellow stripes defining the junction surface are layers of SiO evaporated through a mechanical mask.

First was evaporated 150 nm of Nb on a Si wafer covered with a 50 nm layer of SiO. This was followed by 50 nm of Al. Then the Al was oxidized for 1 minute at the pressure of 8×10^{-2} mbar. Then the junction surface was defined by evaporating a 50 nm thick SiO layer through a mechanical mask. The next step was the evaporation of the ferromagnetic PdNi with 10% Ni, with thicknesses ranging between 0 and 100 Å. The final layer was 50 nm of Nb. The evaporation pressure was 10^{-9} – 10^{-8} mbar, with typical rates of 2 Å/s. Critical temperature of Nb is around 9 K. The junction surface is typically 0.6 mm $\times$ 0.8

mm, and their normal resistance around 0.3 Ω at room temperature. Each wafer contained 8 junctions, each two with the same thickness of the ferromagnetic layer. When mounting the samples, we used silver paint to adhere the silver wire contacts onto the Nb pads.

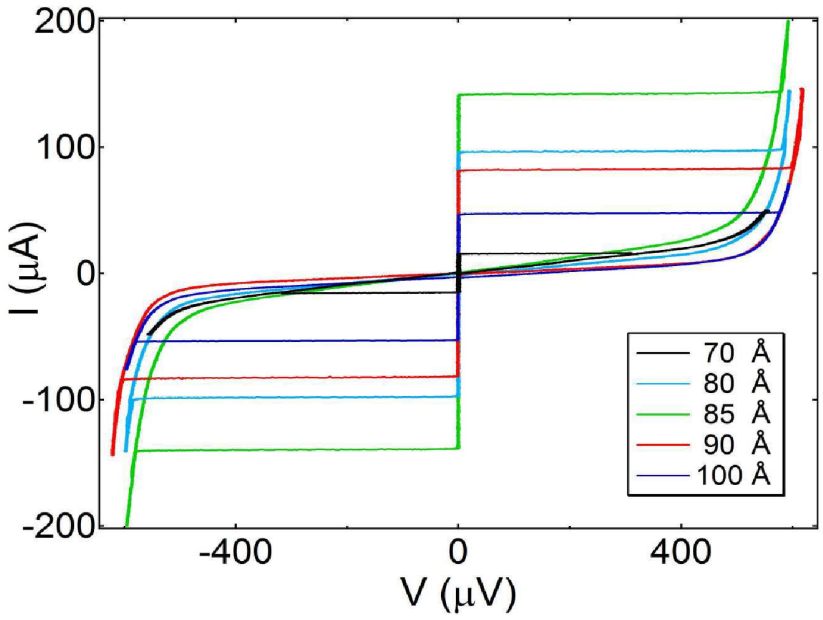

Figure 3.2: IV characteristics of the Nb/AlO/PdNi/Nb junctions with various PdNi layer thicknesses, taken at 300 mK.

The optical microscope photo of the wafer with two junctions is shown in Fig. 3.1. The white horizontal stripe is the bottom layer of Nb, and the two vertical stripes are PdNi/Nb bilayers. Yellow stripes defining the junction surface are layers of SiO evaporated through a mechanical mask.

Since the junctions were fabricated earlier, first we checked that their properties had not changed. The junctions measured in this Chapter present the same critical current within 10% as when they were fabricated. The normal resistance is also reproduced. In Fig. 3.2 we see the IV curves of all the junctions in the π state and at the $0 - \pi$ transition, taken at 300 mK with low bias frequency. The IV curves are hysteretic, as the junctions are underdamped. Typical critical currents are around 100 μA, except for the junction at the $0 - \pi$ transition, with I_C =15 μA. The retrapping current I_r is practically zero. This stems

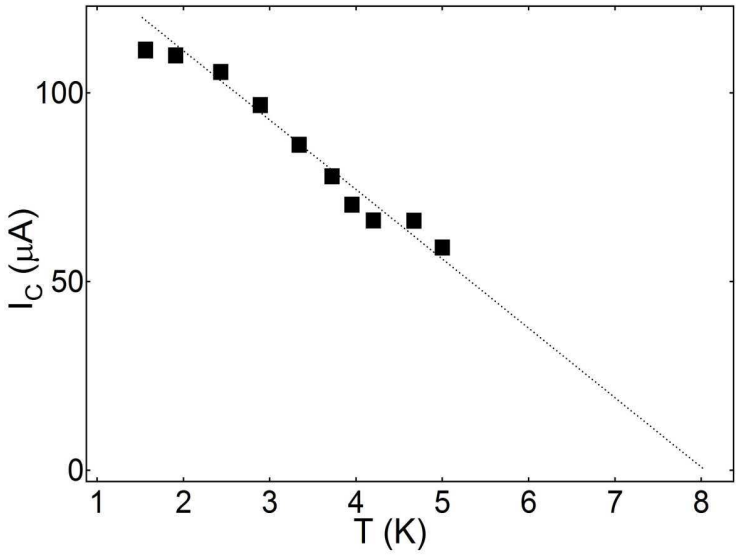

Figure 3.3: Critical current I_C as function of temperature for the Nb/AlO/PdNi/Nb junction with 85 $\mathring{A}$ of PdNi.

from relatively high junction capacitance of around 40 nF, making the quality factor Q of the order of 3000, and $I_r \sim 4I_C/\pi Q$. The gap is around 600 μV, in accord with what we expect with the presence of the ferromagnet. On one side we have the bilayer of Nb/Al, with the gap of around 600 μV due to the proximity effect, and on the other side a bilayer of PdNi/Nb, with a very small gap, suppressed by the ferromagnet.

In Fig. 3.3 we show the critical current of junction with 85 $\mathring{A}$ of PdNi as function of temperature. The dependence is linear at higher temperature, as previously seen in [98]. The junction critical temperature is $T_C = 8.3 \pm 0.2$ K. We have also investigated the dependence of the critical current on the external magnetic field, to be detailed in the Section dedicated to the Fiske resonances in this Chapter. The Fraunhofer curves $I_C(H)$ are regular, such as in Fig. 3.26 for the junction with 85 $\mathring{A}$ of PdNi, indicating good junction quality and uniform current distribution.

In Fig. 3.4 we show the measurement of the Josephson coupling $I_C R_n$ as function of the PdNi layer thickness at T=1.5 K, taken in 2001 (black markers), compared to the same measurement taken during this work at T=300 mK (red markers stand for the wafer 56J

and the green marker for the wafer 55W). We have also measured one junction in the 0 state, as well as an SIS junction, not shown here since their Josephson coupling is much larger. The critical current does not change between 300 mK and 1.5 K. We see the transition from 0 to the π state as function of thickness, the critical current becoming zero at the transition, at 68 $\mathring{A}$. The fit (full curve) stems from the Usadel equation, and is detailed in [98]. We see that the junctions have not changed with time. We summarize the junction properties in Tables 3.1 and 3.2, corresponding to the two measured wafers, 56J and 55W.

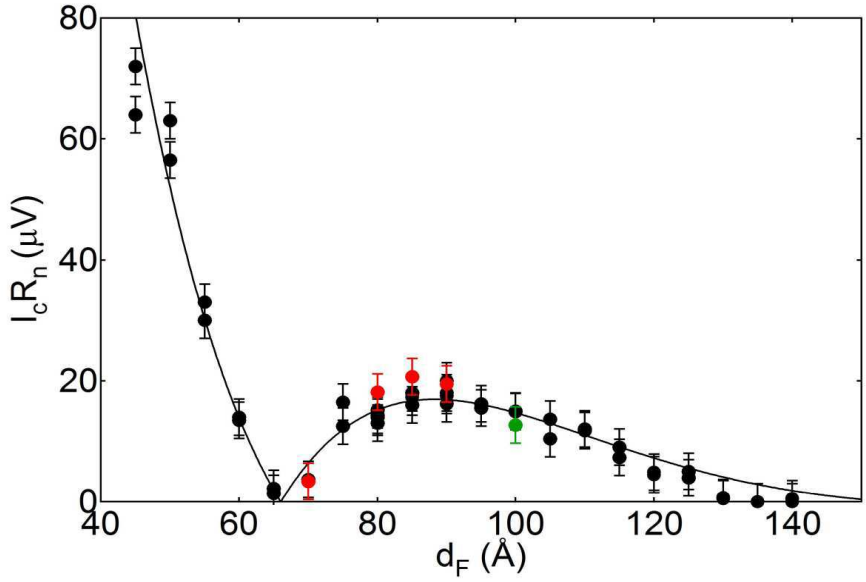

Figure 3.4: Josephson coupling I_CR_n as function of the PdNi layer thickness. Black markers correspond to the junctions measured at T=1.5 K by T. Kontos [98], the red markers correspond to the same junctions on the wafer 56J measured now and the green marker corresponds to the junction on the wafer 55W measured now. Our measurement is taken at T=300 mK.

The capacitance value of 42 nF is estimated assuming the dielectric constant of Al_2O_3 of 10, and the oxide layer thickness of 10 Å, and it is assumed to be the same for both wafers. The plasma frequency $\nu_0 = \omega_0/2\pi = \frac{1}{2\pi}\sqrt{2eI_C/\hbar C}$ is of the order of 500 MHz, and the quality factor $Q = \omega_0 R_{qp} C$ is of the order of 3 000 for junctions in the π state that we will measure

PdNi 56J						
N^0	a_{PdNi} (Å)	state	I_C (μA)	R_n (Ω)	R_{qp} (Ω)	C (nF)
2	70	$0-\pi$	15	0.34	19.3	42
4	80	π	102	0.27	24	42
5	85	π	110 – 130	0.28	23	42
8	90	π	86	0.34	50	42

Table 3.1: Summary of junction properties for wafer PdNi 56J. The values of I_C and R_{qp} are measured at T=300 mK, and R_n at room temperature.

PdNi 55W						
N^0	a_{PdNi} (Å)	state	I_C (μA)	R_n (Ω)	R_{qp} (Ω)	C (nF)
2	50	0	1 200	0.125	0.8	42
5	100	π	50	0.255	38.7	42
6	100	π	50	0.263	8.5	42
7	0	non-ferro	10 000	0.148	0.23	42

Table 3.2: Summary of junction properties for wafer PdNi 55W. The values of I_C and R_{qp} are measured at T=300 mK, and R_n at room temperature.

in detail. An alternative way to estimate capacitance stems from the measurement of the Fiske resonances, to be detailed at the end of this Chapter. The quasiparticle resistance R_{qp} is measured as the slope of the retrapping branch of the IV characteristics at voltage close to zero. We will proceed to show that the phase relaxation is governed by the quasiparticle resistance.

3.3 Experimental setup

We bias the junction with a periodic low frequency sawtooth ramp. We measure the junction switching from the non-dissipative into the dissipative state with a counter, measuring the time that elapses between the start of the ramp and the appearance of finite voltage, and that time is proportional to the switching current. The measurement setup is shown in Fig. 3.5.

We bias the junction with a sawtooth ramp (shown in blue in Figs. 3.5 and 3.6) of amplitude

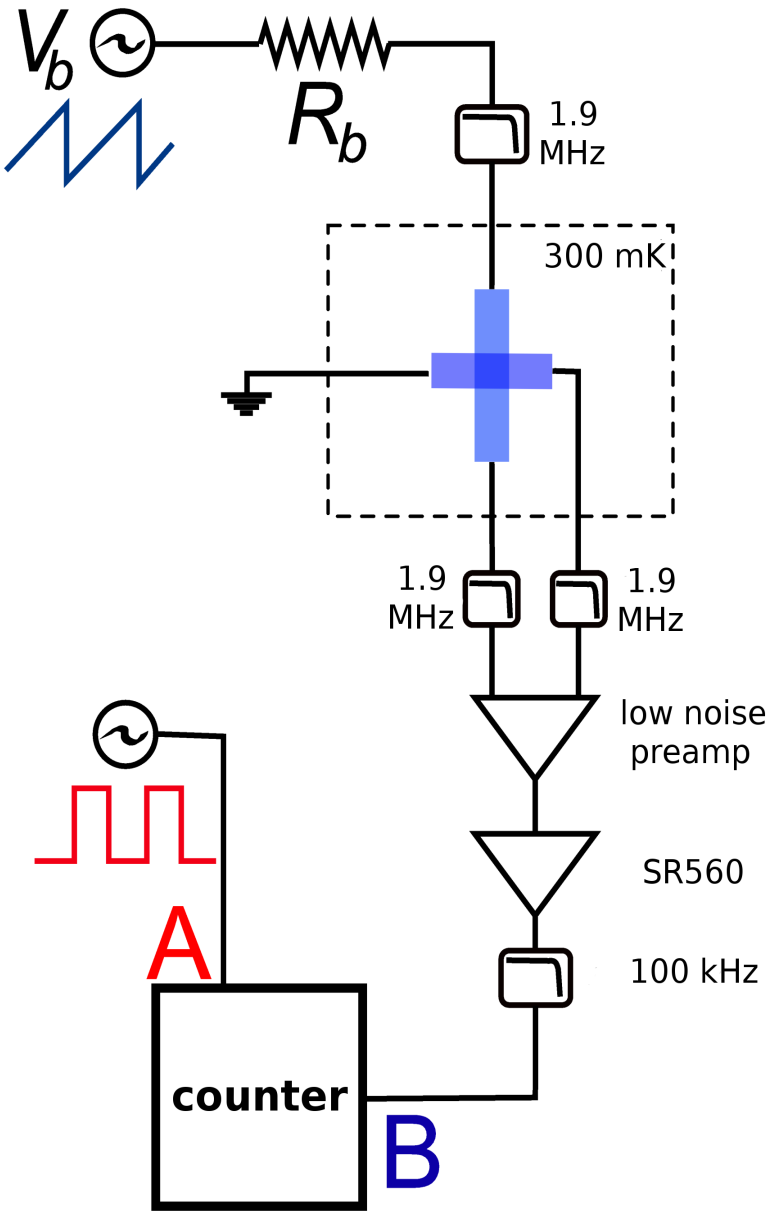

Figure 3.5: The experimental setup.

V_b and frequency ν_b across the resistance $R_b \gg R_{qp}, R_n$, where R_{qp} and R_n are respectively the quasiparticle and the normal resistance of the junction, making it a current $I_b = V_b/R_b$ ramp, where I_b is higher than the junction critical current I_C. The measurement is four-point. Measured voltage across the junction is amplified in two stages at room temperature, first 100 times with a low-noise preamplifier NF Electronic Inst. LI-75A, and then between

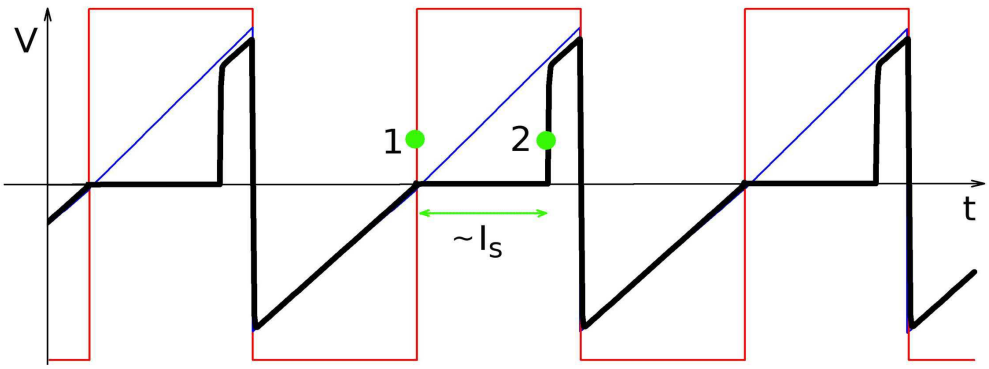

Figure 3.6: The ramp (blue curve), the voltage generated across the junction on channel B (black curve) and the synchronized pulse on channel A (red curve). The counter measures the time t between triggering events 1 and 2, proportional to the switching current $I_S = 2\nu_b I_b t$, where I_b and ν_b are ramp amplitude and frequency respectively.

1 and 10 times with a Stanford SR560 amplifier, which also serves as a low band pass with variable cutoff frequency (we typically set it to 100 kHz). The amplifiers were connected to the power grid. The voltage across the junction enters the B channel of the counter. The A channel of the counter is fed with a synchronized rectangular 3 V pulse, shown in red. All the incoming and outcoming lines are filtered with low band pass 1.9 MHz filters. Not shown in Fig. 3.5 is the resistance of cables, typically around 30 Ω. Also not shown are on-chip RC filters with a cutoff frequency of 1.1 MHz.

The principle of measurement is shown in Fig. 3.6. The black curve is the junction response to the ramp - the voltage $V(t)$ generated across the junction. The counter measures the time t that elapses between the start of the pulse on channel A and the triggering event on channel B, which is proportional to the switching current $I_S = 2\nu_b I_b t$. Since the switching takes place for a certain current I with a certain probability $P(I)$, we accumulate over many cycles the switching histogram $P(I)$, as shown in Fig. 3.7. The red curve is the measurement, and the blue curve is the fit we shall detail later. The histogram is asymmetric.

We performed this measurement in two different cryostats. First we used a ^{4}He 1.2 K

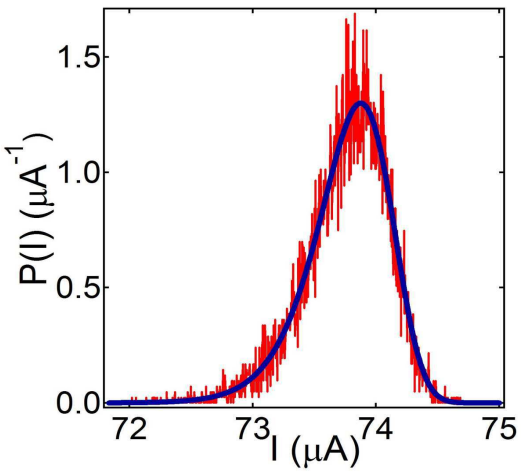

Figure 3.7: A typical histogram. The data is given in the red curve, while in blue is the theoretical fit, to be detailed in the following Section.

cryostat without on-chip filtering. In this setup we had typically 1 μV voltage noise, and we had at 1.2 K the relative histogram width $\sigma/\langle I\rangle \sim 0.5-1\%$, measured for junctions J5 (90 $\mathring{A}$ of PdNi) and J2 (70 $\mathring{A}$) on wafer 56J, respectively. Then we mounted the samples 56J and 55W in the 300 mK ^{3}He "minute" cryostat. We noticed that in this setup there was an extrinsic broadening to all of our histograms, so we introduced on-chip RC filtering. The resistance R is the resistance of each wire of $R_f = 30\,\Omega$, to which we added the capacitance $C_f = 5$ nF, yielding a cutoff frequency $(2\pi R_f C_f)^{-1} = 1.1$ MHz. Note also that the added capacitances are much smaller than the junction capacitance. After the implementation of RC filtering we measured the same histogram widths as in the ^{4}He cryostat.

Another setup variation is the counter. We used two counters, the Fluke PM 6681 counter that outputs raw data (switching time intervals in their consecutive order) with the sampling rate of 1.26 μs per point, accumulating typically tens of thousands of points, and the LeCroy WaveMaster 8600A oscilloscope which outputs automatically generated histograms, with typically 2000 bits and a sampling rate of 1 – 100 MS/s.

For the measurements taken in the 300 mK ^{3}He cryostat, the magnetic field was applied in the junction plane, with an external coil mounting up to several G. One flux quantum

corresponds typically to the field of 150 mG. The whole setup was shielded from the Earth's magnetic field with a mu-metal cage.

3.4 Adiabatic phase dynamics - thermal switching

In this Section we investigate the phase dynamics of the ferromagnetic Josephson junctions in the stationary regime in order to see if there is additional noise coming from the magnetization dynamics, or related to the 0 – π transition. The magnetization couples to the phase via a vector potential $\varphi = \varphi_0 + \int \mathbf{A} d\mathbf{l}$, where $\mathbf{B} = \mathrm{curl}\mathbf{A}$, so in principle the magnetization dynamics can be detected as phase dynamics. The other question is whether the π state is any different than the 0 state in terms of noise. Our primary motivation was to use the π junction as a phase battery, since when embedded in a superconducting loop it generates a phase difference of π without the applied external field, and to that end to investigate the noise of a π junction. For temperatures above the lowest experimentally accessible temperature of 300 mK the switching mechanism of a junction is thermal activation. The temperature of crossover into the quantum regime, determined by the ratio of the junction's plasma frequency and temperature, is around 10 mK. In case there is additional noise, we expect the effective noise temperature to be higher than the bath temperature.

The escape rate with which the Josephson phase escapes the minimum of the tilted washboard potential is

$$\Gamma(I) = a_t(I)\frac{\omega_a(I)}{2\pi}\exp\left(-\frac{\Delta U(I)}{k_B T}\right), \tag{3.1}$$

where $a_t(I)$ is a damping-dependent prefactor (see Table 1.1), ω_a the activation frequency, ΔU the potential barrier and T the temperature. For detailed definitions see Section 1.3.1. The probability distribution $P(I)$ is

$$P(I) = -\frac{d}{dI}W(I) = \frac{\Gamma(I)}{\dot{I}}\exp\left[-\int_0^I \frac{\Gamma(I')}{\dot{I}}dI'\right], \tag{3.2}$$

where $\dot{I} = dI/dt$ is the ramp speed[73] and $W(I)$ the probability that the phase will stay inside the potential well at bias current I.

We have performed a switching measurement in the adiabatic regime on several junctions. The measurement of the switching histograms as function of temperature for the junction with 80 $\mathring{A}$ of PdNi is given in Fig. 3.8. We bias the junction in the form of a sawtooth ramp of amplitude $V_b = 110$ mV and frequency $\nu_b = 37$ Hz across the resistance $R_b = 1$ kΩ, making it a current $I_b = V_b/R_b = 110$ μA ramp, where $I_C = 103\,\mu$A. Measured voltage across the junction is amplified 100 times with a low-noise preamplifier. The cutoff frequency of the low band pass on the SR560 amplifier is 30 kHz. We trigger at 100 μV and accumulate 10^4 points.

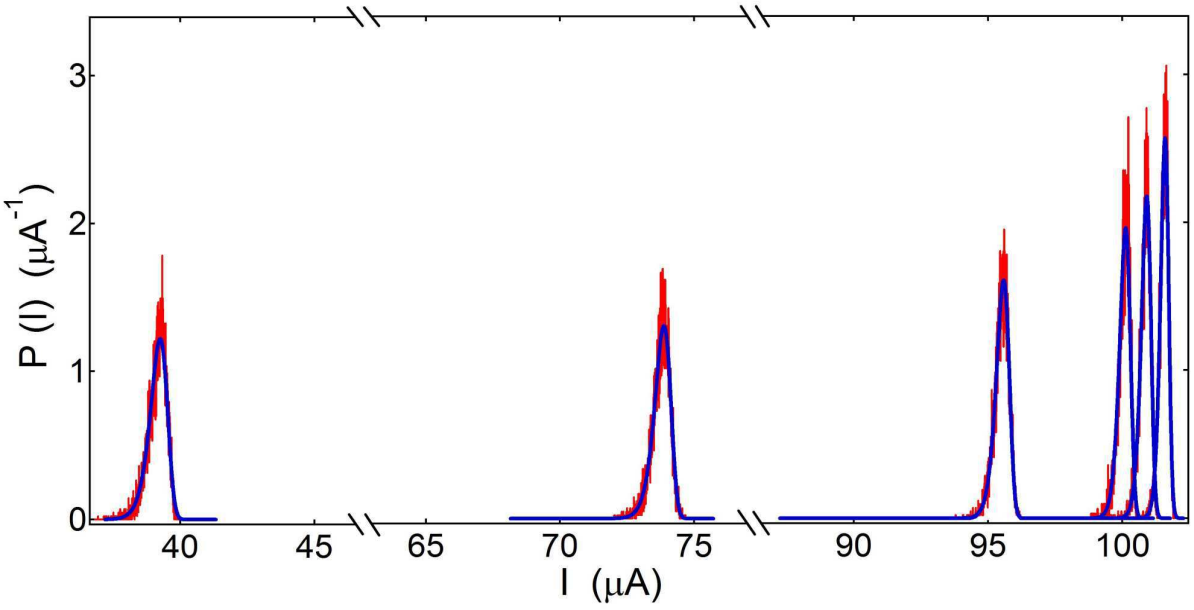

Figure 3.8: Switching histograms for the following temperatures (from right to left): 500 mK, 800 mK, 1.2 K, 2 K, 3 K, 4.2 K. Red curves are experimental results, and blue curves are a fit using Eqs. (3.1) and (3.2) for low damping. The junction is in the π state, with 80 Å of PdNi.

In Fig. 3.8 we show a measurement taken on a ferromagnetic junction in the π state with 80 Å of PdNi for various temperatures. The red curves represent experimental results, and the blue curves represent the fit using the Kramers escape theory, Eqs. (3.1) and (3.2), for

low damping. Between 1 K and 4.2 K we are crossing between low and moderate damping, as we shall detail later. With temperature, the mean switching current $\langle I \rangle$ decays, staying within the few percent of the ideal no-fluctuations critical current $I_C(T)$, and the standard deviation $\sigma = \sqrt{\langle I^2 \rangle - \langle I \rangle^2}$ augments.

In the low damping regime the activation rate depends on the damping parameter β, while for moderate damping it does not.

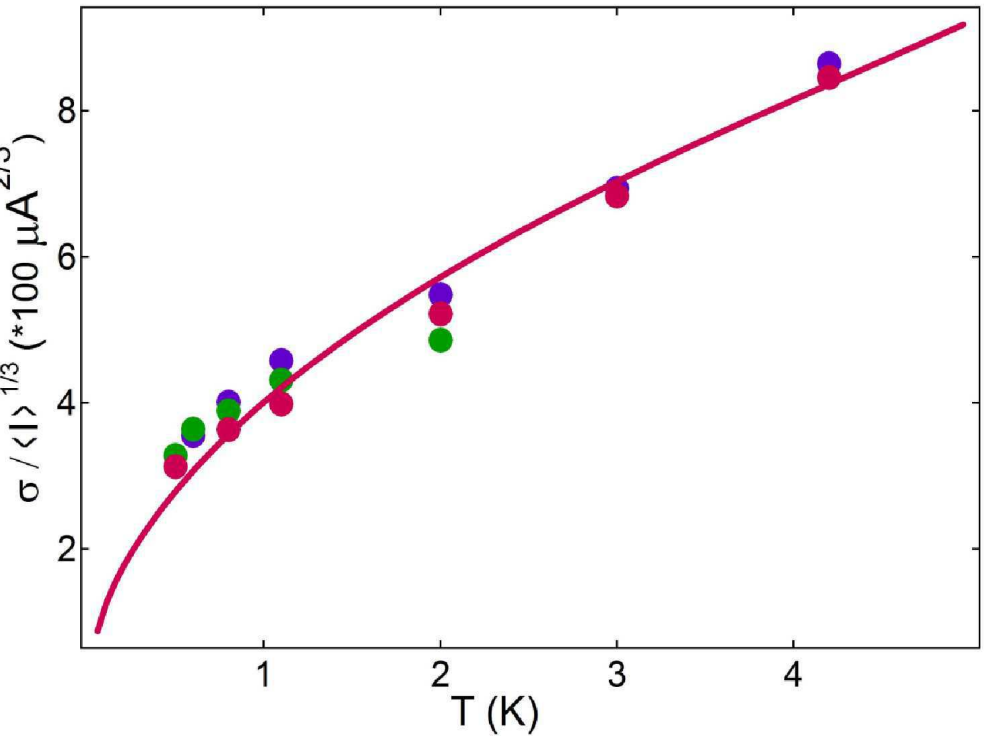

Figure 3.9: The markers are the measured normalized switching histogram widths as function of temperature for three different junctions: 70 $\mathring{A}$ - green, 80 $\mathring{A}$ (same as Fig. 3.8) -purple, and 85 $\mathring{A}$ - blue. The full purple line is the fit in the low damping regime for the junction with 80 $\mathring{A}$ of PdNi, assuming the form for the quasiparticle resistance given in Fig. 3.10.

Now we will look in detail into the dependence of the measured histogram width σ as function of temperature, Fig. 3.9. In general, for moderate damping, $\sigma \sim I_C^{1/3}\sigma^{2/3} \sim \langle I \rangle^{1/3}T^{2/3}$, since we take the switching current $\langle I \rangle$ to be close to the no-fluctuations critical current I_C. In his paper [73], Garg gives the analytical expression for σ, making several simplifying

assumptions for the activation rate, detailed in Section 1.3.1. In Fig. 3.9 we show the measured normalized distribution width $\sigma/\langle I\rangle^{1/3}$ as function of temperature for junctions with 70 $\mathring{A}$ (green markers), 80 $\mathring{A}$ (purple) and 85 $\mathring{A}$ (blue) of PdNi. The purple curve is the fit for low damping, pertaining only to the junction with 80 $\mathring{A}$ (purple markers), where the damping is calculated from the interpolation (full curve) of the measured (markers) quasiparticle resistance R_{qp}, Fig. 3.10. Above 2 K we cross into the regime of moderate damping, but σ is almost the same. The role of the thermal smearing is more important in the case of low damping, explaining this widening. The transition temperature between the two regimes is in accord with the junction parameters.

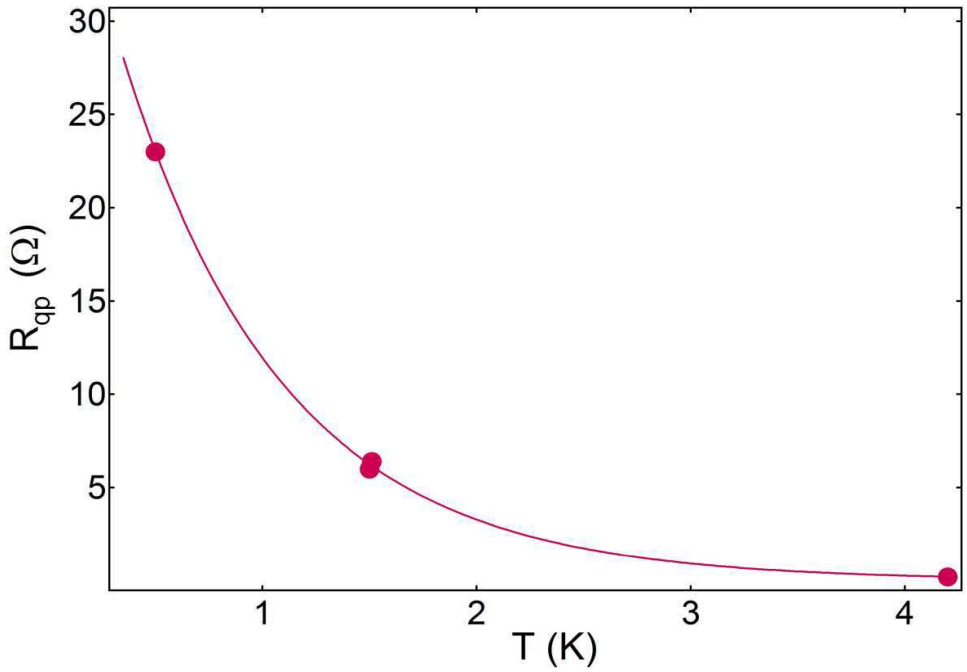

Figure 3.10: The measured quasiparticle resistance R_{qp} as function of temperature (markers), fitted with a double exponential $R_{qp}(\mathrm{T}) = 23\exp(-1.17\,\mathrm{T}) + 21\exp(-1.52\,\mathrm{T})$, for the junction with 100 $\mathring{A}$ of PdNi.

In Fig. 3.10 is shown the measured quasiparticle resistance on the junction with 100 $\mathring{A}$ of PdNi. We fit the quasiparticle resistance with a double exponential, obtaining $R_{qp}(\mathrm{T}) = 23\exp(-1.17\,\mathrm{T}) + 21\exp(-1.52\,\mathrm{T})$. For junction with 80 $\mathring{A}$ of PdNi, from IVs measured at low frequency, we also obtain the quasiparticle resistance of 24 Ω at low temperature, and we

expect it to decay in the similar way as function of temperature. We see that the damping is dominated by the quasiparticle resistance, setting the phase relaxation time.

Since one of the measured junctions is at the 0 – π transition and the other two in the π state, and they all scale as $\sigma/\langle I\rangle^{1/3}$, we conclude there is no additional noise coming from the phase fluctuations at the 0 – π transition. Also, the histogram width is as expected for non-ferromagnetic junctions, so there is no additional noise due to the ferromagnet. In fact, this is plausible, since the magnetic noise scales with volume and becomes difficult to detect in large surface junctions.

3.5 Non-adiabatic phase dynamics - dynamical bifurcation

The Josephson phase is seen within the RCSJ model as a nonlinear oscillator, forced by the periodic current bias. When the bias ramp frequency ν_b is comparable to the inverse damping time $\tau_\varphi^{-1} \sim (R_{qp}C)^{-1}$, the movement of the potential $U(\varphi)$ can no longer be considered as adiabatically slow compared to the phase movement. The nonlinear oscillator can enter into the bifurcation regime, meaning a small smooth change made to the parameter values or to the initial conditions of a system causes a sudden qualitative or topological change in its behavior. We see the bifurcation as jumps between the locked, non-dissipative state and the running, dissipative state. Bifurcation is a great tool to investigate the phase dynamics. We measure the bifurcation probability with the equivalent of a pump-probe measurement - we tilt the washboard potential fast, and then measure the evolution of the phase $\varphi(t)$ (more precisely, the voltage $V(t) \sim \dot{\varphi}(t)$).

The Kramers theory still applies, but in the phase space of meta-potential ($\dot{\varphi}$, φ)[85, 86, 87, 88, 102], meaning the activation rate

$$\Gamma = \frac{\omega_a}{2\pi} \exp\left(-\frac{\Delta U}{k_B T}\right) \tag{3.3}$$

does not describe the escape from one potential well to the other, but out of the attractor corresponding to a stable solution over a barrier ΔU. The attempt frequency ω_a and the potential barrier ΔU are also redefined, describing the movement in the phase space. The damping β does not play a role in the adiabatic switching for moderately underdamped junctions, while it does in the bifurcation escape rate. This activation rate is quite difficult to calculate for an underdamped junction, and we shall investigate bifurcation by solving Eq. (3.4) numerically.

In Fig. 3.11 we show the voltage as function of time (black curves) generated across the junction biased with a current sawtooth ramp (blue curve) for three different bias frequencies ω_b, obtained by the numerical solving of

$$\ddot{\varphi} + \beta\dot{\varphi} + \sin\varphi = 2\,\eta_b \left(\frac{\omega_b \tau}{2\pi} - \left[\frac{\omega_b \tau}{2\pi}\right]\right), \tag{3.4}$$

where $\beta = (R_{qp} C \omega_0)^{-1}$, $\eta_b = I_b/I_C$, $\omega_b = 2\pi\nu_b/\omega_0$, $\tau = \omega_0 t$, where ω_0 is the plasma frequency. The dot denotes $d/d\tau$, and brackets the round of a real number (closest integer smaller than the real number). Damping is $\beta = 1 \times 10^{-2}$ and the ramp frequency is, top to bottom $\omega_b = 1 \times 10^{-4}$, 1×10^{-3} and 3×10^{-3}. So first we have $\omega_b \ll \beta$ and all the switching is in equilibrium, then as ω_b approaches β from below, we see the second panel with two early switching events out of three, and as ω_b rises further, we see three early switching events out of three. So the early switching probability augments with the ramp frequency. There is a competition between the phase relaxation time and the ramp rise time. The early switching corresponds to the junction not relaxing into the locked state, but staying on the retrapping branch. We shall detail the numerical simulations in the next Section.

In Fig. 3.12 we show the measurement of the early switching probability as function of the

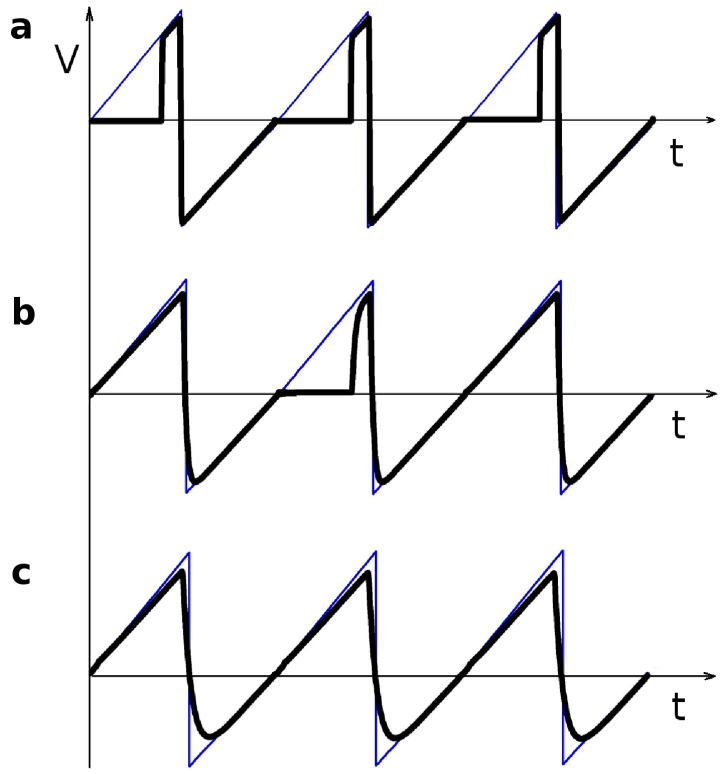

Figure 3.11: We show three possible scenarios obtained by numerical simulation, when varying the bias ramp frequency. We show voltage across the junction as function of time in black curves, and the sawtooth bias ramp in blue curves. The damping is $\beta = 1 \times 10^{-2}$ and the ramp frequency is, top to bottom $\omega_b = 1 \times 10^{-4}$, 1×10^{-3} and 3×10^{-3}, in units of plasma frequency. So first we have $\omega_b \ll \beta$ and all the switching is in equilibrium, then as ω_b approaches β from below, we see the second panel with two early switching events out of three, and as ω_b rises further, we see three early switching events out of three. The early switching probability rises with ramp frequency. The drive amplitude is $\eta_b = 1.25$ in units of critical current.

bias frequency. We bias the junction with 85 Å of PdNi with a ($V_b = 140$ mV, $R_b = 1$ kΩ) $I_b = 140\,\mu A$ current ramp in the frequency range between 4037 Hz and 20037 Hz. The Stanford SR560 amplifier bandpass is 1 Hz - 1 MHz. The measurement is taken at 300 mK. The sampling rate is 100 Ms/s. On the top panel the switching probability is measured for the ramp frequency $\nu_b = 4037$ Hz, showing one single histogram P_0. On the middle panel at $\nu_b = 6037$ Hz, we have a bimodal distribution with two histograms P_0 and P_1, where the additional histogram corresponds to the early switching. In the bottom panel, for $\nu_b = 12\,037$ Hz, we see the probability of early switching $N_1 = \int P_1(I)\,dI$ rise and $N_0 = \int P_0(I)\,dI$ decay.

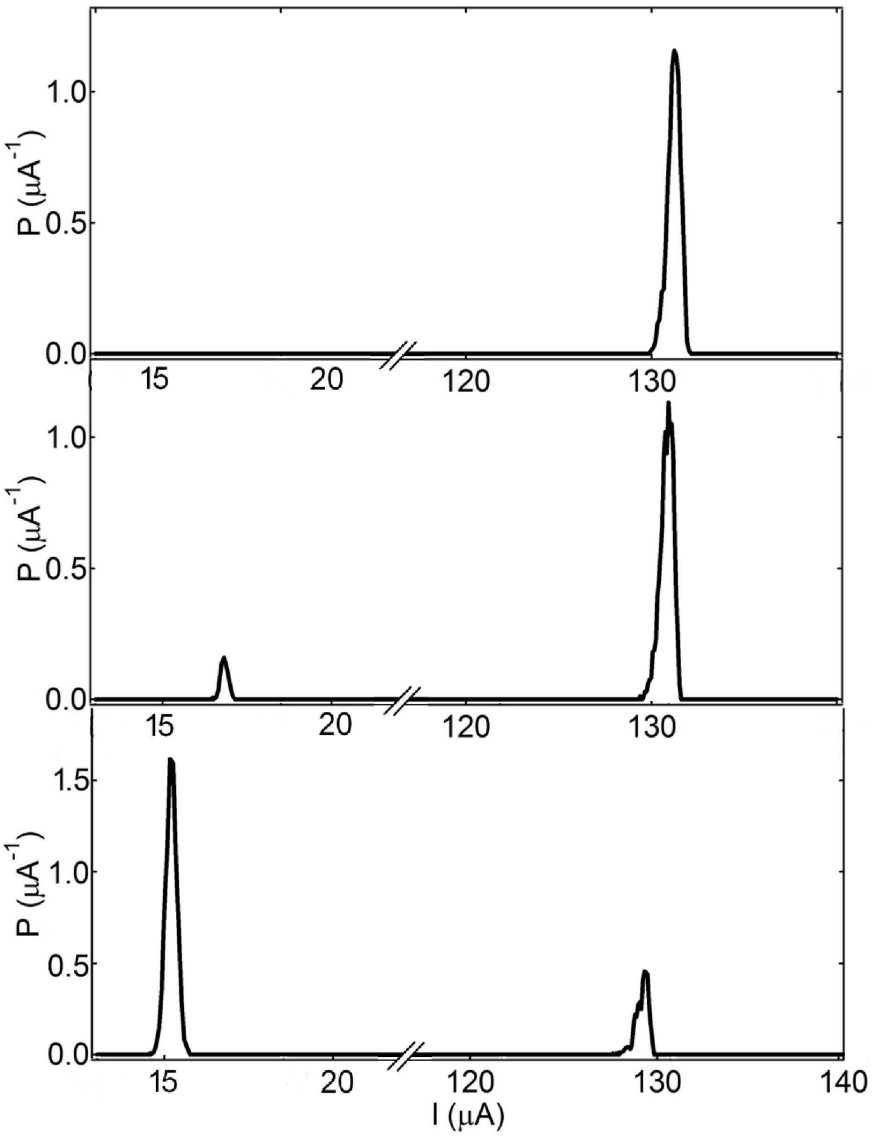

Figure 3.12: Switching histogram of the Nb/AlO/PdNi/Nb junction with 85 Å of PdNi taken at 300 mK with sweep frequency 4037 Hz (top panel), 6037 Hz (middle panel) and 12037 Hz (bottom panel).

The normalization yields $N_1 + N_0 = 1$. We have corrected the switching time for $3\,\mu s$ coming from the capacitance delay at the beginning of the ramp. This time is determined separately by taking the IV measurement, and it is frequency independent in this range. We expect the mean switching current $\langle I_S \rangle = (1/N_0) \int I P_0(I)\, dI$ to decrease as function of frequency, which is confirmed in the experiment. This does not apply to the early switching mean current

$\langle I_1 \rangle = (1/N_1) \int I P_1(I)\, dI$, where the trigger is not on the step but on the dissipative branch, therefore sensitive to the variations in the quasiparticle resistance R_{qp}. As we shall see later, in the ferromagnetic junctions we can have Fiske resonances (non-dissipative current at small but finite voltage) at zero external field which are seen on the dissipative branch, so by placing the trigger at higher voltage than the Fiske voltage we actually measure the Fiske current, rather than the retrapping current, which is the case for the measurement given in Fig. 3.12, where $\langle I_1 \rangle \sim 15\,\mu$A (Fiske current), while the retrapping current is estimated to be around 50 nA. However, this is a technical detail, brought on by the fact that the Fiske voltage is around 18 μV and it is easier to trigger above it. The probability of the early switching remains unchanged.

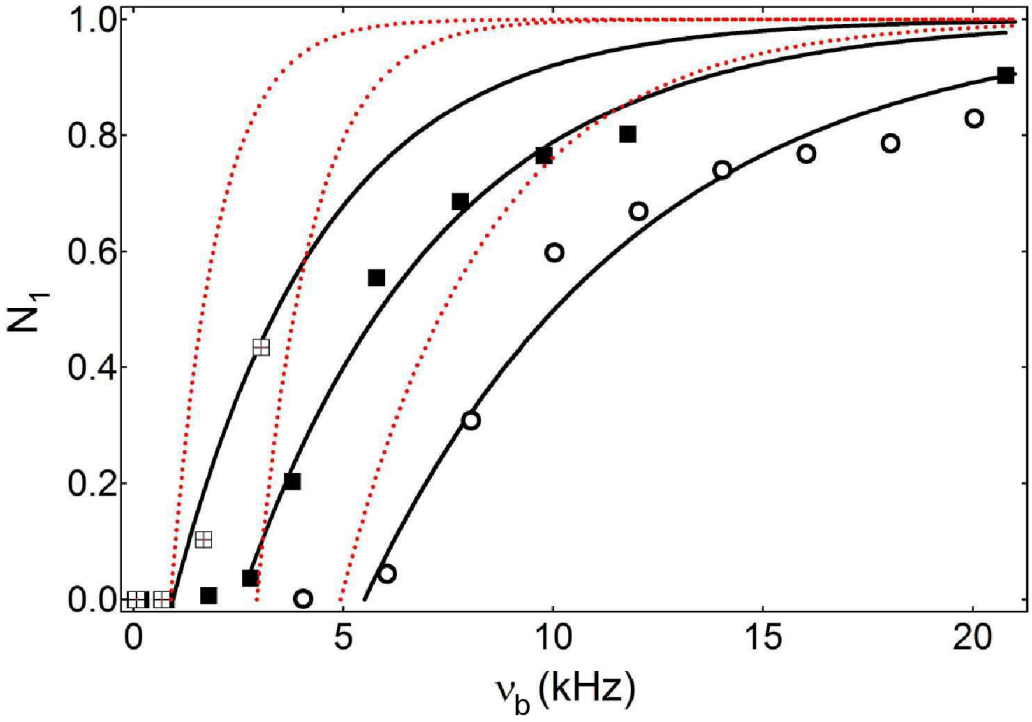

Figure 3.13: Early switching probability as function of the ramp frequency, measured at 300 mK for the Nb/AlO/PdNi/Nb junction with 85 Å (open circles), 100 Å (full squares) and 90 Å (crossed squares) of PdNi. The fit given in black curves assumes the early switching probability $N_1(\nu_b) = 1 - A\exp(-\tau_\varphi \nu_b)$, with τ_φ as the fitting parameter. The dashed red lines correspond to the theoretical prediction, obtained by numerically solving Eq. (3.9) to obtain τ_φ.

In Fig. 3.13 we show the probability of early switching N_1 as function of the ramp frequency. The measured values for three junctions are denoted by markers. We fit the experimental results with an exponential $N_1 = 1 - A\exp(-\tau_\varphi \nu_b)$, shown in black curves, obtaining the following fitting parameters. For the 85 Å junction (open circles, measured with bias amplitude η_b=1.18): $A = 2.32 \pm 0.3$ and the characteristic time is $\tau_\varphi = 153 \pm 20\,\mu s$. For the 100 Å junction (full squares, $\eta_b = 2$): $A = 1.69 \pm 0.15$ and $\tau_\varphi = 207 \pm 20\,\mu s$. For the 90 Å junction: $A = 1.3 \pm 0.3$ and $\tau_\varphi = 282 \pm 30\,\mu s$. The dashed lines are a predicted theoretical value, obtained by extrapolating the results of the numerical simulation detailed in the next Section, Eq. (3.9). With the numerical simulation we have calculated the time τ_φ.

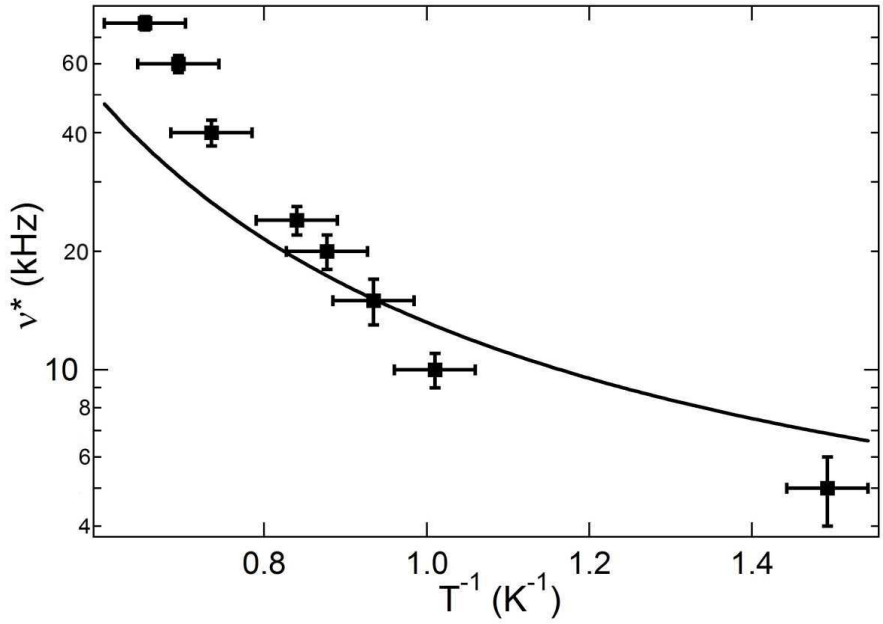

Figure 3.14: The measured dependence of the characteristic frequency ν^* for which the bifurcation sets in as function of temperature. The full line is an exponential fit taking into account the measured quasiparticle resistance, Fig. 3.10. The measurement is taken on the Nb/AlO/PdNi/Nb junction with 85 Å of PdNi.

In Fig. 3.14 we show the frequency ν^* at which bifurcation sets in as function of temperature T, measured on the junction with 85 Å of PdNi. Since the damping is $\beta = (R_{qp} C \omega_0)^{-1}$ and $R_{qp}(\mathrm{T}) = 23\exp(-1.17\,\mathrm{T}) + 21\exp(-1.52\,\mathrm{T})$, as obtained fitting the measured $R_{qp}(T)$, Fig. 3.10, we expect the double-exponential dependence of $\nu^*(T^{-1})$, which is confirmed in the

experiment. Here we directly establish the dependence of the phase relaxation time upon the quasiparticle resistance. The full expected dependence of $\nu^*(T)$ is obtained from $N_1(\nu^*) = 0$, yielding

$$\nu^* = \frac{\omega_0}{2\pi} \frac{\log A}{\mu \eta_b \left(C\omega_0\right)^{\frac{3}{2}}} R_{qp}^{-\frac{3}{2}}.$$

We treat A and μ as the fitting parameters, obtaining $\mu = 0.76$ and $A = 1.001$, which is in accord with the numerical simulations we shall detail in the following Chapter.

PdNi 56J						
Junction	a_{PdNi} (Å)	I_C (μA)	$\omega_0 = \sqrt{\frac{2eI_C}{\hbar C}}$ ($\times 10^9$ rad)	$\nu_0 = \frac{\omega_0}{2\pi}$ (MHz)	$\beta = \frac{1}{R_{qp} C \omega_0}$ ($\times 10^{-4}$)	$\eta = \frac{I_b}{I_C}$
56J, junction 5	85	130 (110)	3.0 (2.82)	474 (448)	3.3 (3.66)	1.18
55W, junction 5	100	67 (50)	2.2 (1.9)	350 (302)	2.78 (3.1)	1.5

Table 3.3: Parameters of measured junctions.

In Table 3.3 we summarize the properties of the two junctions we have measured in detail.

3.6 Numerical simulations of the bifurcation regime

We solve numerically the RCSJ model at zero temperature. The Josephson phase across the junction satisfies the second-order differential equation of a nonlinear driven oscillator

$$\ddot{\varphi} + \beta\dot{\varphi} + \sin\varphi = 2\,\eta_b \left(\frac{\omega_b \tau}{2\pi} - \left[\frac{\omega_b \tau}{2\pi} \right] \right), \tag{3.5}$$

where $\eta_b = I_b/I_C$, and the brackets [ ] denote the round of a real number (closest integer smaller than the real number). We are biasing with a sawtooth ramp, as used in the experiment. It corresponds to the movement of the Josephson phase in the tilted-washboard potential, with damping β, and forced by a sawtooth ramp of frequency ω_b and amplitude η_b. The time and all parameters are given in the units of plasma frequency ω_0, as explained in Section 1.3.1.

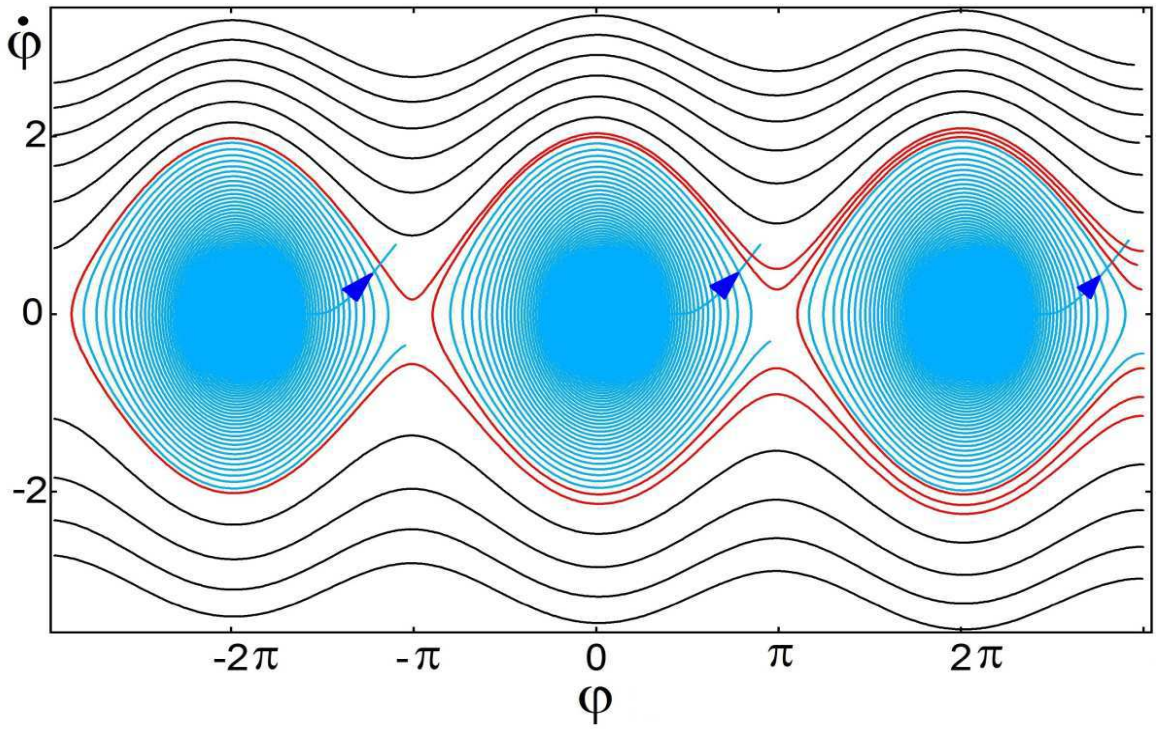

Figure 3.15: The phase diagram calculated for damping $\beta = 0.01$, ramp amplitude $\eta_b = 1.25$ and ramp frequency $\omega_b = 0.001$. The blue curves the are attractors, corresponding to the non-dissipative regime. The blue arrows are the instances of switching. The black curves correspond to dissipation, while the red curves correspond to the early switching events, where the phase approaches the attractor, but since it has sufficient kinetic energy, it does not retrap but stays in the dissipative regime. Red curves are very close to the separatrix, and they correspond to the retrapping branch in the IV characteristic.

Now let us detail the calculation procedure. The basis of the program is the numerical evaluation of Eq. (3.5), yielding the solutions $\varphi(\tau)$ and $\dot{\varphi}(\tau) \sim V(\tau)$, where $V(\tau)$ is the voltage across the junction, for given parameters β and η_b and ramp frequency $\nu_b = \omega_b\omega_0/2\pi$. Due to numerical limitations, we calculate one cycle at a time, feeding the solution $\varphi(2\pi)$ and $\dot{\varphi}(2\pi)$ as initial conditions $\varphi(0)$ and $\dot{\varphi}(0)$ into the following cycle. Since one period is $2\pi/\omega_b = \omega_0/\nu_b$, the ratio between the plasma frequency and the ramp frequency, the main numerical challenge is to address ramp frequencies much lower than the plasma frequency, as is the case in the experiment. Numerically we are able to obtain $\omega_b \sim 10^{-5}$, corresponding to ν_b =30 kHz, while the plasma frequency $\omega_0/2\pi \sim 500$ MHz, therefore we need to extrapolate

the numerical results by less than one order of magnitude to attain the experimental region. This is why we suppose that the probability of the early switching has the form $N_1 = 1-A\exp(-\tau_\varphi \nu_b)$, determine how τ_φ depends on parameters β and η_b by numerical simulations and then compare this calculated τ_φ to the one we are measuring.

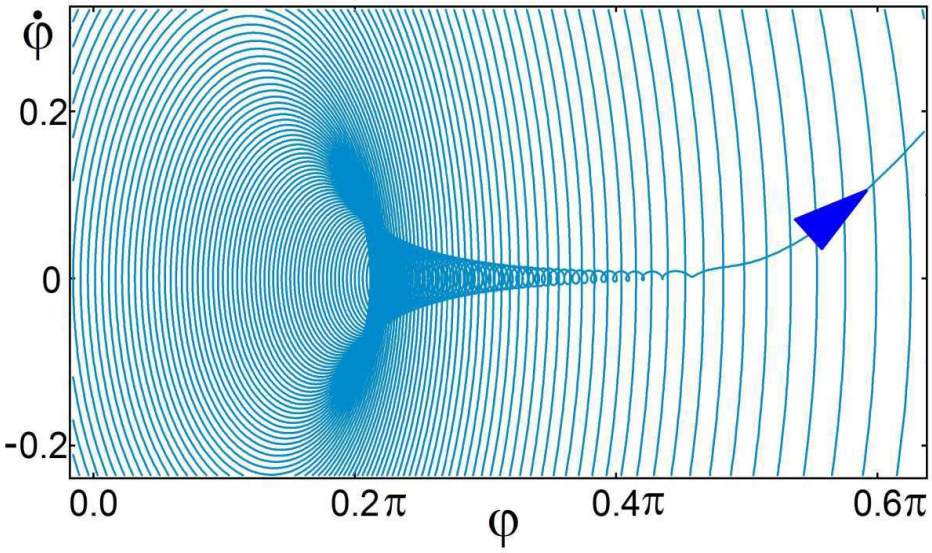

Figure 3.16: The core of the attractor. The arrow denotes the path corresponding to switching. The parameters are: $\beta = 0.01$, $\eta_b = 1.25$ and $\omega_b = 0.002$.

First we calculate the different types of solutions in the phase space (φ,$\dot{\varphi}$), Fig. 3.15. Non-dissipative regime corresponds to the attractors, shown in blue, where $\langle\dot{\varphi}\rangle = (2e/\hbar)V = 0$ over one period $T = 2\pi/\omega_0$. As the sawtooth ramp passes through zero, the particle falls into the attractor, staying there as the ramp mounts. Then the switching takes place, represented with blue arrows. The dissipative regime corresponds to the black curves, where $\langle\dot{\varphi}\rangle = (2e/\hbar)V \neq 0$. The red curves correspond to the events of the early switching, where the particle starts to fall into the attractor near zero, but since it has enough kinetic energy, it manages to stay out and go immediately into dissipation. The red curves are very close to the separatrix between the two regimes. Therefore the early switching current is equal to the retrapping current. In our case it is zero, due to very low damping. The phase diagram is obtained numerically for the following parameters: $\beta = 0.01$, $\eta_b = 1.25$ and $\omega_b = 0.001$.

The choice to represent $\varphi \in [-3\pi, 3\pi]$ is arbitrary and is made for clarity, since the diagram is obviously periodic in φ over 2π.

In Fig. 3.16 we show the core of an attractor, which clarifies how the switching takes place. As the ramp is tilted from 0 to 1, the local minimum of the potential $U(\varphi)$ is moved from 0 to $\pi/2$, which can be clearly seen in the Figure, since $\langle\varphi\rangle$ also moves from 0 to $\pi/2$, the particle making smaller and smaller oscillations in both φ and $\dot{\varphi}$. During this time, the mean voltage across the junction is zero. Then, the switching takes place and phase starts on the straight trajectory denoted by the arrow into the dissipative regime.

The Figs. 3.15 and 3.16 are slightly different from the phase diagrams in the strict sense of the word, since in a phase diagram all the lines are supposed to be for constant energy, t.i. for constant current bias. However, in the program we change the current bias adiabatically compared to all the other timescales, so it is a close approximation, and the phase trajectories are very close to the lines of constant energy. What would be constant energy concentric circles in the phase diagram, we see numerically as a spiral. The red lines in Fig. 3.15 are therefore not separatrices strictly speaking, but are sufficiently close to them. The phase diagram is symmetrical in 2π.

Now we shall clarify how exactly it is possible for a fast ramp to provoke bifurcation. As we have said, we calculate one period at a time, feeding the results $\varphi(0)$ and $\dot{\varphi}(0)$ as the initial conditions for the following cycle. So what makes the phase in one period stay on the critical current branch and in the other switch early? It is the kinetic energy the phase is getting from the ramp, which is then dissipated via damping. The ramp speed is crucial because for higher ramp speed there is not enough time for dissipation, and the phase enters the following cycle with higher kinetic energy. We numerically calculate the distribution of the initial conditions $\delta\varphi(0)$ and $\delta\dot{\varphi}(0)$ over a large number of cycles, Fig. 3.17. We find that $\delta\varphi(0)$ is always evenly distributed between $-\pi$ and π, regardless of the parameters. As for $\delta\dot{\varphi}(0)$, it is inversely proportional to $\eta_b\omega_b \sim \dot{\eta}$, the ramp speed, in the regime $\omega_b < \beta$,

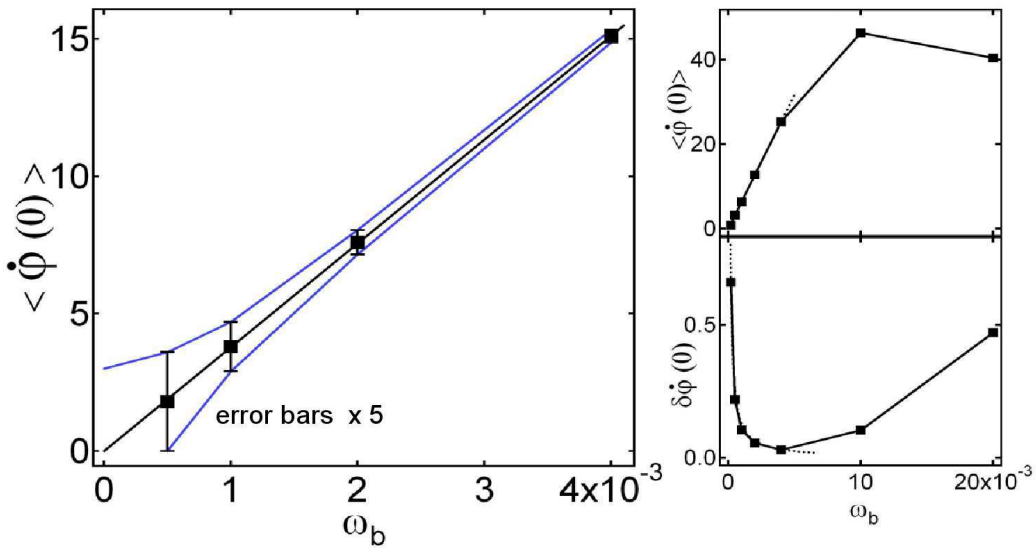

Figure 3.17: Left: Dependence of the mean initial speed of the Josephson particle $\dot{\varphi}(0)$ at the start of each cycle on the ramp frequency ω_b, with its dispersion, augmented 10 times for clarity. Right: Dependence of $\dot{\varphi}(0)$ (upper panel) and $\delta\dot{\varphi}(0)$ (bottom panel) on the ramp frequency ω_b in a wider range, for $\beta = 0.01$ and $\eta_b = 1.2$.

with a minimum at $\omega_b \sim \beta$, and for $\omega_b > \beta$ it is a rising function of $\dot{\eta}$. The minimum in $\delta\dot{\varphi}(0)$ is independent of the calculation accuracy. The mean $\langle\dot{\varphi}(0)\rangle$, on the other hand, is proportional to $\dot{\eta}$ over the whole range with a change of slope at $\omega_b \sim \beta$. When inspecting the core of the attractor, Fig. 3.16, we see by the level of detail in the solution that there is practically no numerical noise coming from the accuracy of calculation. Numerically we obtain bifurcation because at the end of each cycle the initial conditions for the following cycle are changed. But if we were to keep the initial conditions fixed entering each cycle, we would always get the exact same solution. In other words, at zero temperature bifurcation is deterministic.

We run the program for a given set of junction parameters, changing only the ramp frequency, and we obtain the solution $\dot{\varphi}(\tau) \sim V(\tau)$ already presented in Fig. 3.11 in the previous Section. For low ramp frequency, we get only one type of solution, while for higher ramp frequency we get two types of solution, corresponding to bifurcation. Our goal is to investigate the probability of obtaining the additional solution - the early switching prob-

ability N_1. We postulate that it depends on damping β, ramp amplitude η_b and the ramp frequency ω_b. In the following we will systematically keep one of the given parameters constant and investigate the dependence of N_1 on the second, with the third as independent variable, thus amounting to the empirical formula $N_1 = N_1(\beta, \eta_b, \omega_b)$. We know it should be in the form $N_1 = 1 - A\exp(f(\beta, \eta_b, \omega_b))$. In the following it is not important to keep track of all the fitting constants that come up, they will be shed once we arrive to the empirical formula. We proceed in three steps.

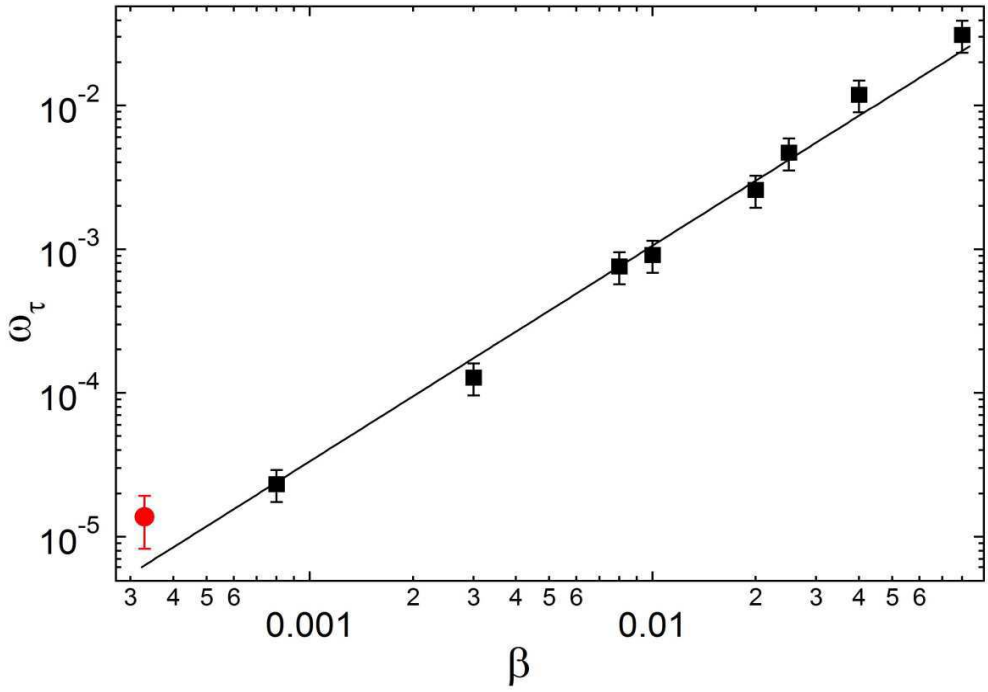

Figure 3.18: The early switching characteristic frequency $\omega_\tau \sim \tau_\varphi^{-1}$ as function of the damping β, when assuming the early switching probability in the form $N_1 = 1 - A\exp(-\omega_b/\omega_\tau)$. The black markers are the results of the numerical simulation, and the red marker is an experimental point (fitting parameter to data on Fig. 3.13, open circles). The full curve is an exponential fit $\omega_\tau = B_\tau * \beta^{3/2}$, with $\mathrm{B}_\tau = 1.06 \pm 0.1$.

First as function of the frequency ω_b, we calculate the probability of obtaining the early switching $N_1(\omega_b)$ for a given damping β, keeping the ramp amplitude η_b fixed, Fig. 3.18. We fit $N_1(\omega_b)$ as with an exponential $N_1 = 1 - A\exp(-\omega_b/\omega_\tau)$, as already shown in the previous Section for experimental results, and plot ω_τ as function of β in Fig. 3.13. Black markers

are numerical results, while the red marker is the experimental result, obtained as fitting parameter for the junction with 85 $\mathring{A}$ of PdNi (Fig. 3.13, open circles), the only measurement where the ramp frequency was roughly equal to that in the calculation, $\eta_b = 1.2$. We fit the numerical results with an exponential, $\omega_\tau = B_\tau * \beta^{3/2}$, with $B_\tau = 1.06 \pm 0.1$. Estimated ω_τ from the numerical simulation is 7.4×10^{-6}, while the measured value is 1.37×10^{-5} (for estimated damping of 3.3×10^{-4}). So, after first step, $N_1 \sim \beta^{-3/2}$.

We have so far $N_1 = 1 - A\exp(-\omega_b/B_\tau\beta^{3/2})$ for $\eta_b = 1.2$. In general it is

$$N_1 = 1 - A\exp\left[-f(\eta_b)\,\frac{\omega_b}{\beta^{\frac{3}{2}}}\right]. \tag{3.6}$$

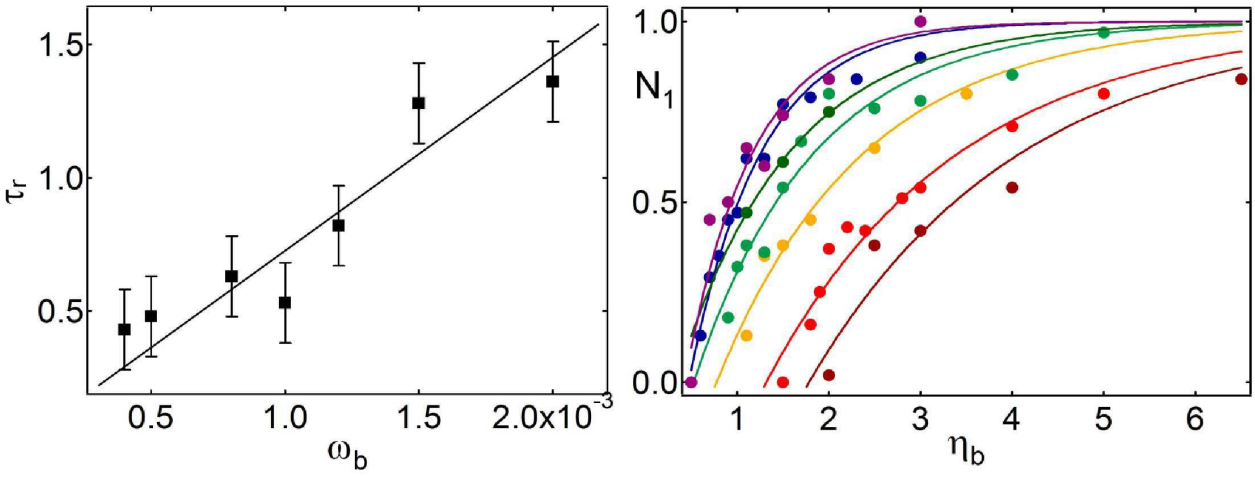

Figure 3.19: **Left**: Dependence of the characteristic time τ_r as function of the ramp frequency ω_b, for a fixed damping $\beta = 0.01$. **Right**: Dependence of the early switching probability N_1 on the ramp amplitude η_b, where each curve is given for a different value of the ramp frequency ω_b. The early switching probability is $N_1 = 1 - A\exp(-\eta_b\tau_r)$, where $\tau_r = \tau_r(\omega_b)$.

Now we keep the damping β fixed. First, on the right panel of Fig. 3.19, we investigate numerically the dependence of N_1 on the ramp amplitude η_b, varying ω_b from curve to curve. From left to right $\omega_b = 4 \times 10^{-4}$ up to $\omega_b = 2 \times 10^{-3}$. We fit each curve with an exponential $N_1 = 1 - A\exp(-\eta_b\tau_r)$, extracting τ_r for each ω_b. The data and the fit are the same color. In the left panel we show the obtained result. We are looking for a homogenous power

dependence, and here it is most likely linear, so we fit $\tau_r = B_r \omega_b$. The fitting parameter is $B_r = 725 \pm 45$. The damping is fixed throughout, $\beta = 0.01$. So, step two and three, $N_1 \sim \omega_b \eta_b$. Now we have established the second aspect of the empirical formula

$$N_1 = 1 - A \exp\left(-B_r(\beta)\, \omega_b\, \eta_b\right). \tag{3.7}$$

Now we put the two formulae, Eq. (3.6) and (3.7), together. Having started from a generic form $N_1 = 1 - A \exp(-\tilde{f}(\beta, \eta_b, \omega_b))$, and having established that $\tilde{f} \sim \beta^{-3/2}$, $\tilde{f} \sim \eta_b$ and $\tilde{f} \sim \omega_b$, we now have the complete empirical formula

$$N_1 = 1 - A \exp(-\frac{\mu\, \eta_b\, \omega_b}{\beta^{\frac{3}{2}}}), \tag{3.8}$$

where A and μ are constant. As it turns out, even if A and μ depend upon different parameters, this dependence is very slow. In the following we shall show that they can be taken as constant in the range we are interested in. We proceed to check the formula numerically and obtain the best values for A and μ by fitting.

Now we shall demonstrate this scaling. In Fig. 3.20 we plot N_1 as function of the reduced coordinate $\eta_b \omega_b / \beta^{3/2}$. All the curves are calculated by different procedures, keeping two parameters fixed and varying the third for each curve. We see that the scaling works rather well and we fit all of the curves with one single exponential. In order to determine the best fit, we fit each one, thus obtaining A and μ for each curve. We show these A and μ in Fig. 3.21. We see that although there is a certain distribution in A and μ, it is random and we can find a mean value to be $A = 1.8 \pm 0.1$ and $\mu = 0.76 \pm 0.04$. We can simplify the empirical formula further. The current bias $\eta(\tau)$ is linear in τ, it is $\eta = (1/\pi)\, \eta_b\, \omega_b\, \tau$, therefore $\eta_b \omega_b = \pi\, \dot{\eta}$.

Taking all this into account, the full and final empirical formula, obtained by the numerical fitting of the RCSJ model at zero temperature, is

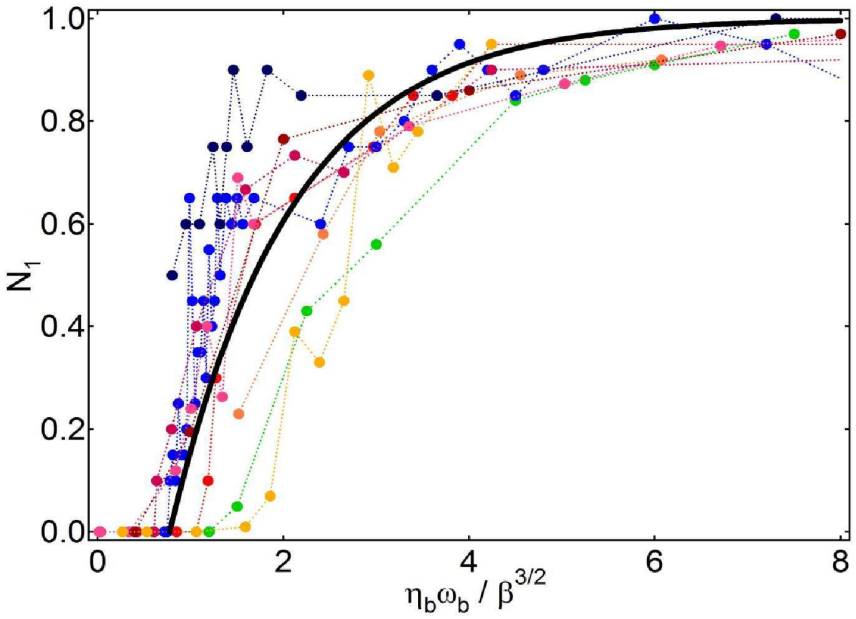

Figure 3.20: Numerical results of the early switching probability as function of the scaled variable $\eta_b\omega_b/\beta^{3/2}$ for values of β ranging from 8×10^{-4} to 8×10^{-2}, η ranging from 1 to 10, and ω_b ranging from 5×10^{-5} to 3×10^{-2}. The black curve is the best fit of all curves, $N_1 = 1 - A\exp(-\mu\,\eta_b\,\omega_b/\beta^{3/2})$, where $A = 1.8\pm0.2$ and $\mu = 0.76\pm0.04$.

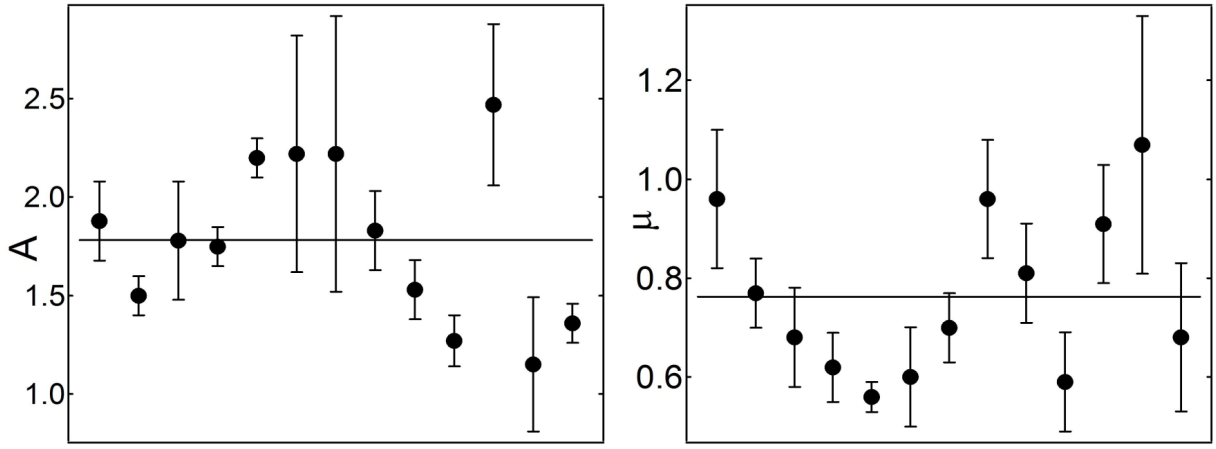

Figure 3.21: The values of universal constants A and μ in Eq. 3.8 for each numerically obtained curve on Fig. 3.20. The full lines are the best fit yielding $A = 1.8\pm0.1$ and $\mu = 0.76\pm0.04$.

$$N_1 = 1 - 1.8\,\exp(-0.76\,\pi\,\frac{\dot{\eta}}{\beta^{\frac{3}{2}}}). \tag{3.9}$$

This formula is valid in the range $\eta_b = 0$ – 10, $\omega_b = 10^{-5}$ – 10^{-1} and $\beta = 10^{-4}$ – 10^{-1} in units of the plasma frequency, and it is the central result of this Section. We need it because we are not able to solve the RCSJ model directly for the experimental junction parameters, where $\omega_b \sim 10^{-6}$ and $\beta \sim 10^{-5}$.

Now we can use the obtained numerical results to extrapolate to the experimental results on the three junctions shown in Fig. 3.13, for different values of damping and ramp amplitude, shown in Table 3.3. Coming back to the SI units, we have $N_1 = 1 - A\exp(-\mu\eta_b\omega_b/\beta^{3/2}) = 1 - A\exp(-\tau_\varphi[\mathrm{s}]\,\nu_\mathrm{b}[\mathrm{Hz}])$, yielding

$$\tau_\varphi = \frac{2\pi}{\omega_0}\frac{\mu\eta_b}{\beta^{\frac{3}{2}}}\,. \tag{3.10}$$

For the junction with 85 $\mathring{A}$ of PdNi we predict $\tau_\varphi = 283\,\mu$s, for 100 $\mathring{A}$ we predict $\tau_\varphi = 767\,\mu$s and for 90 $\mathring{A}$ we predict $\tau_\varphi = 905\,\mu$s. The curves corresponding to these relaxation times are show in Fig. 3.13 in red dotted curves, so we can make a direct comparison between the numerical and the experimental result. We see that we obtain the order of magnitude and the trend of rising relaxation time with rising quasiparticle resistance, but the calculated relaxation time is typically three times larger than the experimental. The numerical result is obtained for zero temperature, but when adding thermal smearing we would expect the relaxation time to rise, although not much, than to diminish.

In Fig. 3.22 we show the calculated frequency at which the bifurcation sets in, $\omega^* = 2\pi\nu^*/\omega_0$, as function of damping β. Here we keep the ramp amplitude fixed, $\eta_b = 1.2$. We expect the dependence

$$\omega^* = \beta^{\frac{3}{2}}\frac{\log A}{\mu\,\eta_b}.$$

We fit the numerical data with $\omega^* = A_2\beta^{3/2}$, and obtain $A_2 = 1.2$ for best fit, full black line. According to the empirical formula we should have $B^* = 1.92$, shown in dotted line. We can see however that the exponent $3/2$ might not be the best fit, but rather 1.8. The

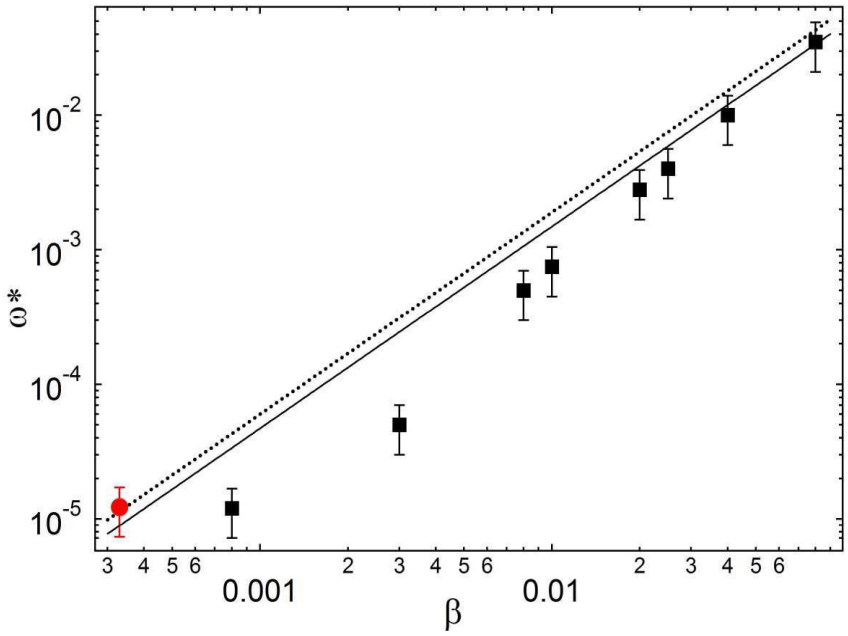

Figure 3.22: The characteristic frequency ω^* for which the bifurcation sets in, as function of the damping β. The black markers are the results of the numerical simulation, and the red marker is an experimental point. The full curve is a power fit $\omega^* = A_2 * \beta^{3/2}$, with $A_2 = 1.2 \pm 0.03$, while for the dotted curve $A = 1.92$, as predicted by the empirical formula. The experimental point is for the junction with 85 $\mathring{A}$ of PdNi.

red marker corresponds to the experimental result of junction with 85 $\mathring{A}$ of PdNi. When comparing Figs. 3.13 and 3.22, we see that they are fairly similar, and this is to be expected since in any exponential distribution roughly $\omega_\tau \sim \omega^*$.

Finally we shall briefly mention the influence of thermal noise on bifurcation. Coming back to the main equation, we add a thermal noise term as a current source in the usual manner

$$\ddot{\varphi} + \beta\dot{\varphi} + \sin\varphi = 2\,\eta_b \left(\frac{\omega_b \tau}{2\pi} - \left[\frac{\omega_b \tau}{2\pi} \right] \right) + f_n(\tau), \tag{3.11}$$

$$\langle f_n(\tau) f_n(\tau') \rangle = 2\beta\theta\delta(\tau - \tau'),$$

where $\theta = k_B T/U_C$, $U_C = (\hbar/2e)I_C$ being the Josephson energy. In our experiments $T = 300$ mK $\sim 25.8\,\mu$eV, and the Josephson energy is typically $U_C \sim 0.2$ eV for $I_C \sim 100\,\mu$A, therefore $\theta \sim 1.3 \times 10^{-4}$. The function $f(\tau)$ is the white noise correlator. More work is

needed to see numerically the influence of thermal noise on the bifurcation probability.

The bifurcation itself is deterministic. At zero temperature, the distribution of solutions is determined by the initial conditions, t.i. the initial position and, more importantly, kinetic energy. For one set of initial conditions we would always get the same sequence of solutions. At finite temperature, the sequence becomes stochastic, and we expect the switching probability to change somewhat due to the thermal fluctuations.

In this Section we have resolved numerically the equation governing the escape for ramp frequencies of the order of inverse damping time, we have shown that the bifurcation sets in, explained the dependence of bifurcation probability on the relevant parameters - ramp speed and damping, and made a correspondence with the experimental data.

3.7 Fiske steps in a ferromagnetic Josephson junction

Fiske resonance is a resonance between the Josephson current and the electromagnetic modes that propagate through the barrier as if it were a transmission line, and form standing waves with the junction's lateral size. The dispersion relation of the Fiske modes informs us on the propagation velocity of the electromagnetic waves through the ferromagnetic barrier. Just like the critical current, the Fiske step current shows a particular magnetic field dependence[96].

Our motivation is to find out if the Fiske resonances couple to the spin wave modes in the ferromagnetic Josephson junctions. In order to place the Fiske resonances in the GHz frequency range corresponding to the spin wave modes, we need the junctions of millimetric size. The junctions are the same as in the remainder of this Chapter. They consist of Nb (150 nm), Al (50nm), Al_2O_3, $Pd_{0.9}Ni_{0.1}$ ($0 - 10$ nm) and Nb (50 nm), with the surface of $0.6\,\text{mm} \times 0.8\,\text{mm}$.

The Fiske resonance condition is

$$V_n = \frac{\hbar}{2e}\,\omega_n = \frac{h}{2e}\frac{\bar{c}}{2L}\;n, \tag{3.12}$$

where V_n is the Josephson voltage, ω_n the corresponding Josephson frequency, $\bar{c}$ is the propagation of electromagnetic waves through the insulating/ferromagnetic barrier, L is the junction lateral size and n is an integer. The propagation speed $\bar{c}$ is

$$\bar{c} = \frac{1}{\sqrt{\mathcal{L}C}} = c\sqrt{\frac{a}{\varepsilon_r\, d}}\;, \tag{3.13}$$

where $\mathcal{L}$ is the barrier inductance per unit length, C is the capacitance per unit length, a is the barrier width, $d = a + 2\lambda$ is the magnetic length, λ is the superconducting penetration depth, ε_r the relative dielectric constant of the insulating barrier and c is the speed of light. The wave vector k_n of the $n-$th Fiske resonance is

$$k_n = \frac{n\pi}{L}\,. \tag{3.14}$$

Fiske resonances are measured as steps in the IV curve with an applied magnetic field. We apply an asymmetric current ramp. This is a standard method for measuring Fiske steps[92, 93]. The SIFS junction is with a 100 $\mathring{A}$ thick layer of ferromagnet $Pd_{0.9}Ni_{0.1}$. The measurement was taken at 300 mK. The junction was biased with a 52 μA asymmetric ramp with an offset of 26.7 μA. The current bias was imposed over a resistance of 1 kΩ, and with a frequency of 127 Hz.

In Fig. 3.23 we show Fiske resonances for a SIS junction (red curve) and for a SIFS junction (blue curve). We see that the first Fiske step for the SIS junction is at 10 μV, while for the SIFS junction the first step is shifted to the value of 18 μV. In Fig. 3.24 we show the in plane magnetic field dependence of the first Fiske step (dark blue markers) and the second Fiske step (light blue markers) for the ferromagnetic junction. By examining the field dependence of Fiske steps, we show unambiguously that the step at 18 μV is the first one. The dotted

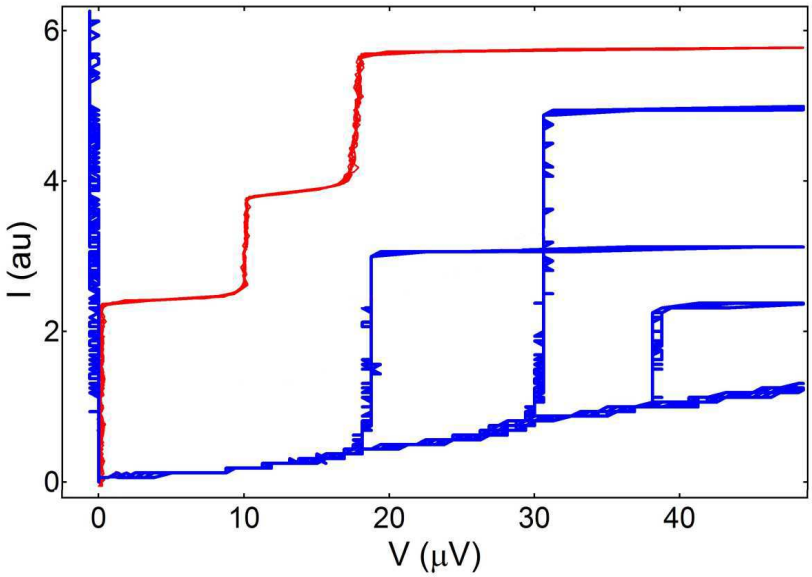

Figure 3.23: Fiske steps in the IV characteristics for an SIS junction (red curve) and for an SIFS junction (blue curve). The SIFS junction has a $Pd_{0.9}Ni_{0.1}$ layer of 100 $\mathring{A}$. The measurements is performed at T=300 mK. The field is applied in plane.

curve represents the dependence of the critical current on the applied in plane field.

Now we measure the Fiske resonance dispersion relation $\omega_n(n)$ for ferromagnetic junctions with various barrier thickness. We have available two wafers, and one of them also has two non-ferromagnetic junctions. In Fig. 3.25 we show the dispersion relation $\omega_n(n)$ for the SIS (pink markers) and the SIFS junctions (blue and grey markers corresponding to two different wafers, each shade/form to a separate junction). The pink line is a linear fit for the SIS junction $V_n = (\hbar/2e)\,\omega_n = (\hbar/2e)\,\bar{c}\,k_n = (\hbar/2e)\,n\,\pi\,\bar{c}/L$, yielding the propagation speed $\bar{c} = 0.022\,c$, where c is the speed of light in vacuum.

The Fiske steps give a possibility to estimate the junction capacitance. Since $\bar{c} = c\sqrt{a/\epsilon_r d}$, for $\bar{c} = 0.022\,c$, $a = 10$ $\mathring{A}$ and $\epsilon_r = 10$, we obtain $d = 189$ nm, which is not too bad, since on one side of the junction we have 50 nm of Nb, and on the other a bilayer of 50 nm of Al and 150 nm of Nb. We could determine d independently from the periodicity of the Fraunhofer pattern, Fig. 3.26, since $H_0 = \Phi_0/Ld$, where H_0 is the field corresponding to one

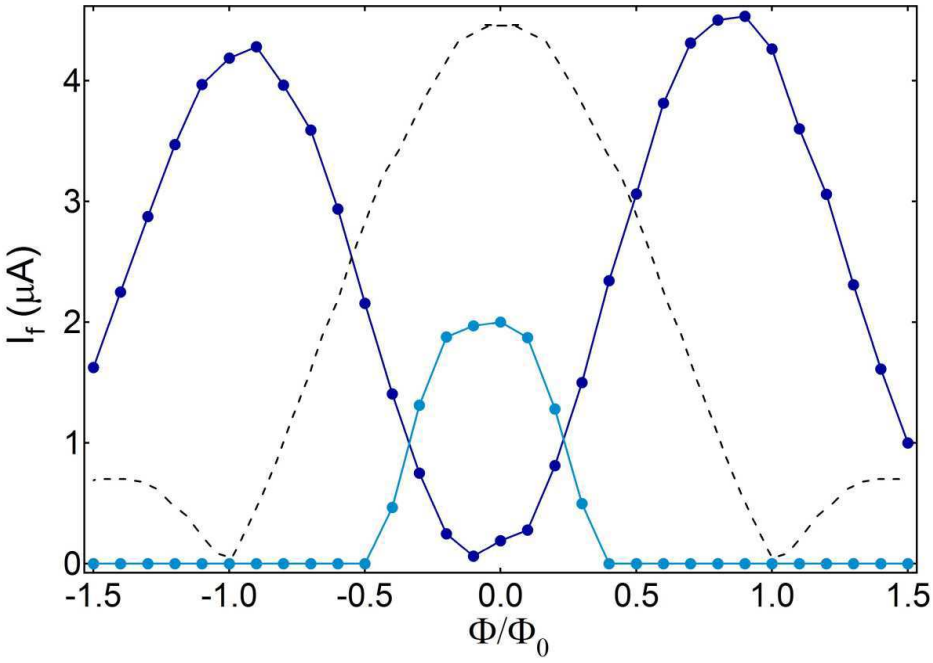

Figure 3.24: Dependence of the first (dark blue markers) and the second (light blue markers) Fiske step of the SIFS junction with 100 $\mathring{A}$ thick layer of ferromagnet $Pd_{0.9}Ni_{0.1}$ on the external magnetic field. The measurement is performed at T=300 mK. The field is applied in plane. The dotted black line is the Fraunhofer curve.

flux quantum Φ_0, but we did not measure the absolute value of the magnetic field. For the $d = 189$ nm and $L = 0.7$ mm we would obtain $H_0 = 150$ mG, which is reasonable. So the capacitance $C = 42$ nm calculated for $\epsilon_r = 10$, $L^2 = 0.49$ mm^2 and $a = 10\,\mathring{A}$ agrees with the Fiske resonances. We also have $\bar{c} = \omega_0 \lambda_J$, so the Josephson penetration depth is around 2 mm, which is four times larger than the junction lateral size.

For SIFS junctions we see that there is a shift in the dispersion relation, and the blue and grey lines are a linear fit. The change in the slope of the linear fit is wafer dependent, and it can come either from a different propagation speed or, more likely, somewhat different lateral size of the junction L. More work is needed to explain the shift in energy for ferromagnetic junctions with respect to the non-ferromagnetic ones. This is related to the dynamics of electromagnetic wave propagation through an insulator/ferromagnet bilayer.

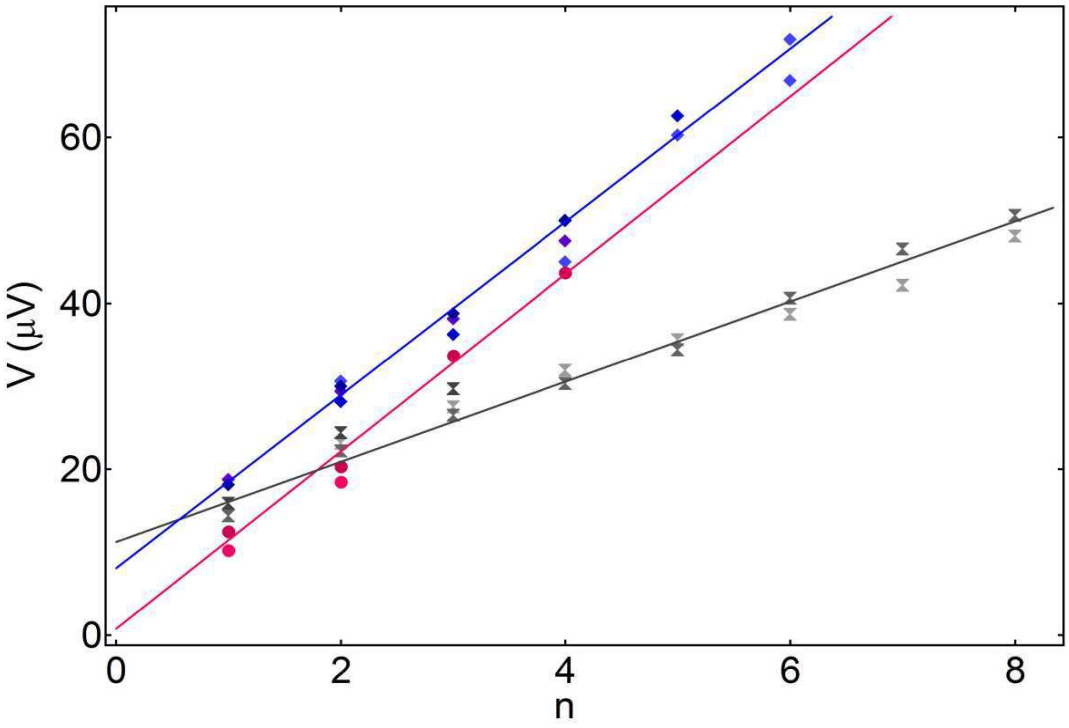

Figure 3.25: Dispersion relation or the SIS (red markers) and the SIFS junctions (blue and grey markers correspond to two different wafers, each shade/form to a separate junction). The red line is a linear fit for the SIS junction, blue and grey lines are a linear fit for SIFS junctions.

3.8 Fiske resonances measured via dynamical bifurcation

We come back to the measurement of the Fraunhofer pattern $I_C(H)$ in order to confirm the quality of the ferromagnetic Josephson junctions, see Fig. 3.26.

We fit the data assuming the uniform current distribution

$$I_C(H) = I_C(0) \left| \frac{\sin(\Phi/\Phi_0)}{\Phi/\Phi_0} \right|,$$

where $\Phi = H \cdot S$, H being the external magnetic field and $S = L \cdot d$ the junction (cross-section) surface. Of course, even though the junction is ferromagnetic, with 85 $\mathring{A}$ of PdNi, the shift of the Fraunhofer maximum similar to that seen for the smaller junctions is not visible,

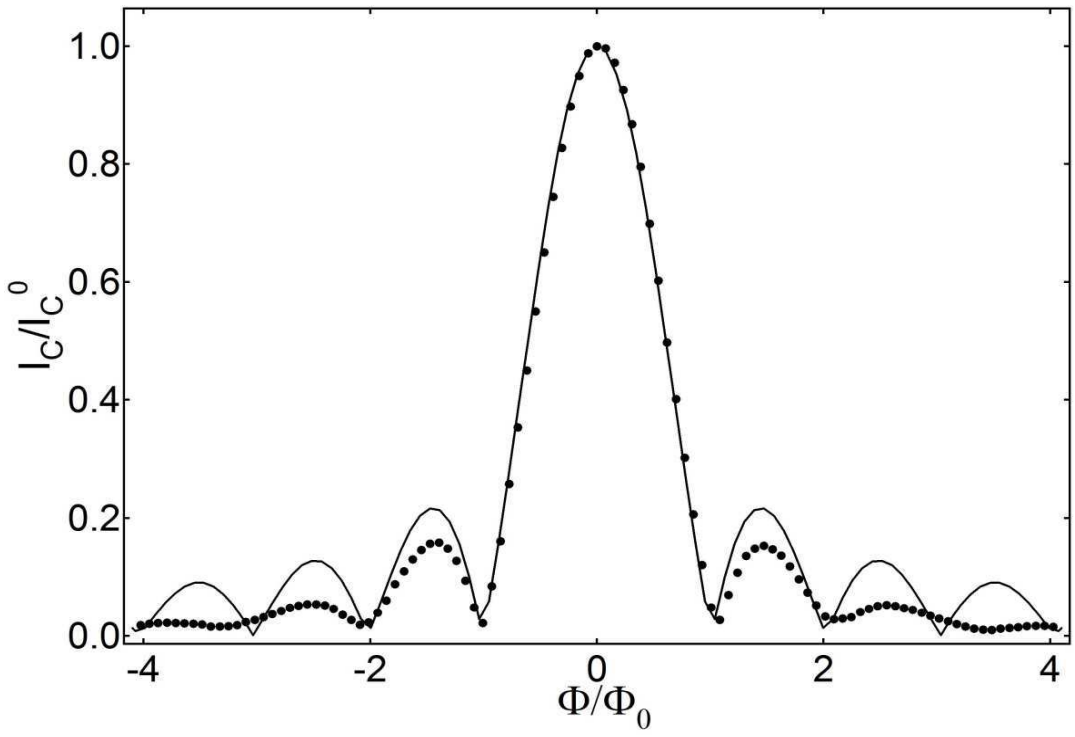

Figure 3.26: The Fraunhofer curve $I_C(H)$ for the junction with 85 $\mathring{A}$ of PdNi measured at 300 mK. The markers represent the data, while the full curve is the fit assuming uniform current distribution.

since $H_0 \sim \Phi_0/S \sim 10^{-4}$ Gauss is not comparable to the junction magnetization. Since the second minima are lower than predicted assuming the uniform current distribution, the fit could be improved by introducing a bell-shaped current distribution. We are reassured that the current flows through the junction in a homogenous way.

Returning to the question of bifurcation, we can ask what happens in the presence of an external field. We have the phase equation

$$\frac{\partial^2\varphi}{\partial\tau^2} + \beta\frac{\partial\varphi}{\partial\tau} + \sin\varphi - \frac{\bar{c}^2}{\omega_0^2}\frac{\partial^2\varphi}{\partial x^2} = 2\,\eta_b\left(\frac{\omega_b\tau}{2\pi} - \left[\frac{\omega_b\tau}{2\pi}\right]\right), \tag{3.15}$$

where $\bar{c}$ is the propagation speed of electromagnetic waves through the junction barrier. This is the driven sine-Gordon equation. We assume the solution in the form

$$\varphi = \varphi_0 + \omega\tau - kx,$$

where $\omega = (2e/\hbar)V$ and $k = (2ed/\hbar)H$. Due to the boundary conditions there is a quantization in frequency

$$\omega_n = \frac{2e}{\hbar}V_n = n\frac{\bar{c}}{2L}, \tag{3.16}$$

where L is the lateral size of the junction. These are the Fiske resonance frequencies. Also, for ferromagnetic junctions, we have seen that sometimes we can have Fiske steps in zero external field and that the dispersion relation is changed from Eq. (3.16).

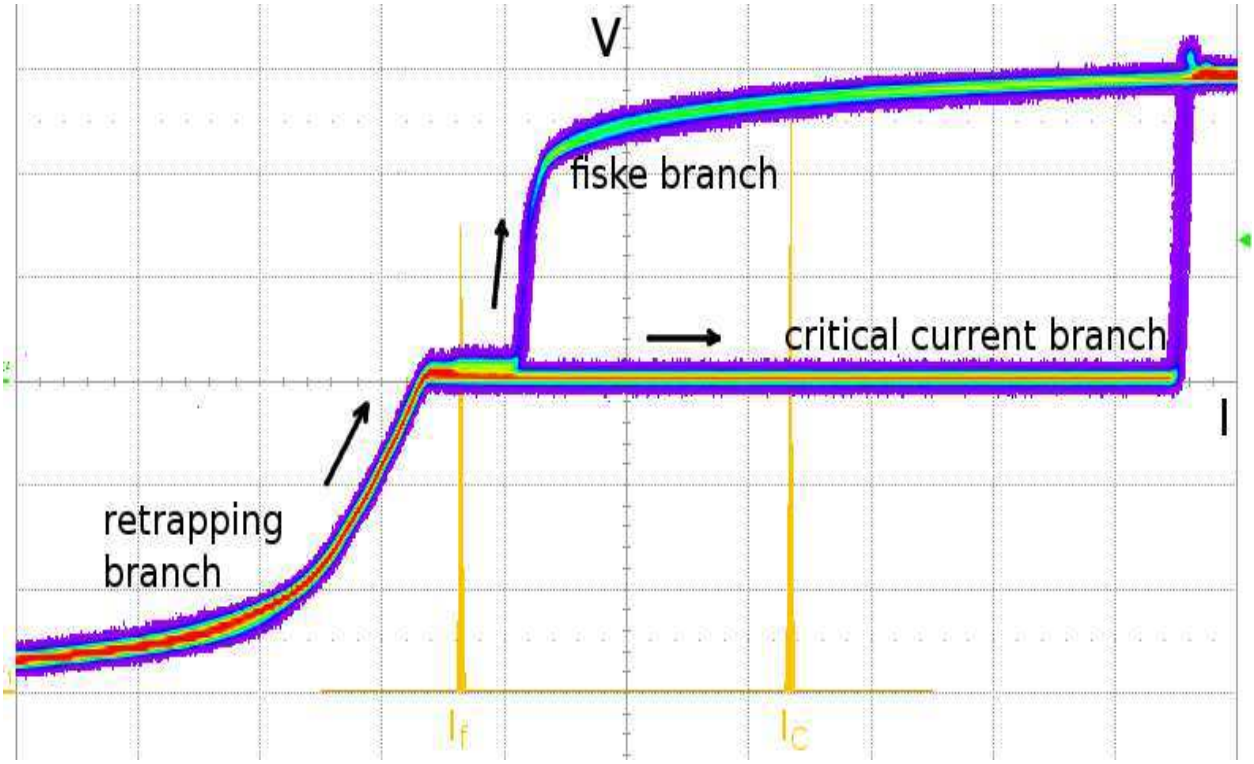

Figure 3.27: Photo taken with the oscilloscope of $V(I)$ for junction with 100 $\mathring{A}$ of PdNi, at 300 mK and with the bias frequency of 3037 Hz. The traces are accumulated over many cycles. We see the critical current branch and the Fiske branch. In the background in yellow are given the histograms of the appearance of two branches. Also it is important to note a small step on the Fiske branch corresponding to the Fiske voltage of 18 μV.

In Fig. 3.27 we see a photo taken with the oscilloscope of $V(I)$ for junction with 100 $\mathring{A}$ of PdNi, at 300 mK and with bias frequency of 3037 Hz. The traces are accumulated over many cycles. We see the critical current branch and the Fiske branch. In the background

in yellow are given the probability histograms of two branches, where the green flesh on the right edge of the graph shows the trigger level. Also it is important to note a small step on the Fiske branch corresponding to the Fiske voltage of 18 μV. We see that in the ferromagnetic Josephson junctions the bifurcation takes on a new form - the junction can either take the critical current branch, when the phase has enough time to relax to the bottom of the potential well, or it can take a Fiske/retrapping branch. With the appearance of the external field or a ferromagnetic layer inside the junction, the Fiske resonances become visible in the retrapping branch and can be probed with a suitable choice of trigger. We could also detect the retrapping current by placing the trigger under 18 μV.

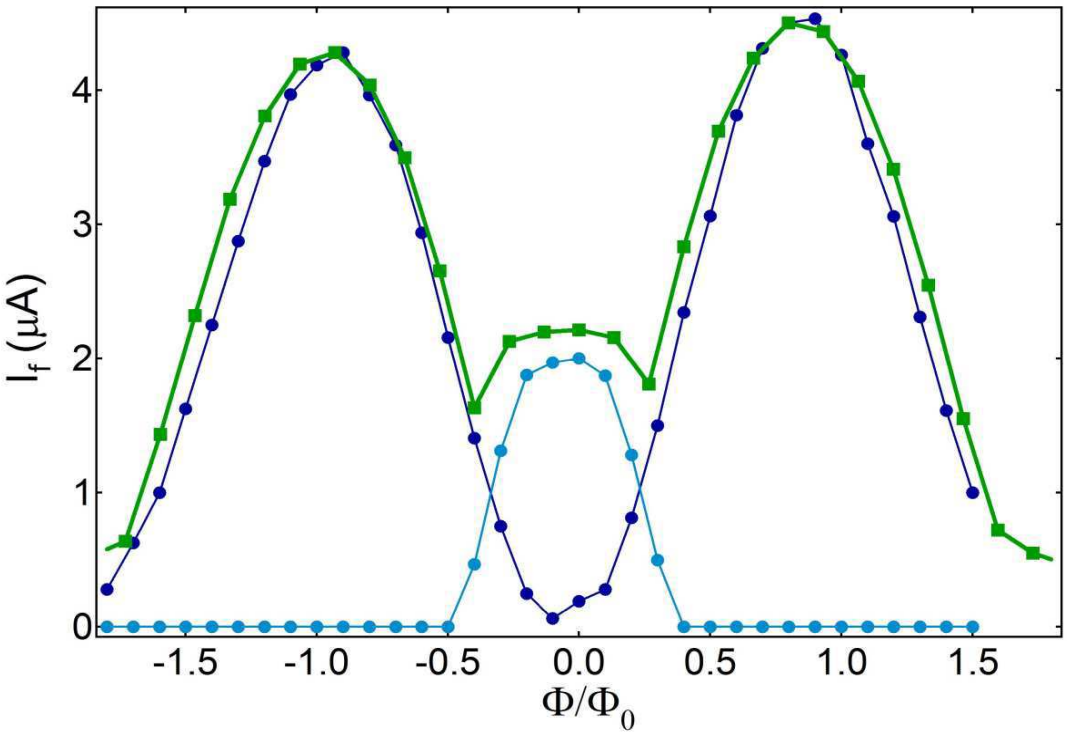

Figure 3.28: Comparison between the first (dark blue circles) and second (light blue circles) Fiske step taken at low frequency on the one side and the early switching current measured with bifurcation (green squares) on the other.

In Fig. 3.28 we compare the in plane field dependence of the early switching current (green squares) measured at high frequency with the Fiske steps taken in a traditional way at

low frequency (blue circles). The early switching current is measured at 300 mK with bias frequency of 3037 Hz. The Fiske steps were also taken at 300 mK at 37 Hz. The junction in question is with 100 $\mathring{A}$ of PdNi. Here we see how it works - with this particular choice of trigger, we probe as the bifurcation branch the first Fiske resonance, and then as the second Fiske resonance current becomes lower than the first, we probe the second. Bifurcation turns out to be a very elegant dynamical way to probe the Fiske resonances[103].

Chapter 4

Conclusion and perspectives

The coupling between the superconducting and magnetic order parameters is the principal subject of this work.

We have demonstrated for the first time the resonant coupling between the spin-wave modes and the Josephson current in the ferromagnetic Josephson junctions. The coupling is a manifestation of the Aharonov-Bohm effect, that is a coupling via the vector potential **A**. This shows that we are able to perform an analog of the ferromagnetic resonance measurement using the unique features of the Josephson junction. The Josephson junction on the one hand excites the spin modes, and on the other resonantly couples to them, and therefore serves as detector. The advantage of this setup is that the ferromagnetic layer inside the Josephson junction is very small, with the magnetic moment of $10^7\,\mu_B$, not accessible with standard ferromagnetic resonance techniques. We have used a weak ferromagnet, PdNi with 10 % Ni and a Curie temperature of 130 K. A stronger ferromagnet would have suppressed the Josephson current, making detection impossible. We have also performed an independent standard resonant cavity experiment on a layer with the same cross-section but with a macroscopic surface and established a correspondence between the spectra. We have also, by applying external rf radiation, shown that the ferromagnetic modes couple to the Josephson current.

We can use the sensitivity of the Josephson effect to study in detail other ferromagnetic modes, such as domain wall movement. Another possibility is the study of nonlocal transport, where by suitable junction geometry a Cooper pair would be forced to pass through

different magnetic domains. This opens up the experimental investigation of the exciting question of interplay between spin-polarized and superconducting transport, especially in the case of the triplet pairing.

Another part of the thesis is dedicated to the study of proper phase dynamics in the non-stationary regime. We have performed an analogue of the pump-probe measurement, biasing the Josephson junction with a fast ramp and then investigating the phase relaxation by measuring the switching into the dissipative state. We found that when the ramp period is comparable to the phase relaxation time $R_{qp}C$, governed by the quasiparticle resistance, the junction enters the bifurcation regime. With a certain probability the phase relaxes to the bottom of the tilted washboard potential well, and with a certain probability it stays near the top, going directly out and into the dissipative state. For the ferromagnetic junctions we find that instead of the retrapping branch, the phase follows the branch of a Fiske resonance. This is again due to the sensitivity of the phase to the total magnetic field. Bifurcation is a new way to probe the phase relaxation directly in different regimes.

Appendix

Fabrication Recipes for small Nb/PdNi/Nb junctions

Mask Fabrication

Deposition of resist trilayer on the silicon wafer with oxidized surface

1) **500 nm of PES**

Bake wafer beforehand

Make 18% solution of PES from PES flakes and NMP

Spin the PES for 315 s, ramp rise time 9 s, 2300 rpm

Spin in nitrogen atmosphere

Bake the PES for 2 minutes at 250°

Resulting thickness: 600-800 nm.

2) **60 nm of Si_3N_4**

Deposit the mixture of SiH_4 and NH_3 in RIE chamber

Time 2 min 30 s

Temperature 200°

rf power 60 Watt

Resulting thickness: 60 nm

3) **350-400 nm of PMMA**

Deposit A3 solution of PMMA

Spin the PMMA for 60 s, ramp rise time 5 s, 2000 rpm

Bake the PMMA for 3-4 minutes at 160°

Resulting thickness: 350-400 nm.

Lithography

We design the mask in NPGS

The lithography is performed with a SEM

The motive is developed in the MIBK-IPA 3:1 solution for 2 minutes

Reactive Ion Etching

Two-step etching process

1) **Etch with SF_6**

Time 1 min 30 sec

Pressure 30 mTorr

Observe the etching with a laser interferometer and optical microscope

2) **Etch with O_2**

Time 10 min

Pressure 300 mTorr

High pressure is crucial for obtaining the undercut

Expected result: 500 nm of undercut.

Evaporation

Three-step evaporation

1) **Nb**

Pressure $6 \cdot 10^{-8}$ mbar

Rate 5.5 $\mathring{A}/s$

Layer thickness 507 $\mathring{A}$

2) **Oxidation of Nb**

Pressure 10 mbar

Time 10 min

3) **PdNi**

Pressure $8 \cdot 10^{-9}$ mbar Rate 1.1 $\mathring{A}/s$

Layer thickness 207 $\mathring{A}$

4) **Nb**

Pressure $8 \cdot 10^{-8}$ mbar

Rate 4.5 $\mathring{A}/s$

Layer thickness 511 $\mathring{A}$

Mask liftoff: 10 min in NMP solution.

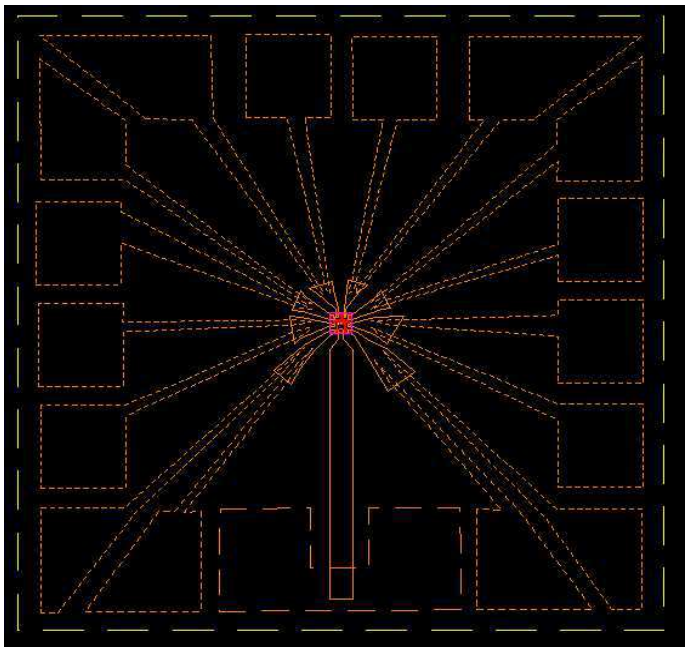

Figure 4.1: Mask designed with NPGS software.

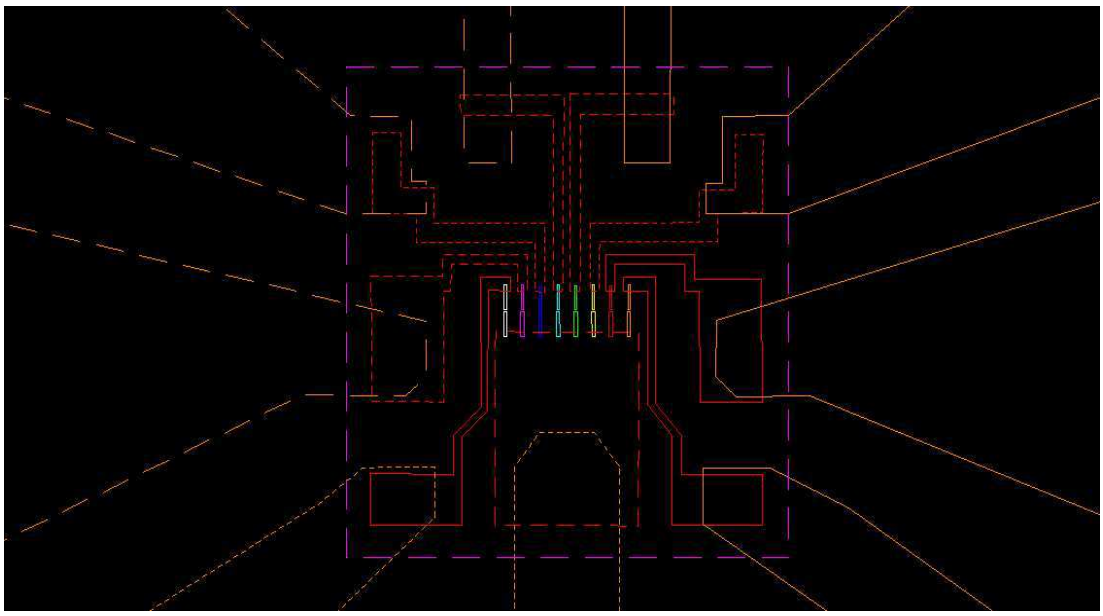

Figure 4.2: Inset of the mask designed with NPGS software, showing 8 junction-masks in parallel.

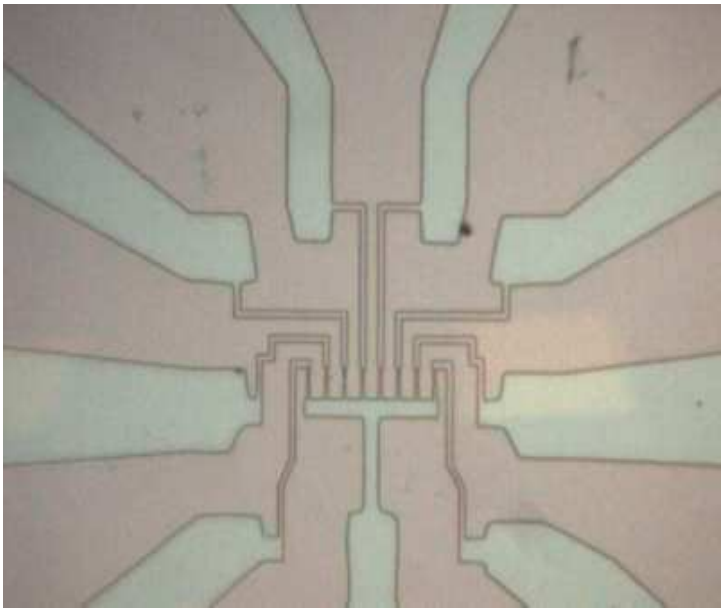

Figure 4.3: Typical fabricated mask.

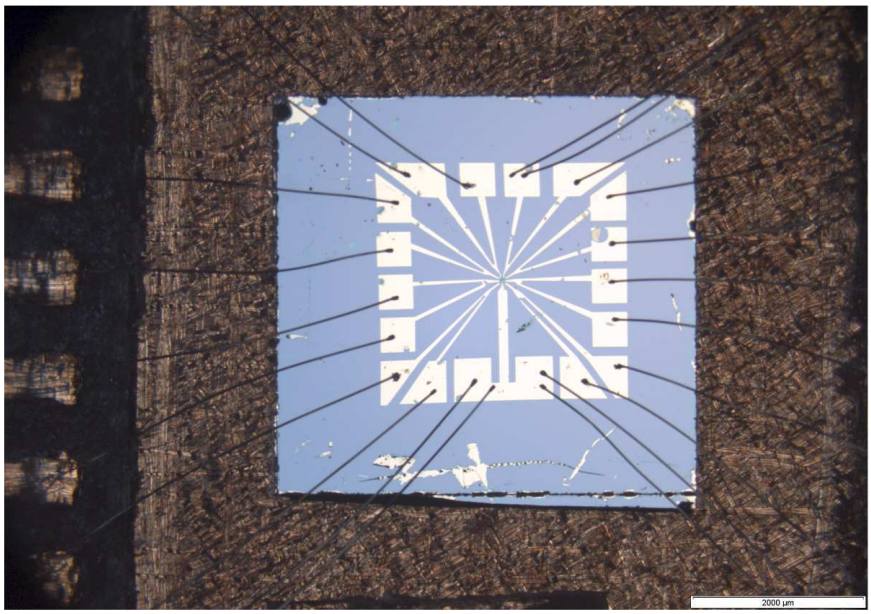

Figure 4.4: Typical fabricated sample glued to the sample holder and with bonded contacts.

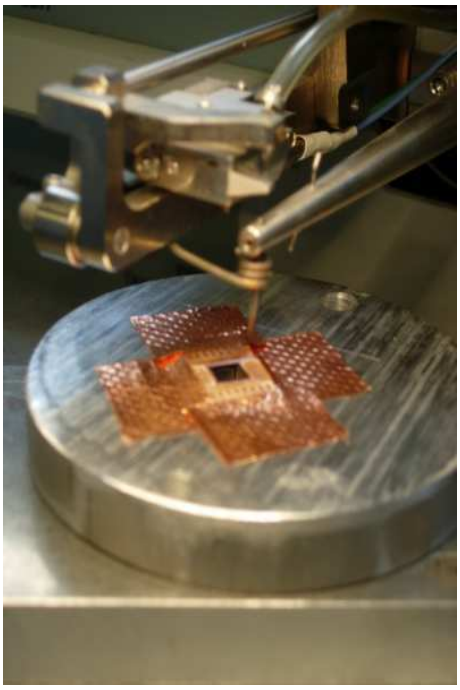

Figure 4.5: Bonding the sample contacts to the sample holder with the ultrasound soldering machine.

Figure 4.6: The top of the dilution refrigerator probe.

Figure 4.7: Photo of the 35 mK dilution refrigerator.

References

[1] H. Kamerlingh Onnes, Leiden Commun. **122**, 124 (1911).

[2] J. Bardeen, L. N. Cooper, and J. R. Schrieffer, Phys. Rev. **108**, 1175 (1957).

[3] V. L. Ginzburg and L. D. Landau, Zh. Eksperim. i Teor. Fiz. **20**, 1064 (1950).

[4] L. N. Cooper, Phys. Rev. **104**, 1189 (1956).

[5] D. Saint-James, D. Sarma, and E. J. Thomas, *Type II Superconductivity* (Pergamon, New York, 1969).

[6] V. L. Ginzburg, Zh. Eksp. Teor. Fiz. **31**, 202 (1956) [Sov. Phys. JETP **4**, 153 (1957)].

[7] W. Meissner and R. Ochsenfeld, Naturwissenschaften **21**, 787 (1933).

[8] P. Fulde and R. A. Ferrell, Phys. Rev. **135**, A550 (1964).

[9] A. I. Larkin and Y. N. Ovchinnikov, Zh. Eksp. Teor. Fiz. **47**, 1136 (1964) [Sov. Phys. JETP **20**, 762 (1965)].

[10] A. I. Buzdin, Rev. Mod. Phys. **77**, 935 (2005).

[11] H. K. Wong, B. Y. Jin, H. Q. Yang, J. B. Ketterson, and J. E. Hilliard, J. Low Temp. Phys. **63**, 307 (1986).

[12] Z. Radović, M. Ledvij, L. Dobrosaljević-Grujić, A. I. Buzdin, and J. R. Clem, Phys. Rev. B **44**, 759 (1991).

[13] J. S. Jiang, D. Davidović, D. H. Reich, and C. L. Chien, Phys. Rev. Lett. **74**, 314 (1995)

[14] I. F. Lyuksyutov and V. L. Pokrovsky, Advances in Physics **54**, 67 (2005).

[15] S. S. Saxena, *et al.,* Nature London **406**, 587 (2000).

[16] D. Aoki, *et al.,* Nature London **413**, 613 (2001).

[17] P. G. de Gennes, *Superconductivity of Metals and Alloys* (Benjamin, New York, 1966).

[18] F. S. Bergeret, A. F. Volkov, and K. B. Efetov, Rev. Mod. Phys. **77**, 1321 (2005).

[19] M. Tinkham, *Introduction to Superconductivity* (2nd ed., New York, McGraw-Hill, 1995).

[20] A. F. Andreev, Zh. Eksp. Teor. Fiz. **46**, 1823 (1964) [Sov. Phys. JETP **19**, 1228 (1964)].

[21] G. E. Blonder, M. Tinkham, and T. M. Klapwijk, Phys. Rev. B **25**, 4515 (1982).

[22] R. J. Soulen, Jr., *et al.*, Science **282**, 85 (1998).

[23] M. J. M. de Jong and C. W. J. Beenakker, Phys. Rev. Lett. **74**, 1657 (1995).

[24] B. D. Josephson, Physics Letters **1**, 251 (1962).

[25] B. D. Josephson, Adv. Phys. **14**, 419 (1965).

[26] B. D. Josephson, Rev. Mod. Phys. **36**, 216 (1964).

[27] S. Shapiro, Phys. Rev. Lett. **11**, 80 (1963).

[28] P. W. Anderson and J. M. Rowell, Phys. Rev. Lett. **10**, 230 (1963).

[29] J. M. Rowell, Phys. Rev. Lett. **11**, 200 (1963).

[30] R. C. Jaklevic, John Lambe, A. H. Silver, and J. E. Mercereau, Phys. Rev. Lett. **12**, 159 (1964).

[31] A. H. Silver and J. E. Zimmerman, Phys. Rev. Lett. **15**, 888 (1965).

[32] A. O. Caldeira and A. J. Leggett, Phys. Rev. Lett. **46**, 211 (1981).

[33] A. J. Leggett and Anupam Garg, Phys. Rev. Lett. **54**, 857 (1985).

[34] T. P. Orlando, J. E. Mooij, Lin Tian, Caspar H. van der Wal, L. S. Levitov, Seth Lloyd, and J. J. Mazo, Phys. Rev. B **60**, 15398 (1999).

[35] Y. Nakamura, C. D. Chen, and J. S. Tsai, Phys. Rev. Lett. **79**, 2328 (1997).

[36] Yu. Makhlin, G. Schon, and A. Shnirman, Rev. Mod. Phys. **73**, 357 (2001).

[37] I.O. Kulik, Zh. Eksp. Teor. Fiz. **49**, 585 (1966) [Sov. Phys. JETP **22**, 841 (1966)].

[38] L. N. Bulaevskii, V. V. Kuzii, and A. A. Sobyanin, Pisma Zh. Eksp. Teor. Fiz. **25**, 314 (1977) [JETP Lett. **25**, 290 (1977)].

[39] V. V. Ryazanov *et al.*, Phys. Rev. Lett. **86**, 2427 (2001).

[40] T. Kontos, *et al.,* Phys. Rev. Lett. **89**, 137007 (2002).

[41] J. J. A. Baselmans, *et al.*, Nature London **397**, 43 (1999).

[42] Z. Radović, N. Lazarides, and N. Flytzanis, Phys. Rev. B **68**, 014501 (2003).

[43] I. Petković, N. M. Chtchelkatchev, and Z. Radović, Phys. Rev. B **73**, 184510 (2006).

[44] D. J. van Harlingen, Rev. Mod. Phys. **67**, 515 (1995).

[45] A. A. Golubov, M. Yu. Kupriyanov, and E. Il'ichev, Rev. Mod. Phys. **76**, 411 (2004).

[46] A. Bauer, J. Bentner, M. Aprili, M. L. Della Rocca, M. Reinwald, W.Wegscheider, and C. Strunk, Phys. Rev. Lett. **92**, 217001 (2004).

[47] Z. Radović, Lj. Dobrosavljević-Grujić, and B. Vujičić, Phys. Rev. B **63**, 214512 (2001).

[48] S. M. Frolov, *et al.*, Nature Physics **4**, 32 (2008).

[49] G. Deutscher and D. Feinberg, Appl. Phys. Lett. **76**, 487 (2000).

[50] D. Beckmann, H. B. Weber, and H. v. Löhneysen, Phys. Rev. Lett. **93**, 197003 (2004).

[51] S. Russo, M. Kroug, T. M. Klapwijk, and A. F. Morpurgo, Phys. Rev. Lett. **95**, 027002 (2005).

[52] Y. Aharonov and D. Bohm, Phys. Rev. **115**, 485 (1959).

[53] T. A. Fulton and L. N. Dunkelberger, Phys. Rev. B **9**, 4760 (1974).

[54] D. E. McCumber, J. Appl. Phys. **39**, 3113 (1968).

[55] W. C. Stewart, Appl. Phys. Lett. **12**, 277 (1968).

[56] K. K. Likharev, *Dynamics of Josephson Junctions and Circuits* (Gordon and Breach, New York, 1986).

[57] I. Petković, M. Aprili, S. E. Barnes, F. Beuneu, and S. Maekawa, *submitted to Phys. Rev. Lett.*

[58] A. M. Goldman, C. G. Kuper, and O. T. Valls, Phys. Rev. Lett. **52**, 1340 (1984).

[59] S. E. Barnes, J. Phys. C **10**, 2863, (1977).

[60] K. Baberschke, K. D. Bures, and S. E. Barnes, Phys. Rev. Lett. **53**, 98 (1984).

[61] S. E. Barnes and F. Mehran, Phys. Rev. B **34**, 4537 (1986).

[62] F. Mehran, S. E. Barnes, C. C. Chi, R. L. Sandstrom, and C. P. Umbach, Phys. Rev. B **36**, 7281 (1987).

[63] Z. Nussinov, A. Shnirman, D. P. Arovas, A. V. Balatsky, and J.-X. Zhu, Phys. Rev. B **71**, 214520 (2005).

[64] J.-X. Zhu, Z. Nussinov, A. Shnirman, and A. V. Balatsky, Phys. Rev. Lett. **92**, 107001 (2004).

[65] A. V. Balatsky, J. Fransson, D. Mozyrsky, and Y. Manassen, Phys. Rev. B **73**, 184429 (2006).

[66] L. Bulaevskii, M. Hruška, A. Shnirman, D. Smith, and Yu. Makhlin, Phys. Rev. Lett. **92**, 177001 (2004).

[67] C. P. Slichter, *Principles of Magnetic Resonance* (Springer-Verlag, New York, 1990).

[68] B. Hildebrands, A. Thiaville (Eds.), *Spin Dynamics in Confined Magnetic Structures III* (Topics in Applied Physics, Springer, 2006).

[69] J. C. Gonzalez-Pons, J. J. Henderson, E. del Barco, and B. Ozyilmaz, Phys. Rev. B **78**, 012408 (2008).

[70] M. Ramesh and P. E. Wigen, J. Magn. Magn. Mater. **74**, 123 (1988).

[71] R. P. Feynman, R. B. Leighton, and M. Sands, *The Feynman Lectures on Physics, Quantum Mechanics, 3* (Reading, Massachusetts, Addison-Wesley Publishing, 1963).

[72] H. A. Kramers, Physica **7**, 284 (1940).

[73] A. Garg, Phys. Rev. B **21**, 15592 (1995).

[74] M. Büttiker, E. P. Harris, and R. Landauer, Phys. Rev. B **23**, 1268 (1983).

[75] H. Grabert, Phys. Rev. Lett. **61**, 1683 (1988).

[76] S. Linkwitz, H. Grabert, E. Turlot, D. Estève, and M. Devoret, Phys. Rev. A **45**, R3369 (1992).

[77] B. Ruggiero, C. Granata, V. G. Palmieri, A. Esposito, M. Russo, and P. Silvestrini, Phys. Rev. B **57**, 134 (1998).

[78] P. Silvestrini, S. Pagano, and R. Cristiano, Phys. Rev. Lett. **60**, 844 (1988).

[79] J. M. Kivioja, T. E. Nieminen, J. Claudon, O. Buisson, F. W. J. Hekking, and J. P. Pekola, Phys. Rev. Lett. **94**, 247002 (2005).

[80] E. Ben-Jacob, D. J. Bergman, B. J. Matkowsky, and Z. Schuss, Phys. Rev. A **26**, 2805 (1982).

[81] E. Ben-Jacob, D. J. Bergman, and Z. Schuss, Phys. Rev. B **25**, 519 (1982).

[82] S. R. Shenoy and G. S. Agarwal, Phys. Rev. Lett. **44**, 1524 (1980).

[83] N. Grønbech-Jensen, *et al.,* Phys. Rev. Lett. **93**, 107002 (2004).

[84] I. Sidiqqi, *et al.*, Phys. Rev. Lett. **94**, 027005 (2005).

[85] M. I. Dykman and M. A. Krivoglaz, Physica A **104**, 495 (1980).

[86] M. I. Dykman and M. A. Krivoglaz, Zh. Eksp. Teor. Fiz. **77**, 60 (1979) [Sov. Phys. JETP **50**, 30 (1979)].

[87] M. I. Dykman and M. A. Krivoglaz, Physica A **104**, 480 (1980).

[88] M. I. Dykman and V. N. Smelyanski, Phys. Rev. A **41**, 3090 (1990).

[89] N. Berglund, B. Gentz, *Noise-Induced Phenomena in Slow-Fast Dynamical Systems: A Sample-Paths Approach, Probability and its Applications* (Springer, Berlin, 2005).

[90] E. Neumann and A. Pikovsky, Eur. Phys. J. B **26**, 219 (2002).

[91] D. Stein, cond-mat/0411283 (2004).

[92] M. D. Fiske, Rev. Mod. Phys. **36**, 221 (1964).

[93] D. D. Coon and M. D. Fiske, Phys. Rev. **138**, A744 (1965).

[94] R. E. Eck, D. J. Scalapino, and B. N. Taylor, Phys. Rev. Lett. **13**, 15 (1964).

[95] I. O. Kulik, Zh. Eksp. Teor. Fiz. Pis'ma **2**, 134 (1965) [JETP Lett. **2**, 84 (1965)].

[96] A. Barone, G. Paterno, *Physics and Applications of the Josephson Effect* (Wiley, New York, 1982).

[97] P. Dubos, P. Charlat, Th. Crozes, P. Paniez, and B. Pannetier, J. Vac. Sci. Technol. **18**, 122 (2000).

[98] T. Kontos, *Cohérence et interférences quantiques dans des nanostructures supraconducteur / ferromagnétique*, PhD thesis, Orsay-Paris Sud, 2002.

[99] T. Kontos, *et al.*, Phys. Rev. Lett. **89**, 137007 (2002).

[100] D. B. Schwartz, B. Sen, C. N. Archie, and J. E. Lukens, Phys. Rev. Lett. **55**, 1547 (1985).

[101] I. Petković and M. Aprili, Phys. Rev. Lett., accepted for publication (2009); cond-mat/0812.2689 (2008).

[102] G. Ithier, *Manipulation, lecture et analyse de la décoherénce d'un bit quantique supraconducteur*, PhD thesis, CEA-Saclay (2005).

[103] I. Petković and M. Aprili, *in preparation.*